UNIVERSITY OF OKLAHOMA

GRADUATE COLLEGE

Disentangling the relative contribution of land-atmosphere coupling toward the evolution of extreme events

A DISSERTATION

SUBMITTED TO THE GRADUATE FACULTY

in partial fulfillment of the requirements for the

Degree of

DOCTOR OF PHILOSOPHY

By

Ryann Ashley Wakefield
Norman, Oklahoma
May 2021

Disentangling the relative contribution of land-atmosphere coupling toward the evolution of extreme events

A DISSERTATION APPROVED FOR THE
SCHOOL OF METEOROLOGY

BY THE COMMITTEE CONSISTING OF

Dr. Jeffrey B. Basara, Chair

Dr. Jason C. Furtado

Dr. Phillip B. Chilson

Dr. Xiangming Xiao

Dr. Eric D. Hunt

© Copyright by Ryann Ashley Wakefield May 2021
All Rights Reserved.

Acknowledgments

Buckle up... this one's long. It takes a village to raise a Dr. Wakefield.

Thank you to the NASA Future Investigators in NASA Earth Space Science and Technology (FINESST) Program (award no. 80NSSC19K1365) for supporting the completion of this degree, and my dream.

This work could not have been completed without the guidance of my advisor, Dr. Jeff Basara, who saw potential in me well before I saw any in myself. Thanks for helping me grow as a scientist and for always putting in the extra effort to provide opportunities for career development, and of course, laughs in the CHEWe office. You always lead by example, and with a positive attitude even when it doesn't seem like there's a lot to be positive about! I'm beyond grateful that you were willing to meet with an overly enthusiastic REU student in 2015, and from that, I've had the opportunity to work with you throughout my graduate career. I'm not sure I would have stuck with it if you hadn't shown me that I could, and should pursue the PhD. Somehow, you made me more confident and helped me to finally believe in myself. My committee members, Dr. Jason Furtado, Dr. Eric Hunt, Dr. Phil Chilson and Dr. Xiangming Xiao, have also made this process much kinder to me than expected, and I'm grateful that I left any meetings/defenses inspired rather than flustered. In particular, thanks to Dr. Jason Furtado for serving on my MS and PhD committees, teaching and inspiring me along the way, and always being supportive through publications and career advancement. I'll miss our hallway chats about the latest Dunkin seasonal flavor releases! Dr. Eric Hunt, you also provided exciting conversations about anything from irrigation to beer. You're a wonderful friend and mentor.

I've also been incredibly fortunate to have Dr. Dave Turner serve as a mentor during a majority of my PhD. Through internships, workshops and other collaborations you've brought me into, I've gained confidence in my role in the scientific community and discovered a career path that gives meaning to the scientific research I get to do. Our conversations always leave me inspired to think creatively about the science and with 1000 more ideas. I

look forward to at least going after at least 999 of those in the near future. This PhD also would not have been completed without the guidance and mentorship of Dr. Joe Santanello, who not only taught me SO MUCH about L-A coupling, but also provided career guidance, kindness and motivation/enthusiasm when PhD'ing in a pandemic became even more challenging. I'm so grateful for your willingness to help me become more involved with the LoCo community and for treating me like a colleague from the very start. I hope we can continue collaborating and talking L-A coupling (and about our dogs) for many years to come. I think there's something in those "hostile mixing diagrams." Finally, Dr. Patricia Lawston-Parker and Dr. Jinwoong Yoo made much of Chapter 5 possible by patiently answering all of my questions and helping me to debug NUWRF or LIS when I accidentally deleted a line, or by providing suggestions for how to improve my simulations.

Thank you to my coauthors, Noah Brauer, Dr. Marshall Shepherd and Roger Edwards. Noah, you made me excited to talk about tropical cyclones. Dr. Marshall Shepherd, your work on TCMI inspired much of this work, but what you may not know is that your 2009 paper about soil moisture and tornadoes in the southeast was what initiated my interest in land-atmosphere interactions. Having you as a coauthor has been humbling and a true honor. Roger, where to begin? Clayton, NM Dairy Queen? I'm so very grateful to have had your friendship and mentorship throughout my undergraduate and graduate education (and beyond).

To Jack Hales, thank you for being my first friend and mentor in the weather community and for all of the emails and phone calls to chat about weather and get me acquainted with this field. You helped me to find the opportunities that snowballed into a dream career. I cannot express to you enough how appreciative I am to have your friendship and support. And to Sarah, thank you for connecting me with both Jack and Roger, for your friendship, and for being willing to hang out with me whenever I'm in Phoenix! Your kindness is inspiring, and I'm so glad I met you.

My REU mentors, Dr. Esther Mullens, Dr. Derek Rosendahl, and Dr. Harold Brooks played a pivotal role in starting this science journey, helping me discover a love for research and making me believe that I might actually be able to apply to OU for graduate school.

I wouldn't be very intelligent if I didn't acknowledge the main reason I'm here, and that's my faith. There have been so many answered (and unanswered) prayers along the way that led me to my dream career.

I'm also forever indebted to my husband, Dalton, for his unwavering support and his pep talks during the thousands of times I told him I didn't think I could do this. He is my inspiration to always strive to be better, and really the one I've been trying to impress all this time. Thanks for letting me go back to school even though I'd already gone to school, then moving to Oklahoma so I could do more school! So, Dalton, if you are ever reading this long document of nerd things written by your nerdy wife, thank you and I love you.

Thank you to the CHEWe research group (current and alumni!) for lots of laughs and support along the way. Thank you to my friends in Done-damentals 2016, who helped me get through the challenging coursework in this program and for making it a little easier to do so. Even during the caffeine fueled sessions in the basement of the library, rewriting derivations until we wanted to (or actually did) cry. You made grad school a lot more fun than I ever expected. Elisa Murillo, from REU to grad school, you've been such a supportive friend, and I'm so grateful we met way back in 2015.

Finally, last but certainly not least, my parents. My weather nerd journey began with tornado nightmares, so I must thank my parents for their patience during all the times I woke up screaming "tornado" or got in trouble for screaming "tornado" in Mr. Davis's class, or screamed "tornado" while driving home from the lake. Thank you for helping me grow my interest in weather rather than trying to suppress it and for fighting to give me educational opportunities that let me stay engaged in school so that I could get here. Thank you for your love and support. Mom, you've been my biggest cheerleader in taking my

education as far as it can go, from having my teachers keep me busy with extra reading, to buying me cool science books, to letting me ramble (or cry) about all this PhD stuff. Dad, thank you for always letting me be excited about weather and for being excited yourself, for driving into a storm, in the Ozarks, with your daughter who knew nothing about meteorology, and for always believing I could do this.

Okay actually... one last thank you to my adorable doggoes, Baylee, Moo and Addie. Life would be pretty ”ruff” without all the cuddles from you.

Table of Contents

List of Tables

List of Figures

Abstract

The Great Plains region is characterized by highly variable and often extreme precipitation. Devastating multi-year droughts are common in the region, and can often be followed by years of above normal precipitation. Drought onset can be difficult to predict, especially in cases known as flash drought when both onset and intensification are rapid. These flash drought events can often lead into longer term drought such as was observed across much of the central United States during 2012.

On the other side of the precipitation distribution lies excessive rainfall, and the impacts of resulting flooding can be just as detrimental to agriculture and society in the region. While landlocked states in the Great Plains aren't typically associated with tropical cyclones, recent studies have begun to draw attention to the idea that these storms may reintensify over land in the presence of anomalously wet soils. This is colloquially known as the Brown Ocean Effect. It has been hypothesized that above normal precipitation during spring of 2015 provided sufficiently wet soils to aid in the reintensification of Tropical Storm Bill as it propagated inland over the Great Plains and Midwest.

Though the flash drought/drought of 2012 and Tropical Storm Bill during 2015 seem unrelated except for shared geography, both extremes may have been influenced by land-atmosphere feedbacks. It is well known that drought and heavy precipitation are often tied to larger scale atmospheric forcing, however, numerous studies have demonstrated that land-atmosphere feedbacks may also amplify extremes in the region. It remains a challenge to disentangle the influence of the land surface from that of the overall atmospheric pattern. However, the key to increased predictability for events such as flash drought may rely on answering the question "to what extent does the land surface really influence hydroclimate extremes?" This study presents new approaches to better estimate the relative contributions of land-atmosphere feedbacks toward precipitation extremes in the Great Plains, with a primary focus on the flash drought/drought of 2012 and the overland maintenance/reintensification of Tropical Storm Bill during 2015.

Chapter 1

Introduction

The United States National Academy of Sciences Decadal Survey (2017) established a list of key science and application questions to be addressed in the ensuing decade (Board et al. 2017). Among the most important science questions was how changes in the water cycle, including changes to evapotranspiration, could impact the *"frequency and magnitude of precipitation extremes such as droughts and floods" (science question H-1)*. In other words, what is the relative contribution of the terrestrial surface to the evolution of extreme precipitation events?

Straddling the 100th meridian, the Great Plains marks the transition zone from a more arid climate to the west and humid climate to the east (Seager et al. 2018). Like other transitional climates throughout the world, land-atmosphere (L-A) interactions are an important influence on the Great Plains hydroclimate (Koster et al. 2004; Guo et al. 2006; Koster et al. 2006; Basara and Christian 2018). Soil moisture gradients and associated differential diabatic heating can drive localized boundaries (Taylor et al. 2007; Frye and Mote 2010), and on the seasonal scale, persistent soil moisture anomalies can influence the quasi-persistent location of the dryline (Flanagan et al. 2017). Anomalous soil moisture can also reinforce seasonal extremes through soil moisture memory (Koster and Suarez 2001) and can influence changes in large scale dynamics (Namias 1988). Further, widespread anomalously dry soils may result in local L-A feedbacks that reinforce existing drought (Atlas et al. 1993; Hong and Kalnay 2000; Pal and Eltahir 2003; Dong et al. 2011; Su and Dickinson 2017) but they may also support drought propagation through suppression of precipitation downstream (Fernando et al. 2016; Koster et al. 2016; Su and Dickinson 2017). At the same time, land-atmosphere feedbacks are part of the much larger climate system, and as such, the relative contribution of such feedbacks to regional precipitation

extremes may be muted or amplified depending upon the large scale synoptic environment (Song et al. 2016; Welty and Zeng 2018).

Excessive precipitation impacts are similarly experienced within the Great Plains region. In some cases, this excess is welcome, as it may provide long awaited relief from multi-year drought (Wu and Dirmeyer 2020). Such drought-terminating precipitation events are often the result of atmospheric rivers, but they may also be attributed to rainfall from landfalling tropical cyclones. While tropical cyclones are not typically associated with the interior of the United States, recent studies have shown that L-A feedbacks can contribute to the overland maintenance and/or reintensification of landfalling tropical cyclones (Emanuel et al. 2008; Arndt et al. 2009; Evans et al. 2011; Monteverdi and Edwards 2010; Andersen et al. 2013; Andersen and Shepherd 2014). Tropical cyclone maintenance and/or reintensification (TCMI Andersen et al. 2013) is colloquially referred to as the Brown Ocean Effect as anomalously wet soils are thought to supply sufficient latent heat fluxes to the tropical cyclone to mimic latent heat fluxes over the ocean. While much of the existing research focuses on the contributions of latent heat fluxes in regions along the tropical cyclone's path, however studies of tropical cyclones over the ocean imply that latent heat fluxes along the storm's inflow may also play a vital role in its evolution (Fujiwara et al. 2017).

Thus, opposite extremes of the hydroclimate spectrum are likely influenced by L-A interactions. The impact of land-atmosphere feedbacks on local PBL development during extreme events such as drought as well as the influence of these feedbacks on propagation of such events remain key questions in the scientific community (Miralles et al. 2019). This challenge is the primary motivation behind the work of this dissertation. In other words, *how can the relative contributions of L-A interactions be distinguished from large scale atmospheric forcing during precipitation extremes in the Great Plains?*

Specifically the hypothesis of this dissertation is that L-A interactions exert influence locally, in the immediate vicinity of extreme events, but also non-locally, through

modification of upstream air masses. The contributions of these L-A interactions can be discerned from the background atmospheric state associated with excessive precipitation or extreme drought driven by L-A interactions.

The first step in testing this hypothesis consisted of preliminary work to identify how existing L-A coupling frameworks may be further leveraged to address the influence of both local and non-local L-A interactions. Additionally, the broader hypothesis motivating this study was further broken down into two event-specific hypotheses highlighted below with their respective studies. The L-A coupling framework analyses and the two event-specific analyses are summarized below:

- Chapters 2 and 3 used observational data to test, select, and modify/improve frameworks for quantifying L-A coupling that can best address local, versus non-local, versus large-scale influences during extreme events. The frameworks were modified to more closely approximate closure of boundary layer moisture and energy budgets and therefore, better quantified the relative contributions of each source and sink to these budgets.

- Chapter 4 was motivated by the first event specific hypothesis that **anomalously wet soils due to above normal antecedent precipitation during 2015 provided sufficient fluxes of moisture over land to support the inland maintenance and reintensification of Tropical Storm(TS) Bill (2015).** The novelty of this study was that it also introduced a method for considering non-local surface flux contributions to the storm's evolution through evaluating surface fluxes along inflow trajectories.

- Chapter 5 used coupled model simulations to test the sensitivity of PBL moisture and energy budgets during the 2012 flash drought to extreme wet and dry soil moisture states using the modified coupling metric method demonstrated in Chapter 3. The goal of this analysis was to specifically test the hypothesis that **L-A feedbacks amplified the background atmospheric state to support the 2012 flash drought and extended period of drought that followed.**

Together these studies provide a novel contribution to the science of L-A coupling by introducing new methods and associated insights that demonstrate how the relative contributions of L-A feedbacks can amplify the background atmospheric state to support wet and dry precipitation extremes.

Chapter 2

Evaluation of a land-atmosphere coupling metric computed from a ground-based infrared interferometer

2.1 Introduction

Land-atmosphere interactions play a critical role in both the atmospheric water and energy cycle. The sensitivity of the atmosphere to changes in land surface conditions is particularly pronounced in semi-arid regions throughout the world (Guo et al. 2006; Koster et al. 2006; Dirmeyer 2006). Changes in soil moisture and vegetation health alter the partitioning of surface water and energy fluxes, influencing diurnal evolution of the planetary boundary layer (PBL), and even subsequent cloud and precipitation development. Along the same lines, persistence in soil moisture states may drive longer term precipitation anomalies and geopotential height anomalies (Koster et al. 2016). As such, extreme events such as drought, heatwaves (Miralles et al. 2014; Schumacher et al. 2019), heavy rainfall (Wei et al. 2016; Song et al. 2016), or even the overland re-intensification of tropical cyclones (Emanuel et al. 2008; Arndt et al. 2009; Andersen et al. 2013; Andersen and Shepherd 2014) can be impacted by land-atmosphere feedbacks. Greater understanding of how the atmosphere and land surface covary, also referred to as land-atmosphere coupling (LA coupling), is essential to improving predictability of such extremes (Seneviratne et al. 2006; Koster et al. 2011; Dirmeyer and Halder 2016). Numerical modeling approaches to study LA coupling range in scale from single column models (Ek and Mahrt 1994; Ek and Holtslag 2004) to atmospheric general circulation models (Dirmeyer 2001; Koster et al. 2004; Guo et al. 2006; Koster et al. 2014) to conceptualize the link between surface and atmospheric processes across scales. Observation based studies (e.g., Basara and Crawford 2002; McPherson et al. 2004; Phillips and Klein 2014; Tang et al. 2018) supplement these

approaches by quantifying the true behavior of these processes in nature and can inform more realistic representation of coupling in models. Coupling metrics arose from the need to succinctly quantify land-atmosphere feedbacks in both modeling and observational studies (Santanello Jr et al. 2018). Numerous metrics have been developed by the LA coupling community and exist on a spectrum of complexity. Process level metrics describe multiple components of the local land-atmosphere coupling process chain (Santanello Jr et al. 2011; Santanello et al. 2011), to better capture the multiple steps through which the land surface influences the evolution of the PBL and free atmosphere.

One frequently used process-level coupling metric is the Convective Triggering Potential, Low-Level Humidity Index (CTP-HI_{low}) framework (Findell and Eltahir 2003a,b). This metric has been applied using its original formulation across multiple regions of the world (Jach et al. 2020). It has also been modified based on climatology of the metric over various regions (Ferguson and Wood 2011; Wakefield et al. 2019) or to create a new diagnostic for land-atmosphere coupling contributions to hydroclimate extremes such as drought (Roundy et al. 2013; Roundy and Santanello 2017). The CTP-HI framework uses early morning vertical profiles to diagnose whether the atmosphere is preconditioned toward clouds and/or convective precipitation triggered over wet or dry soils (Findell and Eltahir 2003a,b). The use of the early morning radiosonde profiles was intended to represent the lower troposphere before substantial mixing of the PBL occurs. In the contiguous United States (CONUS), 1200 UTC typically corresponds to a pre-convective boundary layer, between 0400 and 0800 local time (LT). However, in different regions of the world, neither of the synoptic radiosonde launches at 0000 UTC and 1200 UTC may coincide with the early morning PBL (i.e., perhaps they are in the middle of the night or they represent a well-mixed PBL in the day). One solution is to use vertical profiles corresponding to the same local time at every location. However, this approach is limited by the availability of vertical profiles during periods beyond the typical 1200 and 0000 UTC radiosonde observations.

To address this limitation, vertical profiles obtained from remote sensing platforms such as the Atmospheric Infrared Sounder (AIRS) on board NASA's Aqua satellite have been used to compute CTP and HI at the same local time (0130 LT) for locations around the world (Ferguson and Wood 2011; Roundy et al. 2013; Roundy and Santanello 2017). Because 0130 LT is consistent with a pre-convective boundary layer, it was suggested that little difference should exist between vertical profiles obtained at 0130 LT and those obtained at 1200 UTC (which corresponds to a local time of 0700 Central Daylight Time or CDT) across the CONUS. Indeed, there was good agreement between computations of CTP and HI obtained from AIRS when compared to reanalysis datasets. Even so, a lack of ground-based observations with sufficient temporal resolution made it difficult to directly observe whether temporal variability does truly exist in CTP and HI during the period between the AIRS overpass time and the radiosonde observation time. Furthermore, thermodynamic profiles retrieved from infrared sounders like AIRS have relatively little information content in the PBL, resulting in coarse (e.g., order 1 to 2 km) vertical resolution (Irion et al. 2018). As such, the temporal variability of CTP and HI will be explored further in this study.

The lack of such studies until now is primarily driven by a lack of atmospheric profile observations at higher spatial and/or temporal frequencies than those offered by the traditional twice daily radiosonde observations. Ground-based thermodynamic profilers, such as the Atmospheric Emitted Radiance Interferometer (AERI), provide an alternative method for obtaining vertical profiles of temperature and moisture at higher temporal frequencies and where radiosonde observations are absent. The AERI is a ground-based passive spectrometer which measures downwelling infrared radiation. Thermodynamic profiles are retrieved from the observed radiance data (method is described in Section 2.2), but the vertical resolution is lower than that of traditional radiosonde profiles. This decrease in vertical resolution introduces some uncertainty when using the AERI to compute convective indices, though these uncertainties are generally greatest for integrated indices

such as convective available potential energy (CAPE) (Blumberg et al. 2017). Despite this limitation, the temporal resolution of the AERI makes it a useful tool for monitoring destabilization trends within the PBL (Feltz et al. 2003; Wagner et al. 2008; Blumberg et al. 2015, 2017) at temporal resolutions unmatched by radiosonde observations.

The temporal resolution of the AERI provides a unique opportunity to evaluate land-atmosphere coupling, in particular, and allows us to address several questions left unanswered by previous studies. The main questions addressed in this study are:

1. What are the uncertainties associated with computing CTP and HI from AERI profiles relative to collocated radiosonde profiles?

2. Do CTP and HI exhibit substantial temporal variability overnight, or are these values consistent as long as they are obtained for a pre-convective PBL?

Analyses are focused at the Atmospheric Radiation Measurement (ARM) program's Southern Great Plains (SGP) site (Sisterson et al. 2016) in Lamont, Oklahoma during the summers (June, July, August) of 2017 and 2019.

2.2 Data

2.2.1 Atmospheric Emitted Radiance Interferometer (AERI)

The AERI measures downwelling radiance emitted from the atmosphere at wavelengths between 3.3 and 19.2 μm approximately twice per minute at 1 cm-1 spectral resolution (Knuteson et al. 2004a). The instrument maintains calibration by regularly observing two blackbodies, one at 60°C and one at ambient temperature, which results in the AERI maintaining its radiometric accuracy to better than 1% of the ambient radiance in both clear and cloudy conditions (Knuteson et al. 2004b). In the presence of precipitation, an automated hatch is closed to protect the foreoptics of the instrument.

2.2.2 AERIoe algorithm for thermodynamic profile retrieval

Retrieval algorithms are necessary to obtain thermodynamic profiles from the observed infrared radiance spectra. These algorithms make use of CO2 and H2O absorption bands that lie within the spectral range of the AERI to obtain temperature and water vapor profiles respectively. The original retrieval algorithm AERIprof (Feltz et al. 1998; Smith et al. 1999) had several limitations including the inability to retrieve thermodynamic profiles under low and midlevel clouds, which motivated the development of the AERIoe algorithm to addresses these shortcomings (Turner and Löhnert 2014; Turner and Blumberg 2018). The AERIoe algorithm retrieves thermodynamic profiles and cloud properties (e.g., liquid water path) from the AERI radiance observations using an optimal estimation (OE) framework (Rodgers 2000). This framework allows for the uncertainties associated with each retrieved variable to be quantified, and these uncertainties can be propagated to provide uncertainties in the derived coupling metrics.

2.2.3 Site Selection

While multiple AERI instruments are located in the ARM SGP domain, only the central facility (denoted sgpC1) AERI was used for this particular study as radiosondes are launched within 150 m of this AERI. This allows for coupling metrics to be derived from both AERI and radiosonde profiles and for the relative accuracy in the AERI derived metrics to be quantified. This study used sgpC1 and 1200 UTC radiosonde data from three periods: 16 May to 12 June 2017, 1 to 31 August 2017, and 17 April to 31 August 2019. These three periods coincide with three different field campaigns at the ARM SGP site. The 16 May to 12 June 2017 period was in support of the Vaisala DIAL IOP (Newsom et al. 2020), the August 2017 period was in support of the Land-Atmosphere Feedback Experiment (LAFE; Wulfmeyer et al. 2018), and the 2019 period was in support of the Micropulse DIAL IOP.

2.3 CTP-HI Analysis

2.3.1 Framework Description

The Convective Triggering Potential Low-Level Humidity Index (CTP- HI_{low}, hereafter CTP-HI) was developed by Findell and Eltahir (2003a,b) to diagnose the preconditioning of the atmosphere toward locally triggered convection based upon whether soils are wet or dry. It was developed from the output of a one-dimensional model over Illinois and further tested using observational data from upper air stations across the United States. The framework uses the 1200 UTC sounding data, which is within a few hours of sunrise in most locations within the continental U.S., in order to determine the moisture content and instability within the portion of the atmosphere most likely to be incorporated into the growing mixed layer.

HI is computed from the sum of the dewpoint depressions at 50 mb and 150 mb above ground level (AGL) to provide an estimate of the pre-existing moisture in the atmosphere (2.1) and its units are in degrees Celsius.

$$HI = (T - T_d)_{150\,mb\,AGL} + (T - T_d)_{50\,mb\,AGL} \tag{2.1}$$

CTP is computed by locating the moist adiabat which intersects the temperature profile at 100 mb above ground level, and integrating the area between this moist adiabat and the temperature profile, upwards within a 200 mb layer from 100 mb above ground level to 300 mb above ground level. Units of CTP are J kg^{-1}. This process assumes a saturated parcel at 100 mb AGL. Pseudoadiabats (moist adiabats) were computed using the MetPy (May et al. 2020) software package which integrates the equation for moist adiabatic lapse rate obtained from equation 5 in Bakhshaii and Stull (01 Jan. 2013). The computation of CTP is similar to that of Convective Available Potential Energy (CAPE). CTP estimates the instability within the layer of the atmosphere between 100 and 300 mb AGL (approximately 1 to 3 km AGL). The combined CTP and HI pair can be used to

diagnose whether convection is favored over wet or dry soils based upon thresholds set forth in Findell and Eltahir (2003a,b).

Based on this information, the atmosphere is classified into several different categories:

1. Atmospherically controlled: This can either mean that if convection occurs, it is not locally triggered, or it can mean that the atmosphere is too stable or too dry for convective triggering. Therefore, this category has been divided into 3 subcategories based on Findell and Eltahir (2003a,b).

   (a) Atmospherically Controlled Stable (ACst), where the atmosphere is too stable for precipitation (When CTP $<$0 J/kg)

   (b) Atmospherically Controlled Wet (ACw), where the atmosphere is already moist such that rainfall or shallow clouds can occur over any soil condition depending on CTP value (HI $<$5°C)

   (c) Atmospherically Controlled Dry (ACd), where the atmosphere is too arid for convective precipitation to occur (HI $>$15 °C)

2. Wet Advantage (WA): Locally triggered convection most likely over wet soils

3. Dry Advantage (DA): Locally triggered convection most likely over dry soils.

4. Transition (T): Convection may occur over any soil type, but no convection is the most likely outcome. If convection is triggered, it is most likely over dry soils.

The numerical thresholds for each category are depicted in Figure 15 of Findell and Eltahir (2003a) and is reproduced here in Figure 2.1.

2.3.2 Uncertainties associated with AERI derived CTP and HI

The framework uses morning vertical profiles from radiosondes, and in the western hemisphere, this corresponds to the 1200 UTC observation. While these are considered 1200

UTC observations, they are typically recorded in the hour between 1100 and 1200 UTC. Thus, the typical 1200 UTC radiosonde observation is often still within the boundary layer during the 1100 to 1200 UTC time window. As such, AERI retrievals were chosen with the requirements that they occurred within the 1100-1200 UTC window that had both (a) small root mean square (RMS) error (i.e., the retrieved thermodynamic profile agrees well, in a radiance sense, with the radiance observations) and (b) the retrieved liquid water path (LWP) was less than 6 g m^{-2} to ensure little to no overhead clouds. Of the retrievals that met the aforementioned criteria, the retrieval closest in time to radiosonde launch time was selected for comparison.

CTP and HI were computed from the selected AERI profile. Each AERI-retrieved profile has its associated uncertainties that can be used to approximate uncertainties in the CTP and HI values obtained from the profile. Using the posterior error covariance matrix produced by the AERIoe retrieval algorithm, uncertainties in the profile were then estimated by using Monte Carlo resampling of the posterior error covariance matrix 500 times (similar to the approach used in Blumberg et al 2017). This produced a distribution of 500 possible water vapor and temperature profiles. CTP and HI were then computed from each profile to obtain a distribution of possible CTP and HI observations at a given time. First, CTP and HI observations obtained from the full vertical resolution of the radiosonde profiles were compared to those obtained from the AERI thermodynamic profiles. Figures 2.2a and 2.3a show that AERI derived CTP and HI agreed well with HI and CTP values obtained from the radiosonde observations, respectively. R^2 values computed using the Pearson correlation coefficient indicate that HI displayed slightly better agreement between the two platforms with a slightly greater R^2 value than that of CTP 2.1. When broken down by year, both years performed similarly.

One primary source of error in the AERI-retrieved versus radiosonde profiles arises due to differences in vertical resolution. Given the reduced vertical resolution in the AERI (see Figure 7 in Turner and Löhnert 2014) as compared to radiosonde profiles, differences

Table 2.1: R^2 values computed from Pearson Correlation for AERI versus Radiosonde CTP and HI observations, bias and standard deviation of the difference between AERI and radiosonde observations.

	R^2 2017 (N=43)	R^2 2019 (N=95)	R^2 Both (N=138)	Bias (Both)	Standard Deviation (Both)
AERI vs. Radiosonde HI	0.64	0.66	0.65	-0.45°C	4.32°C
AERI vs. Smoothed Radiosonde HI	0.75	0.86	0.83	-0.29°C	3.66°C
AERI vs. Radiosonde CTP	0.65	0.63	0.62	18.1 Jkg^{-1}	98.7 Jkg^{-1}
AERI vs. Smoothed Radiosonde CTP	0.70	0.76	0.72	6.7 Jkg^{-1}	71.7 Jkg^{-1}

in CTP and HI observed from each platform may be attributed to differences in vertical resolution. To test this theory, radiosonde profiles were smoothed to the same vertical resolution as the corresponding AERI profiles for the given time. This was completed using the averaging kernel produced by the AERIoe retrieval algorithm (Turner and Löhnert 2014). Reducing the vertical resolution of the radiosonde profiles produced CTP and HI values that were more similar to those obtained from the AERI (Fig. 2.2c, Fig. 2.3c). The improved agreement suggests that the unsmoothed radiosonde profiles and AERI profiles differ, in part, due to differences in vertical resolution. Overall, CTP showed a lower degree of covariability than HI in datasets for both years and for the smoothed and unsmoothed comparison.

2.3.3 Accuracy of Pre-Conditioning Classifications

A primary objective of this study is to determine whether the AERI can serve as a useful tool for implementing the CTP-HI framework to diagnose atmospheric preconditioning accurately. Therefore additional comparisons to values obtained from the unsmoothed radiosonde profiles were performed. This enabled evaluation of whether the AERI can provide the same diagnosis of atmospheric preconditioning via the CTP-HI framework as the radiosonde despite its lower vertical resolution. Hereafter any reference to radiosonde profiles is referring to the unsmoothed radiosonde profiles.

The combination of CTP and HI observations for a given time were used to diagnose atmospheric preconditioning based upon discrete thresholds for each preconditioning category. Because of the discrete thresholds used in this coupling framework, small differences in CTP and HI between the AERI and radiosonde could result in a different classification of the atmospheric preconditioning. These potential differences in classificaiton prompted additional comparison of the atmospheric preconditioning diagnosed by each instrument using the CTP-HI framework following the thresholds set forth in Findell and Eltahir (2003a,b). A 6x6 verification contingency table was created using the classification categories listed above, with Atmospherically Controlled (AC) conditions further separated into stable (ACst), wet (ACw), and dry (ACd) categories within the table (Fig. 4). AERI and radiosonde observations that produced the same classification reside along the diagonal, while off-diagonal elements represent differences in classification. The Heidke Skill Score (HSS; Equation 2.2) was computed to diagnose the AERI's skill using the approach in Wilks (2011),

$$HSS = \frac{\sum_{i=1}^{I} p(y_i, o_i) - \sum_{i=1}^{I} p(y_i)p(o_i)}{1 - \sum_{i=1}^{I} p(y_i)p(o_i)} \tag{2.2}$$

where I represents the number of elements in the row or column, i is the i-th element, $p(y_i, o_i)$ represents the joint distribution of AERI and radiosonde classifications, or diagonal elements of the table, while the individual AERI $p(y_i)$ and radiosonde $p(o_i)$

marginal distributions of observations represent the off-diagonal elements. In terms of forecast verification, a HSS of 1 represents a perfect forecast; i.e., that the AERI classifications perfectly matched the radiosonde classifications, while a score of 0 indicates that the same agreement between radiosonde and AERI classifications could be achieved by chance.

In addition, all possible classifications were considered within the retrieval's window of uncertainty. The window of uncertainty was defined as greater than or less than one-half standard deviation of the observed value based upon the distribution of potential profiles. CTP and HI were computed from each of the profiles within this window of uncertainty to diagnose atmospheric preconditioning. When the range of uncertainties of CTP and HI values produced only 2 possible classifications, these classifications were still considered. This captured those cases when CTP and HI observations between the two platforms may have been nearly identical, but on opposite sides of a classification threshold. For example, if CTP observed by both platforms lied between 150 and 200 J/kg, but the observed HI for one platform was 9.5 degrees Celsius while the other was 10.2 degrees Celsius, then the former would be considered "wet advantage" while the latter would be considered "transition." Thus, for the uncertainty analysis, if the AERI classification differed from that of the radiosonde initially, but the "correct" (radiosonde) classification was within the AERI's window of uncertainty, and that window of uncertainty only included two possible classifications, then that day would be counted as a "hit." A summary of these methods can be found in Figure 2.5.

AERI and radiosonde observations produced the same classification of atmospheric preconditioning approximately 71% of the time with a HSS of 0.62 (Fig. 2.4a). The majority of days were atmospherically controlled. For wet advantage and dry advantage days, the two platforms agreed just over half of the time, while transition days displayed more off-diagonal counts than counts along the diagonal. When a limited range of uncertainty (Fig. 2.4b), was introduced, this resulted in agreement on 81% of days, while agreement on

both wet and dry advantage days improved from just over half of days to over 75% of days. Transition days also displayed a tremendous improvement in agreement when considering uncertainty, increasing from 29% to 57% of days, and the HSS improved from 0.62 to 0.75. The movement of off-diagonal elements to the diagonal suggests that the reason for differences in the initial classification are likely driven by borderline CTP and HI values that were near the thresholds for a given pair of categories.

2.3.4 Temporal Variability of CTP and HI

A second analysis examined the temporal variability in CTP and HI using only AERI observations. The motivation behind inspecting the temporal variability in these two quantities is driven by the potential differences across time zones in accumulated net radiation at upper air stations during the morning upper air observation. For example, during the summer, an upper air station on the east coast of the United States will have had two additional hours of downwelling shortwave radiation at 1200 UTC than an upper air station at the same latitude within the mountain time zone. Therefore, it is important to ensure that the 1200 UTC radiosonde observation can still be employed in the computation of this coupling metric across time zones.

The high temporal resolution of the AERI enables this type of analysis. While the AERI is at a fixed location, evaluating CTP and HI computed during time windows preceding and following the 1200 UTC radiosonde observation can be used to represent the accumulated net radiation in other time zones. The 1100 to 1200 UTC time window was used as "truth" as it corresponds to the 1200 UTC radiosonde observations. Hereafter, this period is denoted as **T12**. Because the ARM central facility is located within the central time zone, accumulated net radiation in the mountain time zone at 1200 UTC would be one hour behind the central time zone, or more similar to what is observed in the central time zone during the 1000-1100 UTC time window (hereafter **T11**). Similarly, the eastern time

zone would be an hour ahead, or more similar to the accumulated net radiation at the central facility during the 1200-1300 UTC time window (**T13**).

Past applications of the framework (Ferguson and Wood 2011; Roundy et al. 2013; Roundy et al. 2017) have used vertical profiles obtained at times other than 1200 UTC such as those obtained from the Atmospheric Infrared Sounder (AIRS) which are acquired at approximately 0130 Local Time for a given location. As such, CTP and HI were also computed for the time window from 0700 UTC to 0800 UTC (**T08**), which corresponds to the AIRS overpass time at 0130 CST (local time).

It is hypothesized that, in the absence of significant advective processes or the passage of synoptic scale features, that these two quantities should remain relatively constant in time. Further, even in those locations where the sun rises earlier, the PBL should not be fully developed to the levels where CTP and HI are measured. The difference between CTP and HI at T12 (time window considered as truth) and the three other intervals were computed by subtracting the values at other times from the CTP and HI values at T12. All differences were statistically significant at $p<0.05$ except for the CTP differences for T11-T12 and T11-T10. The difference distributions (Fig.2.6) provide several key results:

1. HI at T11 and T13 displayed similar agreement with T12, while the HI values at T08 exhibited a much greater range of differences with T12 (Fig. 2.6a,c).

2. HI at T12 was slightly less than at T11 and slightly greater than at T13, and as such, the atmosphere slightly moistened over time (Fig. 2.6a,c). (Recall that higher values of HI correspond to greater dewpoint depressions.)

3. Similarly, T08 displayed the greatest differences from T12 and a negative median difference indicates that HI at T08 was greater than at T12 (Fig. 2.6c). This remains consistent with T11 and T13 results which indicate the atmosphere moistens with time.

4. HI at T11 and T13 had the lowest interquartile range (IQR) (Fig. 2.6c) with a majority of observations falling within 2 degrees Celsius of HI at T12, while the IQR for T08 was greater and a majority of T08 HI observations were within 6 degrees Celsius of those at T12.

5. CTP observations were relatively consistent for all three periods, and displayed the same sign as biases to those observed in HI, with CTP observations at T13 being less than those at T12, while CTP observations at T11 and T08 were greater than those at T12 (Fig. 2.6b,d).

6. The greatest differences in CTP were observed between T08 and T12 (Fig. 6d).

7. Most CTP observations at T08, T11 and T13 were within 100 J/kg of T12, with differences in T08 versus T12 having a greater IQR, or greater variability (Fig. 2.6d).

2.3.5 Composite Vertical Profiles

Composite mean profiles were computed to better understand where differences in CTP and HI were arising; CTP at each time period of interest was subtracted from CTP at T12. From this difference distribution, composite mean temperature profiles on the three days with the greatest differences in CTP above the 95^{th} percentile (Fig. 2.7a-c) and below the 5^{th} percentile (Fig. 2.7d-f) were computed. Evaluating both tails of the distribution allowed us to evaluate whether there were truly large differences between conditions in which T12 was over or underestimated, or whether the differences were related to small changes in the vertical profile at certain levels, such as the height of an inversion rising or falling. When CTP at T12 is greater than CTP at other times, these differences are primarily associated with differences in lapse rates within the layer. Temperature profiles displayed similar temperatures at 100 mb AGL, resulting in CTP parcel profiles being obtained for approximately the same moist adiabat. The profiles diverged above this level with steeper lapse rates observed for T12 contributing to more positive CTP than the comparison times.

Conversely, when CTP at T12 was less than CTP at other times, steeper lapse rates were often observed for the comparison times.

Composite mean profiles were also computed for HI difference distributions (Fig. 2.8). The greatest differences in HI were primarily driven by differences between dewpoint profiles while temperature profiles were markedly similar in time. An exception is those cases when HI at T12 was less than HI at T08 (Fig. 2.8d) where both temperature and dewpoint profiles differed among the two times. This confirms our hypothesis that the greater length of time between observations at T08 and T12 would allow for greater changes in temperature and moisture within the lower portions of the atmosphere. Even within the tails of the difference distributions, the differences in thermodynamic profiles are most pronounced at both levels in which HI is measured for T12-T08. The greatest contribution to differences in HI can be further narrowed down to differences in the dewpoint depression observations at 150 mb AGL. Most profiles show relatively better agreement in dewpoint depression observations at 50 mb AGL. The reasons for this are two-fold. First, given the AERI's ability to represent CTP and HI well, it is likely that temperature and moisture profiles changed between the two times being compared. Second, while the AERI provides a good representation of reality, all observations include some degree of uncertainty. In this case, vertical resolution decreases with height, and it is likely that coarser vertical resolution is playing a role in the greater differences in dewpoint depression observed at 150 mb AGL.

2.3.6 Temporal Variability in Pre-Conditioning Classifications

Even if median temporal differences in HI are close to 2 degrees Celsius and CTP median differences are approximately 100 Jkg^{-1}, they still may lead to the same category for classification of preconditioning based on the CTP-HI framework as long as these differences do not straddle categorical thresholds. Figure 9 shows contingency matrices of preconditioning classification categories at T12 versus T08 (Fig. 2.9a), T11 (Fig. 2.9b) and T13

(Fig. 2.9c) respectively, along with HSS. As in Figure 2.4, the categories shown are a slight extension of the original framework as the atmospherically controlled category was broken into sub-categories to discern whether atmospherically controlled scenarios were a result of enhanced stability (ACst), lack of moisture (ACd), or excess of moisture (ACw). Atmospherically controlled was the most common classification for all times, with the ACd sub-category occurring most frequently.

The greatest concentration of frequencies on the diagonal of each confusion matrix was most desirable (Fig 2.9), as that suggests both times agree on classification even when exact values of CTP and HI differ. Because T11 and T13 CTP and HI differed the least from T12, it is not surprising that these two times also displayed the greatest agreement in classifications with little difference in HSS and both agreeing with T12 during approximately 78% of days. Where CTP and HI differed most for the T08 case, the greatest frequency of off diagonal observations also occurred in the classification matrix (Fig. 2.9a). When T12 was classified as WA, T08 could be classified as any of the three non-atmospherically controlled classifications, though WA was still the most frequent classification. Overall, the same classification as T12 was produced by T08, T11 and T13 for 64, 78 and 79 percent of cases respectively.

When classification differences occurred, these were often for adjacent categories with a clustering of off diagonal counts immediately adjacent to those along the diagonal. To further explore this, the same uncertainty analysis that was used to compare the radiosonde and AERI observations was performed again, except that T12 (AERI) observations were considered "absolute truth" for this uncertainty analysis. Uncertainties were then computed at T08, T11, and T13 individually using each time's distribution of potential profiles and applying the same uncertainty thresholds used in the radiosonde versus AERI analysis. Addition of uncertainty improved the percentage of days with agreement in time for all three times considered, and also improved HSS for all three times (Fig. 2.10). The decrease in number of off-diagonal elements is especially apparent for T13 versus T12

(Fig. 2.10c). When the frequency of each category by time was examined instead, during the 2017 to 2019 period (Fig. 2.9d), and not at whether these were occurring on the same day, each time displayed similar frequencies per classification. ACd was observed less frequently at T13 than during the other periods, while ACw was observed most frequently for T13, further supporting the idea of atmospheric moistening with time. WA was the most common categorization for the non-atmospherically controlled days for all periods, while T and DA were similar in frequency for all time periods.

2.4 Discussion

This study demonstrated the utility of the AERI for observation-based land-atmosphere coupling analysis using the CTP-HI framework (Findell and Eltahir 2003a,b).

This study was motivated by two primary questions:

1. What are the uncertainties associated with computing CTP and HI from radiosonde profiles versus from ground-based AERI-retrieved profiles?

2. Do CTP and HI exhibit substantial temporal variability overnight, or are these values consistent as long as they are obtained for a pre-convective PBL?

It was demonstrated that the AERI provides a realistic representation of CTP and HI and agreed well with radiosonde observations of the same metrics, even though small uncertainties were still present. These uncertainties were most apparent for the comparison of CTP values computed from radiosonde versus AERI thermodynamic profiles. These uncertainties are not surprising given CTP is a vertically integrated metric and it incorporates observations from higher levels in the atmosphere. Integrated metrics such as CTP, or in the case of Blumberg et al. (2017), CAPE, have greater uncertainties than simpler metrics like HI. CTP measurements are also obtained at greater heights in the atmosphere (i.e. approximately 1 to 3 km) where vertical resolution of the AERI is reduced in comparison to

HI measurements which are made lower in the atmosphere (i.e. approximately 0.5 km and 1.5 km) where vertical resolution is greater.

The impact of vertical resolution on these uncertainties was further realized when radiosonde profiles were smoothed to the same resolution as AERI profiles. Comparison of profiles with the same vertical resolution produced greater agreement in observations of CTP and HI between the two observational platforms. This further suggests that vertical resolution is a significant driver of the difference between radiosonde and AERI derived CTP and HI. While uncertainties exist, they not hinder the AERI's ability to provide a realistic estimation of CTP and HI.

AERI and unsmoothed radiosonde diagnoses of atmospheric preconditioning based on the CTP-HI framework were identical for a majority of days, even if exact values of CTP and HI did not match. Incorporating uncertainty estimates further demonstrated the AERI's utility in applying the CTP and HI framework, producing a greater number of days in which both AERI and radiosonde profiles diagnosed the same atmospheric preconditioning. Such analyses further confirm the hypothesis that a majority of the initial differences in preconditioning classification were driven by instances when radiosonde CTP and HI values were at the boundaries of a given category's threshold. This was made apparent by the increase in along diagonal elements within the uncertainty contingency matrix (Fig. 2.5), and a corresponding decrease in off-diagonal elements, especially within adjacent categories.

The agreement between AERI and radiosonde observations of CTP and HI demonstrated that the AERI can be useful for obtaining vertical profiles in time and space where radiosonde observations are lacking. The temporal frequency of AERI observations also provides a unique opportunity to explore the variability of this metric in time. Accumulated net radiation varies in space such that soundings released at the same UTC time do not coincide with the exact same PBL conditions around the world. Variability surrounding the 1200 UTC observation was also assessed as this corresponds to the morning observation in much of the western hemisphere. It is important to note that the implications of

these results may be interpreted for locations in a different hemisphere, where the morning sounding may coincide with 0000 UTC. The primary concern is with variability in CTP and HI in the hours immediately preceding and following the hour of the morning sounding but an additional time period (0700-0800 UTC) was included in the analysis for comparison to past studies using the CTP-HI framework.

The results of this study suggest that variability in CTP and HI in the hours immediately surrounding the morning sounding is minimal. Composite mean profiles for the cases with the greatest temporal difference in CTP or HI indicate a greater variation in moisture profiles than temperature profiles with time at the levels in which CTP and HI are measured. This is important because it suggests that while CTP and HI are measured in portions of the atmosphere decoupled from the surface, the atmosphere continues to evolve. However, it is important to recognize that the variation in moisture may also be unique to the Southern Great Plains location and future work could address this by performing similar studies using AERI observations outside of this region.

In general, as the difference in time from T12 increases, so do the differences in CTP and HI, and this is particularly true for T08 versus T12 observations. Even the most extreme differences, in the tails of the difference distributions, were more pronounced for T08. The composite profiles were obtained for extreme values in the difference distributions and these extreme cases were often associated with frontal passages, low-level jets, and other large-scale phenomena (not shown). The large differences that arose over time as a result of these meteorological influences suggest that computations of CTP and HI obtained from satellite remote sensing platforms near T08 may not always be a good approximation for atmospheric preconditioning. While median temporal differences in CTP and HI were often small, even small differences in values can produce different classifications based on the original framework. Where T08 may diagnose the atmospheric preconditioning to be most favorable for convection over dry soils, T12 on the same day might diagnose the atmosphere as more favorable for convection over wet soils. Therefore, on a

specific day, greater uncertainty in the diagnosis of atmospheric preconditioning may exist with vertical profiles obtained further in time from the 1200 UTC observation window. T11 and T13 showed greater skill at producing the same preconditioning classification as T12, while T08 performed noticeably worse. Uncertainty estimates enhanced skill for all 3 times considered, suggesting that a reasonable estimate of atmospheric preconditioning can be obtained at times other than T12. Even so, when considering the categories that correspond to non-atmospherically controlled days, T08 displayed more off-diagonal elements for WA and T days despite incorporating a window of uncertainty. This likely reflects an actual difference in the atmospheric preconditioning between the two times, especially when T11 and T13 correctly identified such days at least half of the time when uncertainty windows were considered.

Even if CTP and HI observations at T08, T11, T12 and T13 were consistent with one another, synoptic scale processes could alter the environment at any time between the morning sounding and afternoon period for which the CTP-HI framework diagnoses convective pre-conditioning. For example, if wet soils were observed and application of the framework diagnosed the morning atmosphere as being pre-conditioned for convection over wet soils on a day with an afternoon frontal passage, it would be difficult to forecast the relative contribution of the land surface from the contribution of large-scale drivers toward triggering convective precipitation using this metric alone. Thus, a primary limitation of our analysis is that data were not filtered for synoptically quiescent days only as this would have adversely impacted sample size, but it is expected that doing so would result in even greater temporal agreement in CTP and HI values and greater predictive utility from those values. Finally, the thresholds provided by Findell and Eltahir (2003a,b) are meant to serve as guidelines and may be flexible based upon regional climatology (Wakefield et al. 2019).

2.5 Conclusions

The implications of this CTP-HI analysis are two-fold. First, by showing good agreement between radiosonde and AERI observations of CTP and HI, it was possible to evaluate the temporal variability in this coupling metric with confidence that the AERI retrievals are representative of reality. Second, some temporal variability was demonstrated in this metric within a given day, and applications of the framework are best suited to locations where the morning sounding corresponds to a local time within 1-2 hours of the morning sounding time in the central time zone.

Days in which HI and CTP differed greatly are not likely to be the most favorable days for L-A interactions studies as large-scale meteorological influences contributed to substantial temporal evolution in temperature and moisture profiles. As such, synoptic influences on moisture and temperature would likely overpower the influence of the land surface. However, it is possible that looking at the temporal evolution of CTP and HI over a location could provide a means of identifying days which are favorable for L-A coupling and those which are not. Days in which CTP and HI exceed a certain difference threshold over time would be considered unfavorable for L-A interaction studies. This could be automated for identification of such days within a large dataset. Such an approach is beyond the scope of the current study, but future work could evaluate whether there is a variability threshold for days which are considered optimal for land-atmosphere coupling study versus days which are not.

Vertical profiles of temperature and moisture are often incorporated into land-atmosphere coupling metrics which can limit their applicability from an observational perspective as the temporal and spatial coverage of atmospheric profiles is sparse. The AERI can be used in such locations to better observe land-atmosphere coupling, and these observations may also be used to verify model representation of land-atmosphere coupling in locations where such comparisons were not previously possible.

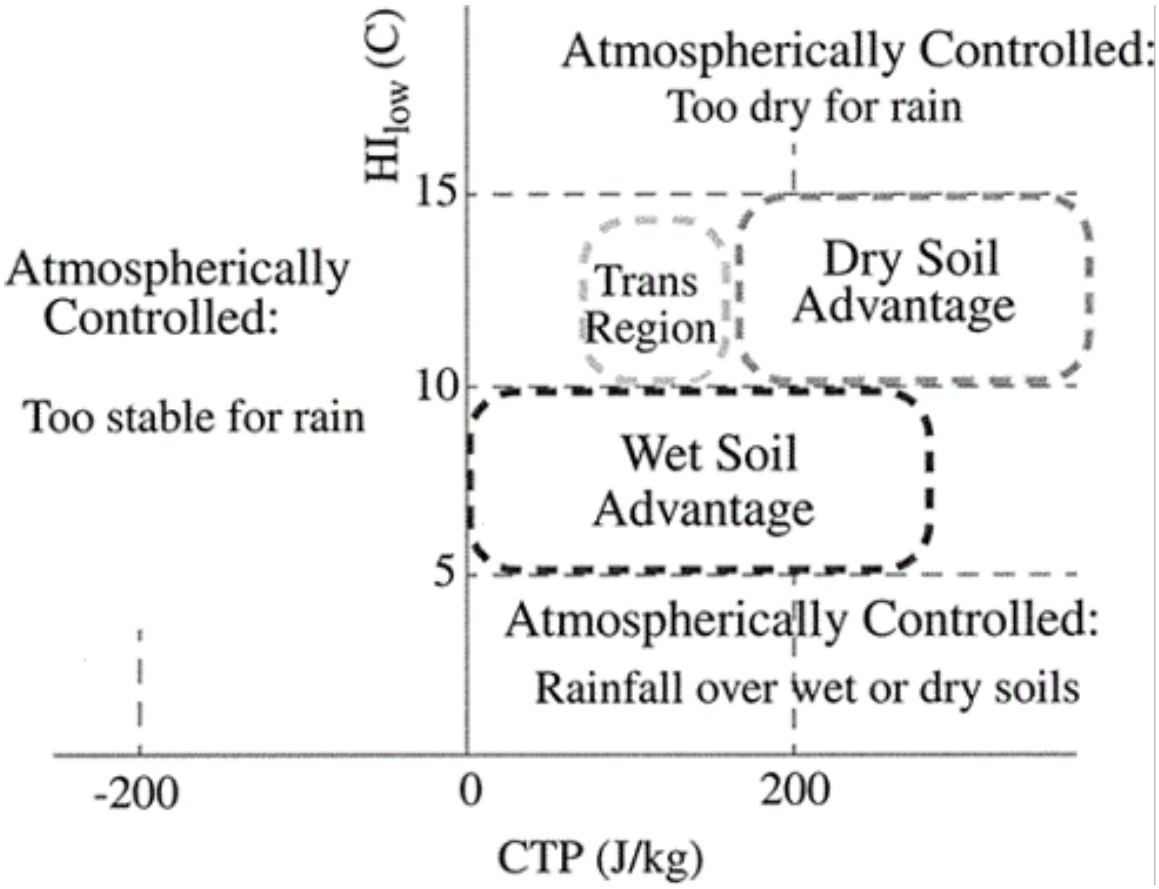

Figure 2.1: Figure 15 from Findell and Eltahir (2003a) showing CTP-HI combinations for each category of atmospheric preconditioning.

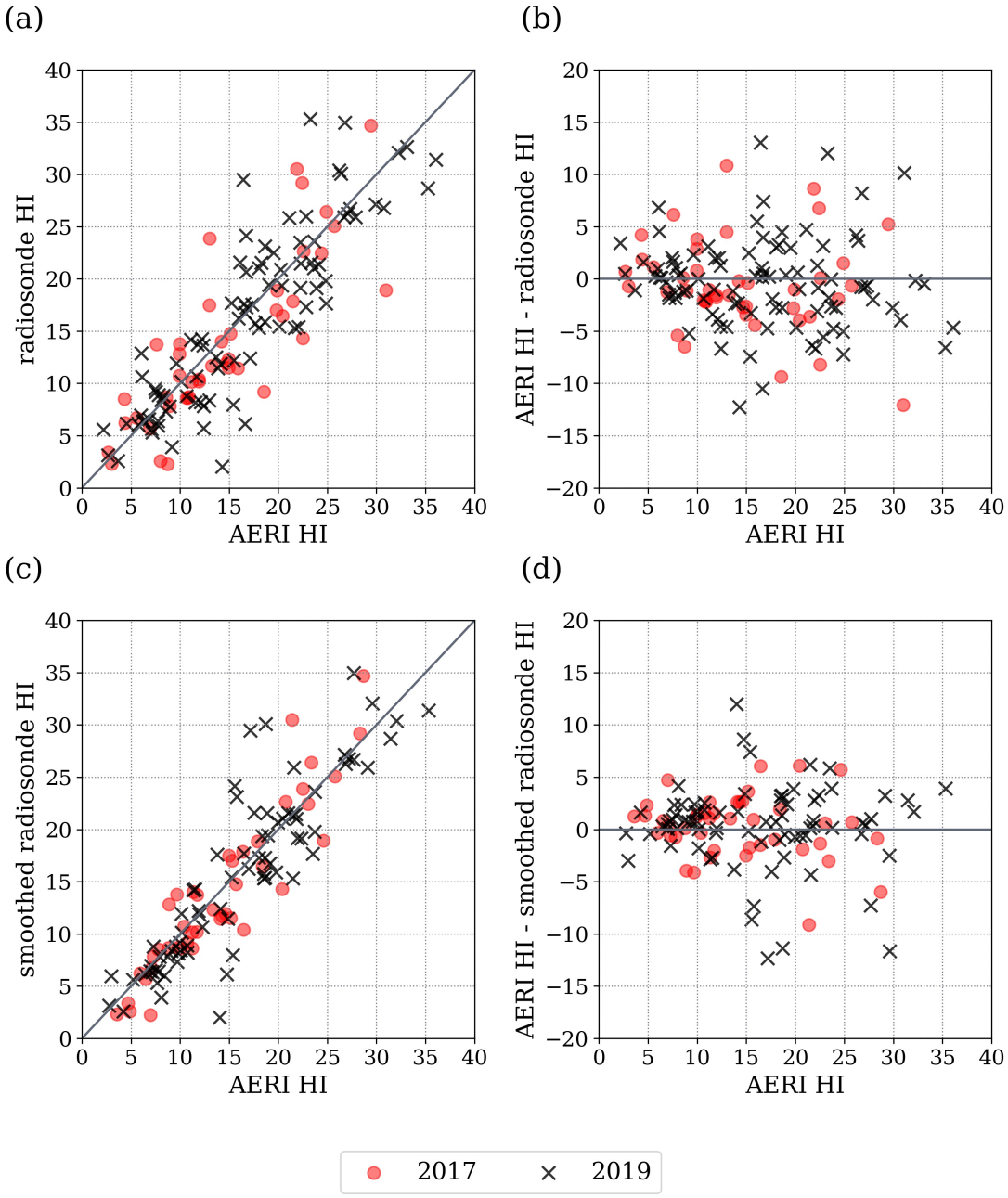

Figure 2.2: (a) AERI HI versus radiosonde HI (b) AERI HI versus AERI-radiosonde HI difference (c) AERI HI versus smoothed radiosonde HI and (d) AERI HI versus AERI-smoothed radiosonde HI difference. Black points represent 2017 data and red points represent 2019.

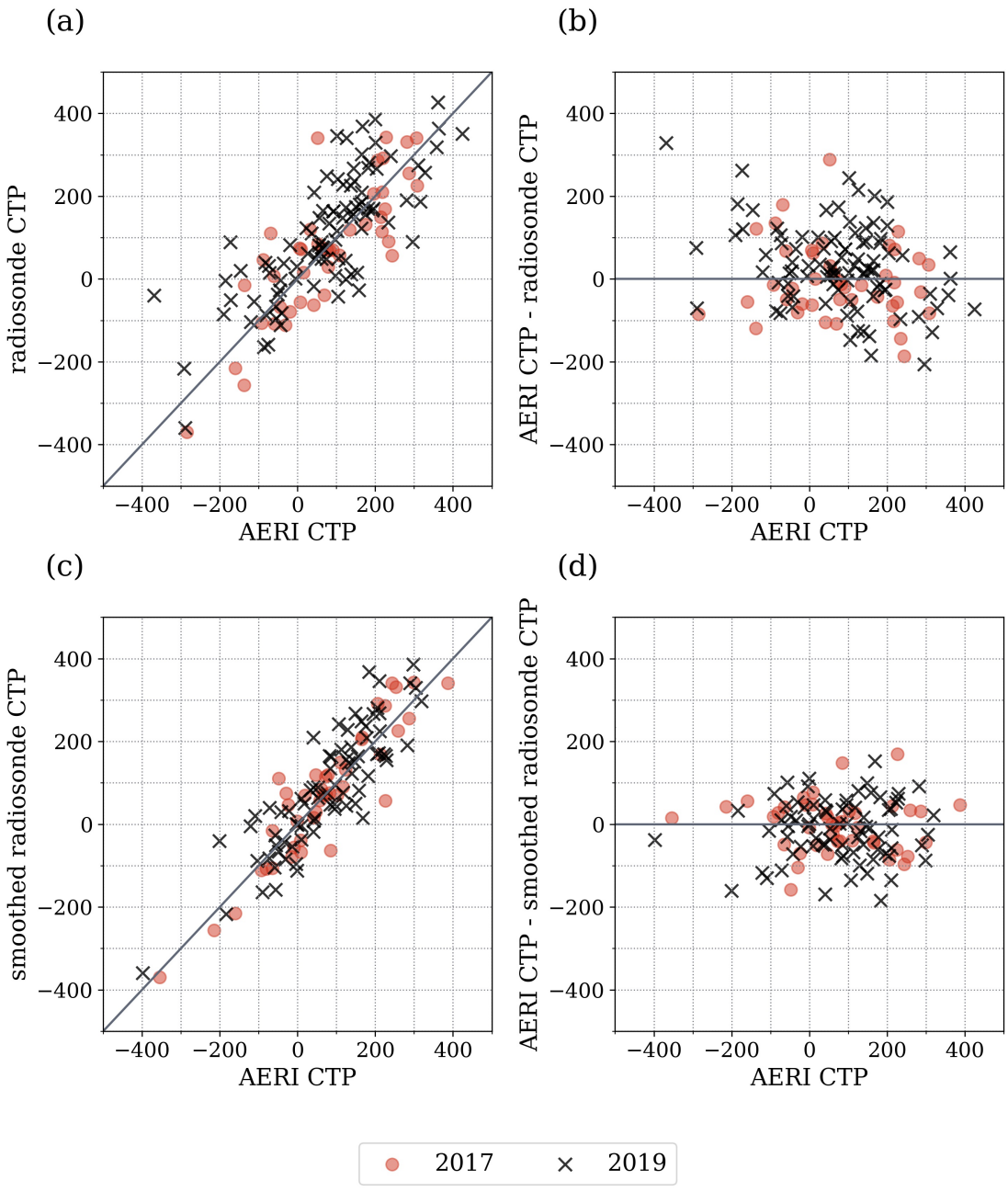

Figure 2.3: As in Figure 2.2, but for CTP.

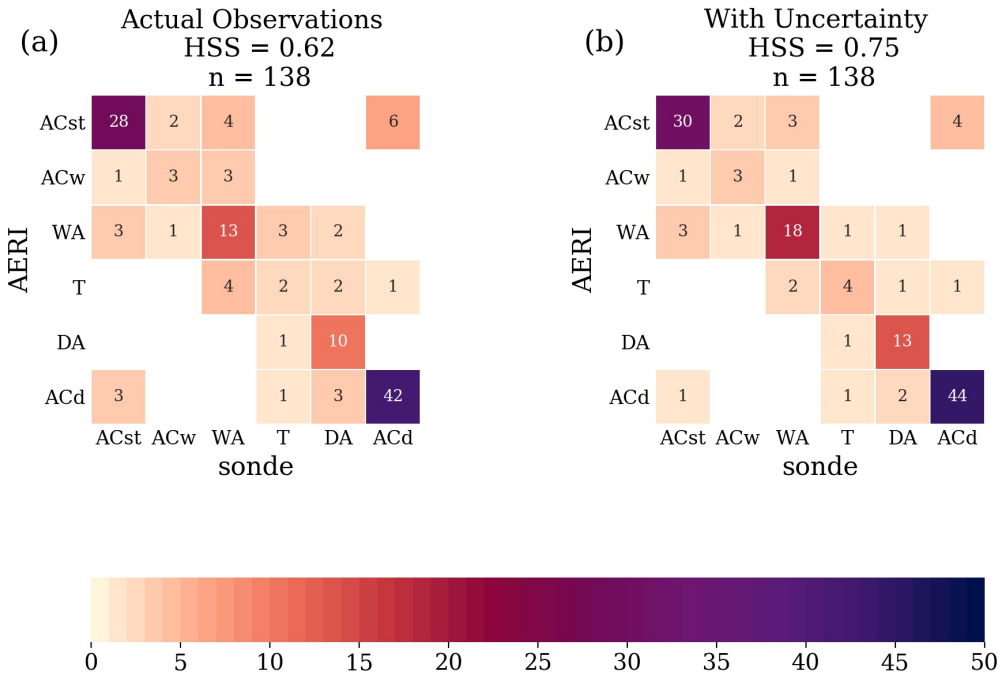

Figure 2.4: Contingency matrix comparing CTP-HI classifications obtained based radiosonde versus AERI CTP-HI observations and Heidke Skill Scores (a) without window of uncertainty and (b) including AERI window of uncertainty. The colorbar corresponds to number of counts, while this number is also annotated directly within the matrix.

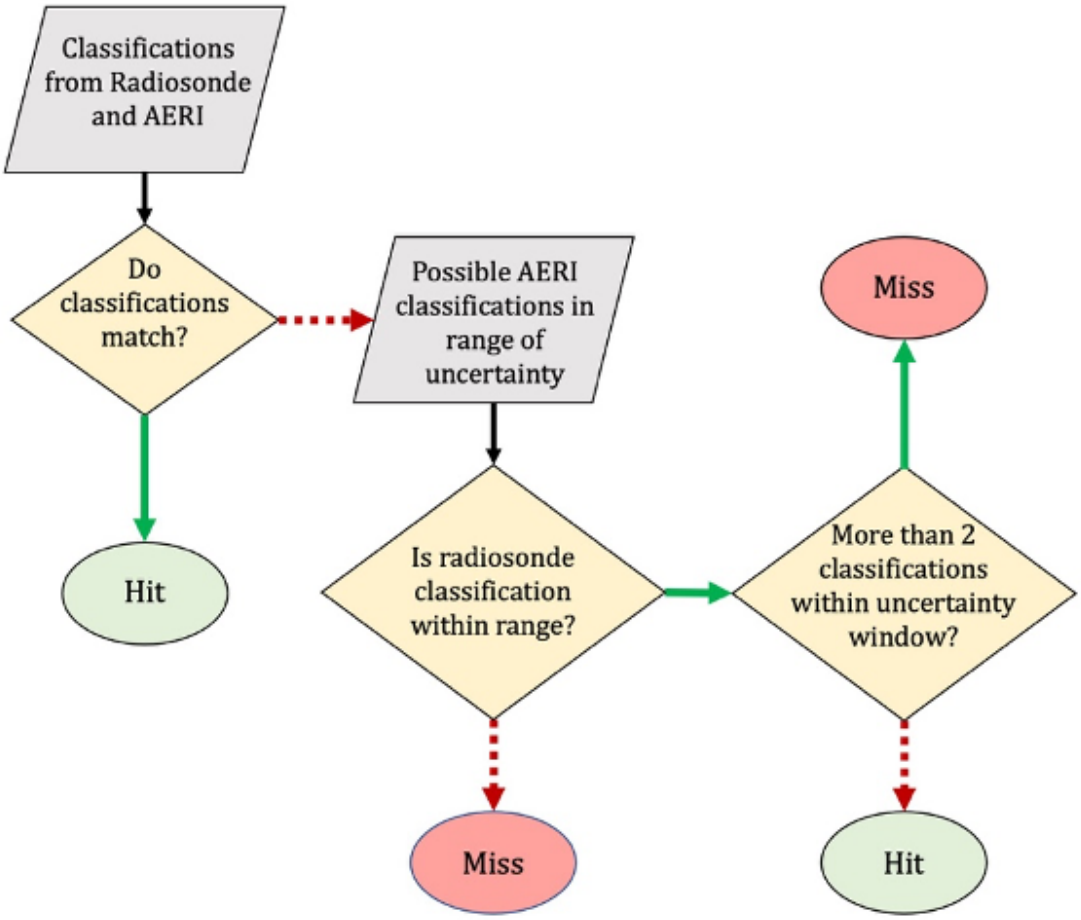

Figure 2.5: Flowchart for computing contingency matrix with uncertainty. Green arrows represent "yes" and red dashed arrows represent "no."

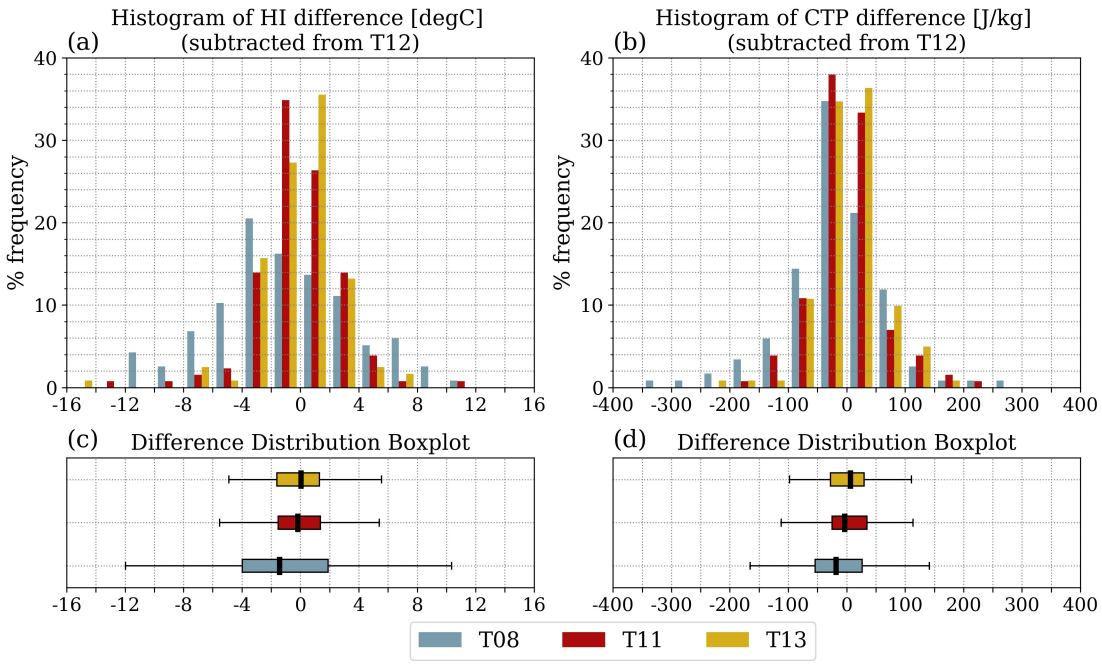

Figure 2.6: Histogram of temporal differences between (a) HI and (b) CTP, and boxplots displaying median and interquartile range of temporal differences for (c) HI and (d) CTP computed for T12-T08 (blue), T12-T11 (red) and T12-T13 (yellow).

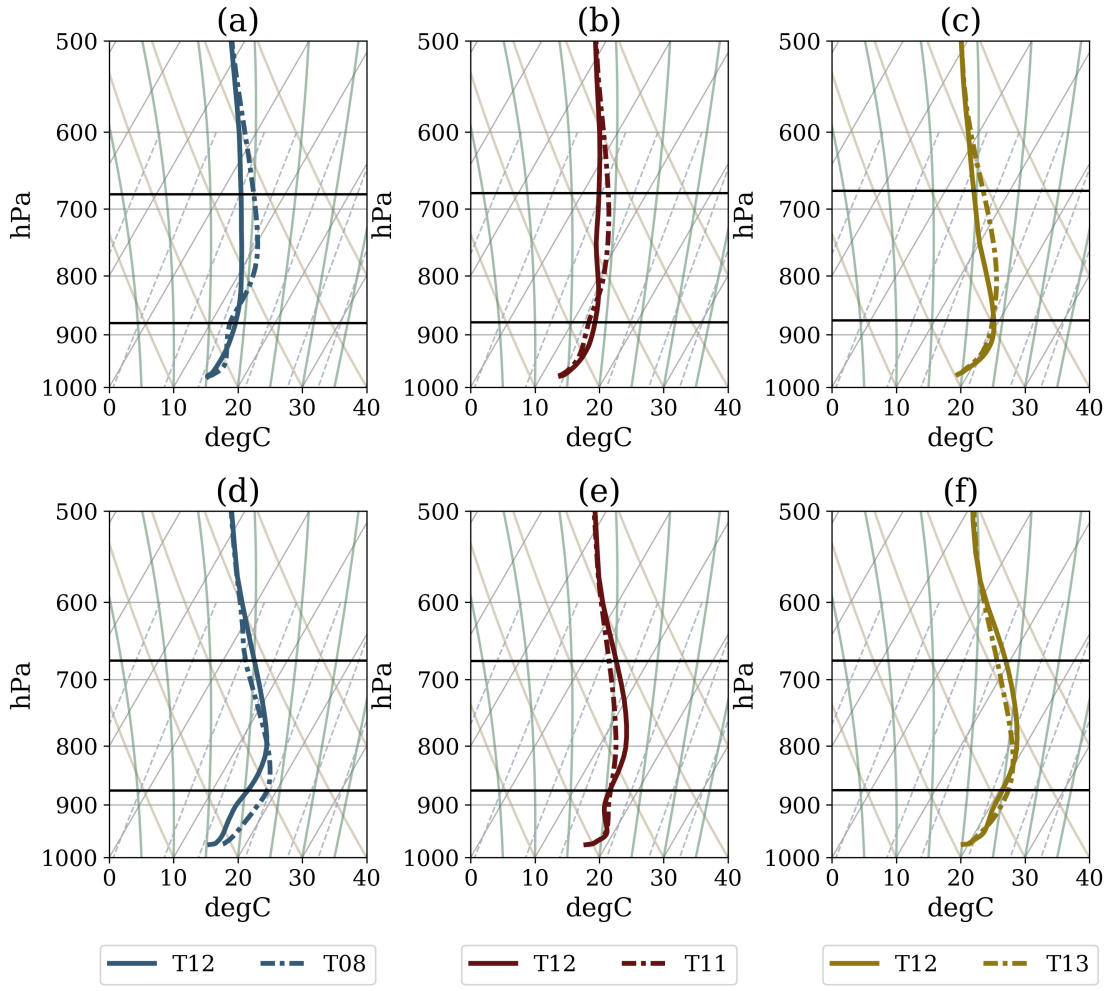

Figure 2.7: Composite temperature profiles for days with the greatest temporal difference (CTP at T12- CTP at Tn) in CTP for differences (a-c) above the 95th percentile and for differences (d-f) below the 5th percentile. Black horizontal lines represent the 100 mb AGL and 300 mb AGL levels.

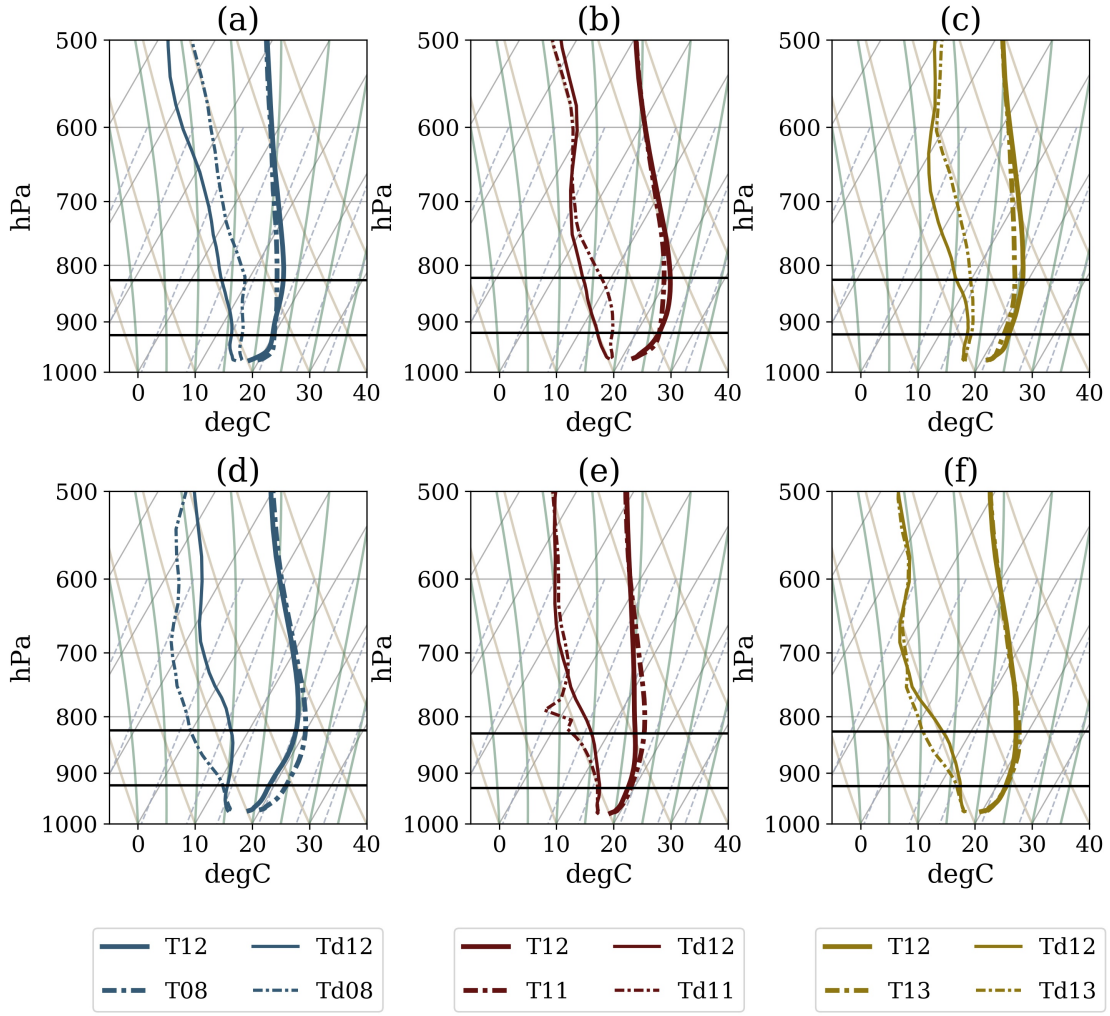

Figure 2.8: As in Figure 2.7 but for HI difference distributions and with the inclusion of dewpoint profiles. Horizontal black lines represent the 50 mb AGL and 150 mb AGL at which dewpoint depressions for HI computations are measured.

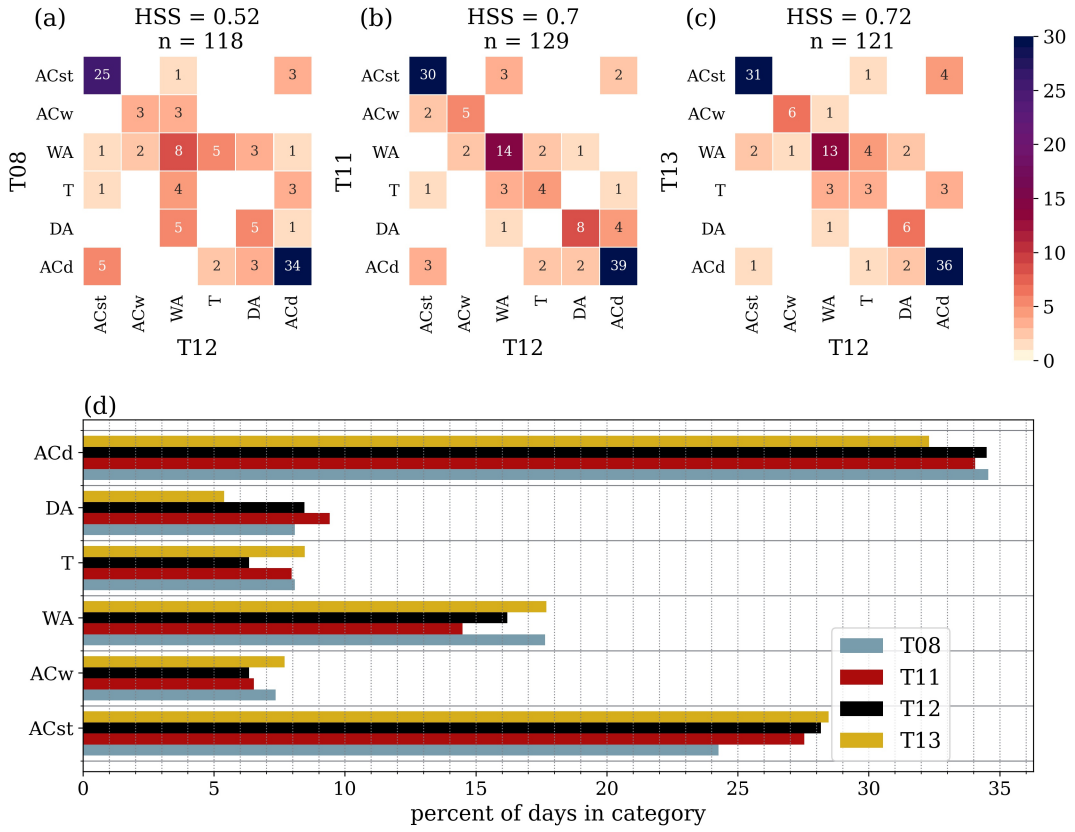

Figure 2.9: (a-c) Contingency matrix of classifications based on CTP and HI combinations for 1100-1200 UTC (+0) versus (a) 0600-0700 UTC (-5) (b) 1000-1100 UTC. (-1) and (c) 1200-1300 UTC (+1). Abbreviations for each classification are provided in section 3.1. (d) percentage of days in each category for each time window.

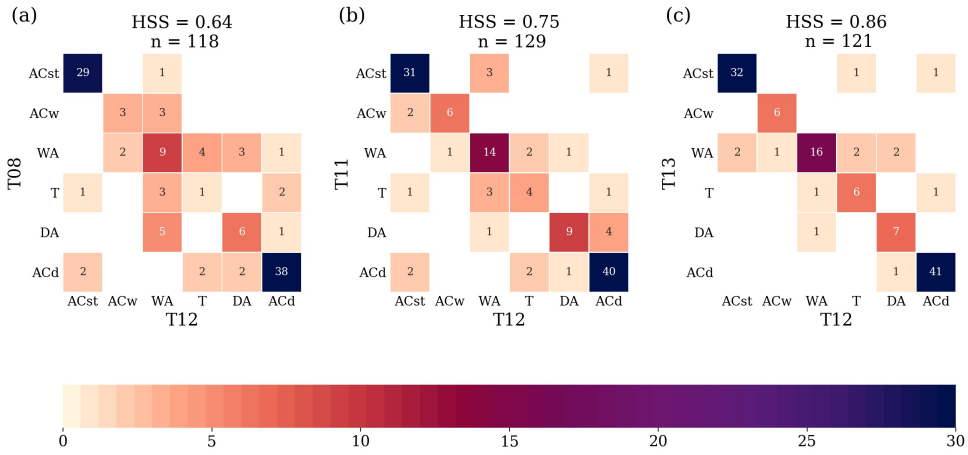

Figure 2.10: (a-c) As in Figure 2.9 a-c, but comparing classifications at T12 to those within windows of uncertainty for (a) T08 (b) T11 and (c) T13.

Chapter 3

Evaluation of a land-atmosphere coupling metric computed from a ground-based infrared interferometer Part II: Boundary layer moisture and energy budget analysis

3.1 Introduction

Chapter 2 introduced the CTP-HIlow framework, which provides an estimate of atmospheric preconditioning toward convection over wet or dry soils. However, the metric is limited to application at a single time, before the daytime PBL develops, rendering it less useful for capturing the co-evolution of the land surface and PBL over the course of an entire day. However, mixing diagrams are a useful tool that can provide such information.

Mixing diagrams (Betts 1992; Santanello et al. 2009; Santanello Jr et al. 2011) combine information about surface fluxes and the atmospheric state of the PBL to quantify the relative contributions of the land surface to the diurnal evolution of boundary layer temperature and moisture. The strength of this framework lies in its applicability to both observational and modeling based land-atmosphere coupling studies, and in its ability to capture the co-evolution of surface and atmospheric processes. Conversely, the framework relies on observations of 2-meter potential temperature and specific humidity to represent the evolution of the entire PBL moisture and energy budget, and thus, operates on the assumption that 2-meter observations are representative of the entire mixed layer. The use of surface meteorological observations was motivated by the relative abundance of such observations in both space and time (Santanello et al. 2009). Using a more representative mixed-layer average temperature and humidity would severely limit this framework's applicability to only those locations where vertical profiles of the atmosphere may be obtained multiple times between the traditional 1200 UTC and 0000 UTC radiosonde launches. As

shown in Chapter 2, the temporal resolution of the AERI and the ability to deploy AERI instruments where radiosonde observations are absent, makes it possible to reconsider the mixing framework's original design. As such, a modified application of the mixing diagram framework, uniquely enabled by AERI observations, is introduced in this chapter.

3.2 Framework Description

Mixing diagrams were first introduced by Betts (1992) and further modified by Santanello et al. (2009) to describe the heat and moisture budgets within the boundary layer. These diagrams attempt to separate the surface, entrainment, and advective contributions to the overall moisture and temperature composition of the boundary layer during daytime hours (i.e. 1200 to 2400 UTC in North America).

The co-evolution of temperature and moisture are represented by a curve in which each point along the curve represents the temperature and moisture content of the PBL at a given time. For example, given 3-hourly radiosondes, a curve from 1200 to 2400 UTC would be found using observations at 1500, 1800 and 2100 UTC with 1200 and 2400 UTC serving as the end points. The mixing diagram shows the 2-m specific humidity multiplied by the latent heat of vaporization (L_v) as the abscissa and the 2-m temperature multiplied by the specific heat (C_p) as the ordinate.

Each component of the moisture and energy budget is represented by a vector. The total vector quantifies the total change in moisture and temperature from the beginning to the end of the period, with the x-component representing changes in moisture and the y-component representing changes in temperature. A conceptual diagram to demonstrate these quantities is provided in Figure 3.1.

Surface vectors are a result of the mean surface fluxes during the period scaled by the mean boundary layer depth. The x-component of this vector can be found by finding the mean latent heat flux ($\overline{LHF_{sfc}}$) over the period of interest, multiplying this by length of the period in seconds, and scaling by the mean boundary layer depth (PBLH) and mixed-layer

density (ρ_m) as shown in (3.1) where $L_v \Delta q_{sfc}$ represents the surface flux component of the PBL moisture budget and L_v is the latent heat of vaporization.

$$L_v \Delta q_{sfc} = \frac{\overline{LHF_{sfc}} \times \Delta t}{\rho_m PBLH} \tag{3.1}$$

Similarly, the surface sensible heat flux component of the energy budget ($C_p \Delta \theta_{sfc}$) can be found from (3.2) where H_{sfc} is the mean sensible heat flux over the period and C_p is the specific heat.

$$C_p \Delta \theta_{sfc} = \frac{\overline{H_{sfc}} \times \Delta t}{\rho_m PBLH} \tag{3.2}$$

Surface fluxes and PBLH are both averaged over the entire period. Santanello et al. (2009) have shown that using a stepwise integration of these values by timestep does not produce a drastically different result. Therefore, when observations of PBLH are limited in temporal resolution, this approximation can be useful.

Finally, the height of the PBL is an essential piece of information in the analysis as surface fluxes are scaled over the depth of the PBL. PBL heights were computed from AERI profiles via the retrieved potential temperature at the surface and adding a factor of 1-σ in uncertainty, then an additional 0.5°, to account for noise in the retrieval temperature estimates, was added to this surface measurement. A parcel was then lifted dry adiabatically until it intersected the potential temperature profile, and this level was determined to be the PBLH. Radiosonde-derived PBLH estimates were computed using the same process.

The mixing diagram framework can benefit from AERI observations in a couple of ways. First, PBLH can be estimated with greater temporal frequency from thermodynamic profiles, and second, it is possible to examine the moisture and energy budget evolution using mixed-layer averages of potential temperature and specific humidity instead of 2-meter observations. Surface meteorological and flux observations as well as radiosonde profiles from the Atmospheric Radiation Measurement (ARM) Program's Southern Great Plains site (SGP) were used in conjunction with AERI observations to test multiple approaches to

the mixing diagram framework and to introduce a refined methodology applied to model simulation data in Chapter 5.

3.3 Data

3.3.1 Site selection

This study uses the same AERI and radiosonde observations from the same location and period used in Chapter 2. A greater focus in this study was placed on observations from 2019 when 3-hourly radiosondes were available as a result of the Micropulse Dial IOP. Higher temporal resolution radiosonde observations were desirable to more comprehensively evaluate PBL budget evolution.

3.3.2 ECOR: Eddy Correlation Flux Measurement System

Surface latent and sensible heat flux observations were obtained from the Eddy Correlation Flux Measurement System (ECOR; Cook and Sullivan 2020) at the E14 site that is collocated with the ARM central facility. The system uses the eddy covariance technique to provide observations of latent and sensible heat fluxes every 30 minutes.

3.3.3 Surface meteorological station

Surface meteorological variables were obtained from the ARM Sothern Great Plains Surface Meteorology Systems (SGPMET; Ritsche 2011) station located at the E13 site, which is also collocated with the ARM central facility. Temperature and relative humidity at 2 meters were measured by the Vaisala HMP45C temperature and relative humidity probe with relative humidity accuracy of 2-3% and temperature accuracy of 0.2at 20and 0.3at 40(https://www.campbellsci.com/hmp45c-l).

3.4 Methods

3.4.1 Observational analysis

The mixing diagram framework uses 2-meter temperature and humidity to compute the overall mixing diagram curve as well as the total vector and assumes that these values are representative of a well-mixed PBL. This is, in part, due to the widespread availability of 2-meter temperature and humidity observations. It is hypothesized that using mixed-layer averages of these quantities makes closure of PBL moisture and energy budgets more attainable. Even so, mixed layer averages with the same temporal resolution afforded by 2-meter observations are difficult to obtain. AERI offers the unique ability to compute these mixed layer average temperature and humidity profiles.

The mixed layer over which temperature and specific humidity were averaged was defined as the layer between 0.1 z_i and 0.75 z_i, where z_i is the PBL height (PBLH). The lower limit of this layer was selected to avoid the surface layer which is typically within the lowest 10% of the PBL while the 0.75 z_i upper bound should reduce influences from entrainment fluxes (Stull 1988). Mixed layer mean values were computed for both the radiosonde and AERI profiles.

Surface flux inputs remain the same for each observational platform, and differences in PBLH derived from the AERI versus radiosonde data are the primary driver of differences in surface vectors. This is because residual vectors as fluxes are scaled to the depth of the PBL. PBL depth also influences the layer in which mixed layer averages of temperature and humidity are obtained as the mixed layer bounds are a direct function of PBLH. Therefore, the analyses presented hereafter will focus primarily on the uncertainties associated with AERI versus radiosonde boundary layer heights as well as mixed-layer profiles.

The traditional mixing diagram framework averages daily latent and sensible heat fluxes and scales these to the average depth of the boundary layer for the period of interest in order to compute the surface flux vector. As such, hour to hour differences in radiosonde

versus AERI PBLH observations may be smoothed by this averaging. The difference between using an hourly stepwise integration of the PBLH scaled fluxes versus using an average over the entire period should not result in a significant difference between the two approaches for the same instrument (Santanello et al. 2009). Even so, both approaches to the mixing diagram framework were tested in addition to comparison of results for both radiosonde and AERI based mixing diagrams. While AERI and surface flux observations were available hourly, the greatest temporal resolution afforded by radiosonde observations was 3-hourly during the 2019 IOP. As such, daily averaged values of surface fluxes and PBLH were compared with values obtained from the highest temporal resolution stepwise integration afforded by the specific observational platform. It is anticipated that the greatest differences in PBL budget representation will be related to uncertainties and differences between the profiling platforms themselves regardless of approach as differences in PBLH estimate will drive differences in the scaling of fluxes over the depth of the PBL.

Although there are numerous potential days for analysis during the 2017 and 2019 periods, only two cases were selected for this proof-of-concept study. Case selection was intended to capture two different PBL regimes to ensure that the final methodology could sufficiently capture a wide range of evolution in PBL moisture and energy budgets. The first date selected was 12 June 2019, which was characterized by equal partitioning between surface latent and sensible heat fluxes and an overall warming and drying of the PBL. The second date, 20 June 2019, was primarily influenced by high surface latent heat fluxes and a late afternoon/early evening moistening of the PBL.

3.5 Results

3.5.1 12 June 2019

Mixing diagrams computed from AERI observations and from radiosonde observations (Fig. 3.2) both portray the overall drying and warming of the PBL that was observed during the daytime hours as represented by the $L_v q$ versus $C_p \theta$ curves. Surface Bowen ratios

were nearly identical for both radiosonde and AERI based mixing diagrams and indicate a greater partitioning of energy into evaporation. Given surface fluxes alone, warming and moistening of the PBL would be expected rather than the observed warming and drying. As such, the residual vector (red) indicates that entrainment and advective fluxes of dry air played a critical role in the observed drying of the PBL.

Using the daytime average (Fig. 3.2a) versus temporally integrated (Fig. 3.2b) approach did not result in significant differences between mixing diagrams, and Bowen ratio values were nearly identical between cases. Vector magnitudes (Fig. 3.3) for radiosonde based mixing diagrams were consistently less than those of AERI mixing diagrams with the exception of the surface vector magnitudes for the time integrated case. As such, reduced magnitudes did not result in great differences in the overall representation of the moisture budget between platforms since the radiosonde vector magnitudes were consistently lesser than those of the AERI. This is further evidenced by little difference in Bowen ratios for each vector shown in figure 3.3.

Upper and lower bounds for the mixed layer are dependent upon z_i or PBL depth. Even if radiosonde and AERI thermodynamic profiles were nearly identical, differences in PBL depth could contribute to differences in mixed layer averages. Additionally, while the exact same surface flux measurements were used for AERI and radiosonde mixing diagrams, these fluxes are scaled to the depth of the PBL. On this particular day, both AERI and radiosonde PBLH were very similar (Fig. 3.4), contributing to the good agreement between mixing diagrams. As such, any differences in the mixing diagrams was likely related to differences in the thermodynamic profiles. Agreement in PBLH is slightly reduced at the end of the period, though this may be related to the evening transition of the boundary layer. As such, limiting the period of interest to when surface fluxes are above a certain threshold could mitigate this issue. Using a flux-threshold based approach further supports the case for AERI thermodynamic profiles as the 0000 UTC radiosonde may fall outside

the bounds of the new time period, and there would be insufficient information to compute a mixing diagram.

3.5.2 20 June 2019

Analysis of 20 June 2019 provided contrasting PBL evolution in comparison to 12 June 2019 and was characterized instead by warming and moistening of the PBL in addition to greater initial moisture content (Fig. 3.5). Much of the PBL moistening was concentrated later in the day and was successfully portrayed by both radiosonde and AERI mixing diagrams. AERI mixing diagrams showed initially drier conditions than those obtained from radiosondes, but the overall shape was similar between the two. Furthermore, the final temperature and moisture was nearly identical between the two platforms at the end of the period. Surface flux partitioning was overwhelmingly dominated by evaporation, and once again, the choice of daytime averaged, versus time integrated approaches resulted in little difference in surface vector Bowen ratios and magnitudes (Fig. 3.6).

The differences between radiosonde and AERI mixing diagrams was further explored by examining 3-hourly vertical profiles obtained from each instrument (Fig. 3.7). From 1200 to 1800 UTC, AERI showed lower mixed layer moisture content, but by 2100 UTC both AERI and radiosonde moisture profiles were in good agreement. It is also evident that vertical resolution played a role in some of these differences, especially earlier in the day. Once the PBL was well-mixed, the AERI performed well, as some of the finer scale variations observed in the radiosonde vertical moisture profile during earlier times became more uniform due to mixing.

The AERI's ability to estimate PBLH accurately (Fig. 3.8) played a key role in creating nearly identical representation of surface flux partitioning in mixing diagrams. Consequently, differences in PBLH were insufficient to create major discrepancies between mixing diagrams. Mixed layer averages would be obtained over nearly the same layer for radiosonde and AERI profiles. This further supports the assertion that the differences in

mixing diagram curves observed early in the period are directly related to differences in thermodynamic profiles shown in Figure 3.7.

The initial difference between radiosonde and AERI representation of the mixing diagram curve had an impact on the computation of the residual vector. Total vectors represent the change in moisture and energy budget of the PBL from beginning to end of the daytime cycle, and therefore, differences at the start of the period resulted in smaller total vector magnitudes for the radiosonde mixing diagrams. Computation of the residual vector is sensitive to the magnitudes of the surface and total vectors, and therefore residual vectors also differed between the AERI and radiosonde mixing diagrams.

Radiosonde total vectors displayed higher Bowen ratios than AERI total vectors, indicating a greater change to the PBL energy budget than to its moisture budget. At the start of the period, radiosonde moisture was already greater than that observed by the AERI, while at the end both platforms were nearly identical. As such, a greater overall change in the AERI moisture budget was necessary to achieve a similar final moisture content to the radiosonde observations. Conversely, radiosonde PBL temperatures were cooler than that of AERI temperatures, such that greater input into the PBL energy budget was necessary for final radiosonde temperature to match that of the AERI.

Given a moister starting point in the radiosonde mixing diagram, and a surface vector with nearly identical magnitude to that obtained from the AERI, more drying had to occur as a result of entrainment and advection to achieve the same final moisture and temperature content as the AERI. Conversely, surface fluxes of moisture appeared to dominate the evolution of the AERI PBL moisture budget, and little contribution of advection or entrainment was necessary. This is reflected in the different Bowen ratios for the AERI and radiosonde residual vectors. Residual vectors in the radiosonde and AERI mixing diagrams suggest that advection and entrainment fluxes primarily contributed to warming of the PBL. These vectors also provide contrasting depictions of the role advection and entrainment fluxes played in the PBL moisture budget.

3.6 Discussion

Mixing diagrams are a useful tool that can provide detailed information about daytime PBL evolution and can benefit from AERI observations in a couple of ways. First, PBLH can be estimated with greater temporal frequency from thermodynamic profiles, and second, it is possible to examine the moisture and energy budget evolution using mixed-layer averages of potential temperature and specific humidity instead of 2-meter observations. Past applications of the mixing diagram framework use 2-meter observations as they are far more prevalent in time and space than vertical profiles of the same meteorological variables (Santanello et al. 2009).

Using a mixed-layer approach means that twice daily soundings are insufficient for application of the mixing diagram framework to observations, and even the 6-hourly soundings at the ARM SGP site would provide a limited picture of the PBL evolution between 1200 and 0000 UTC. Therefore, the temporal resolution of the AERI is optimal for application of this framework. Two case studies were selected during 2019 to showcase the utility of the AERI in this particular application. These cases were selected because sounding data was available at 3-hourly instead of 6-hourly intervals during the period to better compare radiosonde and AERI based mixing diagrams, and both days showed well-developed mixed layers. Furthermore, the two days were selected to contrast one another as the PBL evolution on the 12^{th} was characterized by warming and drying throughout the day. Conversely, the PBL moistened and warmed on the 20^{th}. Both days also displayed differing starting temperature and moisture conditions, such that the AERI and radiosonde portrayal of PBL evolution could be compared for two different extremes.

Overall the AERI and radiosonde mixing diagrams matched well and support the idea that the AERI can provide a representative picture of diurnal PBL evolution in locations where radiosonde data is not available and can provide a valuable tool for studying land-atmosphere coupling. From the two cases presented, a few key points can be made:

1. The AERI performs well at matching the overall shape of the radiosonde mixing diagram curve for days that are characterized by moistening and by drying.

2. Both radiosonde and AERI PBL heights show strong agreement overall, which creates greater consistency in the surface flux vectors as they are a result of normalizing the surface fluxes over the depth of the boundary layer.

3. Using stepwise integration of surface fluxes versus daily means does not lead to significant differences in surface flux vectors, consistent with Santanello et al. (2009).

4. Weakened rapidly following landfall and did not undergo extratropical transition.

5. Residual vectors are sensitive to both the magnitude, and direction of the total vectors and surface vectors, but because the surface flux vectors show little variability, it is the magnitude and direction of the total vectors that created the greatest differences both between observing platforms and within mixing diagrams obtained from the same platform. Because the residual vector captures both entrainment and advection contributions to the overall evolution of the PBL, this may lead to misattribution of the relative role that surface fluxes play in the moisture and energy budget of the PBL.

3.7 Conclusions

In regions where upper air observations are performed only twice per day, the AERI can be used to provide a wealth of information about the PBL evolution in between those two times and can be used to better quantify land-atmosphere interactions in such locations. When co-located with surface flux observations, the relative contributions of sensible and latent heat fluxes to the moisture and energy budget of the boundary layer can be evaluated, even when there are no nearby upper air observing stations. Moreover, the higher temporal resolution of the AERI facilitates comparison with high temporal resolution model simulation output,

and will be used in the future to verify operational forecast model representation of PBL moisture and energy budget components.

Some limitations of the mixing diagram analyses are driven by a lack of information about advection. Chapter 5 will incorporate estimates of advection from numerical model output and reanalysis data to better quantify the role of entrainment in the overall PBL evolution. Ongoing work by collaborators suggests that a network of several AERIs at the ARM SGP site can be leveraged to derive advection, which would allow for advective fluxes to be separated from the residual vector, enabling refinement of entrainment flux estimations. However, the observational aspect of the advection work is beyond the scope of this study. Application of advection obtained from model simulation output will be introduced into the framework in Chapter 5.

The high temporal resolution of the AERI also enables application of the mixing diagram coupling metric. Mixing diagram quantities display some sensitivity to both the morning and nocturnal transitions but the AERI's high temporal resolution would allow for the starting and ending times of the mixing diagram observations to be altered to omit these transition periods. Future analyses may also divide mixing diagrams into smaller temporal ranges to quantify the evolution of the PBL while it is actively developing and while it is steady state. Vertical profiles of temperature and moisture are often incorporated into land-atmosphere coupling metrics which can limit their applicability from an observational perspective as the temporal and spatial coverage of atmospheric profiles is sparse. The AERI can be used in such locations to better observe land-atmosphere coupling, and these observations may also be used to verify model representation of land-atmosphere coupling in locations where such comparisons were not previously possible.

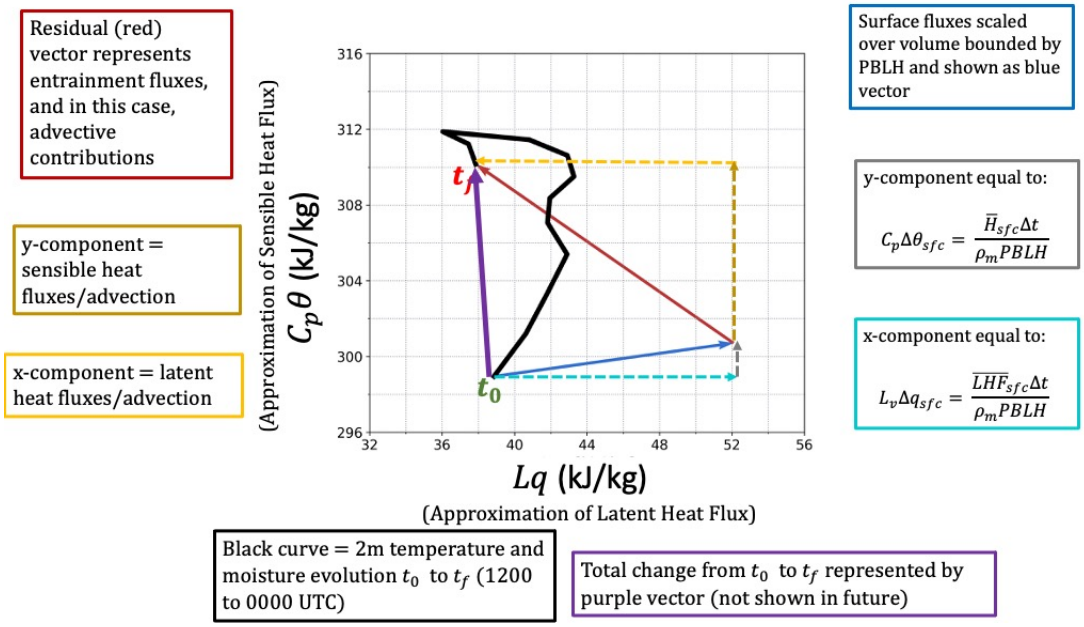

Figure 3.1: Conceptual diagram describing the Mixing Diagram Framework (Santanello et al. 2009.

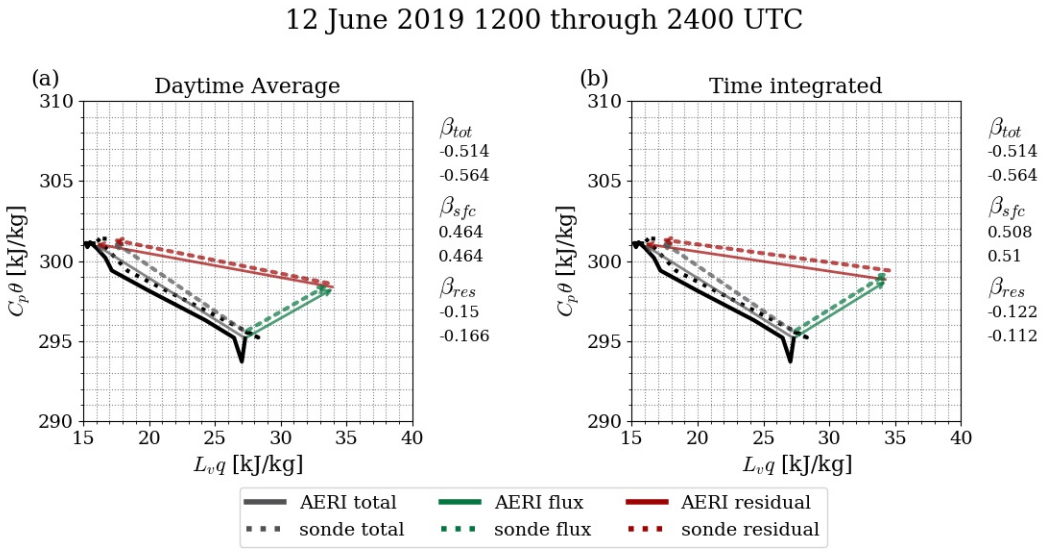

Figure 3.2: Mixing diagrams for 12 June 2019 derived from AERI vertical profiles consisting of (a) mixing diagram computed using mixed layer temperature and humidity, where surface flux vector was computed by normalizing daily average latent and sensible heat fluxes over the daily averaged PBL depth. (b) as in (a) except surface flux vector was computed from stepwise integration of surface fluxes over time. Residual vectors were obtained by subtracting surface vectors from total vectors. Total vectors are the same in both plots, but because the surface vectors change, so do the residual vectors. *Dashed lines represent mixing diagrams obtained from radiosonde profiles instead of AERI profiles.*

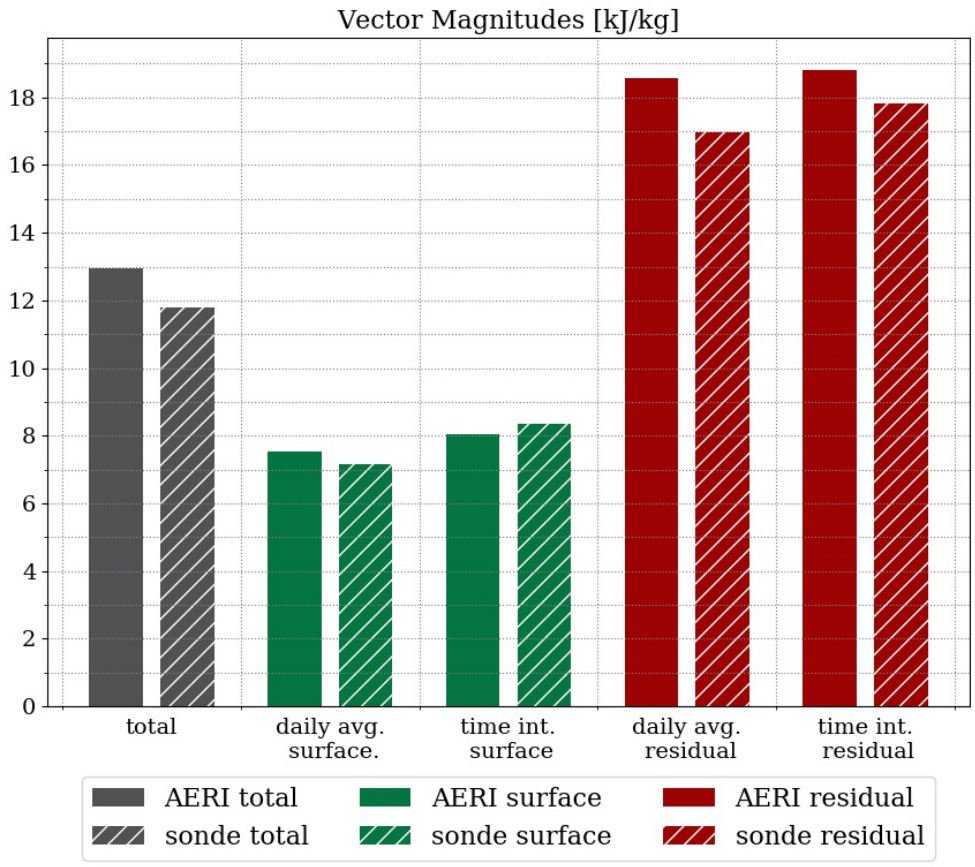

Figure 3.3: Vector magnitudes for mixing diagram vectors on 12 June 2019. Magnitudes for both the daily averaged vectors and time integrated vectors are both shown. Solid bars represent AERI vectors while hatched represent radiosonde vectors.

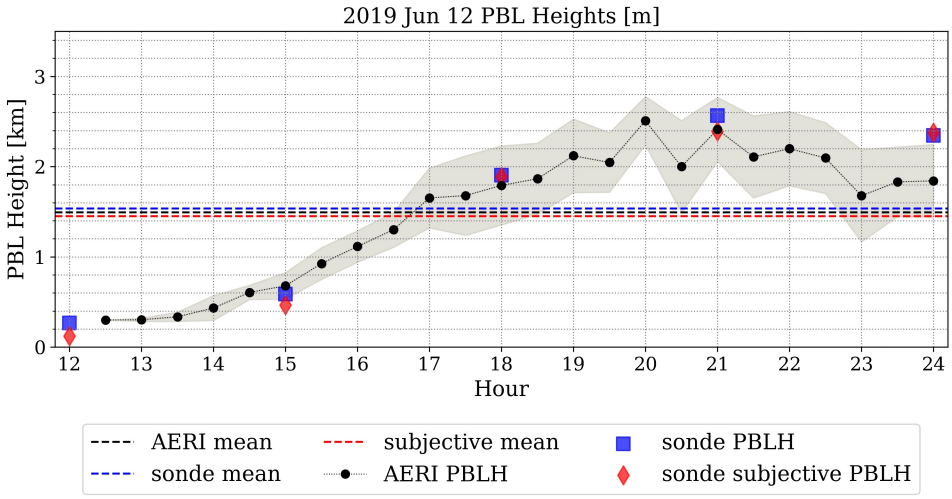

Figure 3.4: AERI versus radiosonde estimates of boundary layer height (PBLH) on 12 June 2019. Gray represents 1 standard deviation in uncertainty for the AERI PBLH. Dashed horizontal lines represent the mean over the entire period. Subjective PBLH and mean were PBLH which were identified manually.

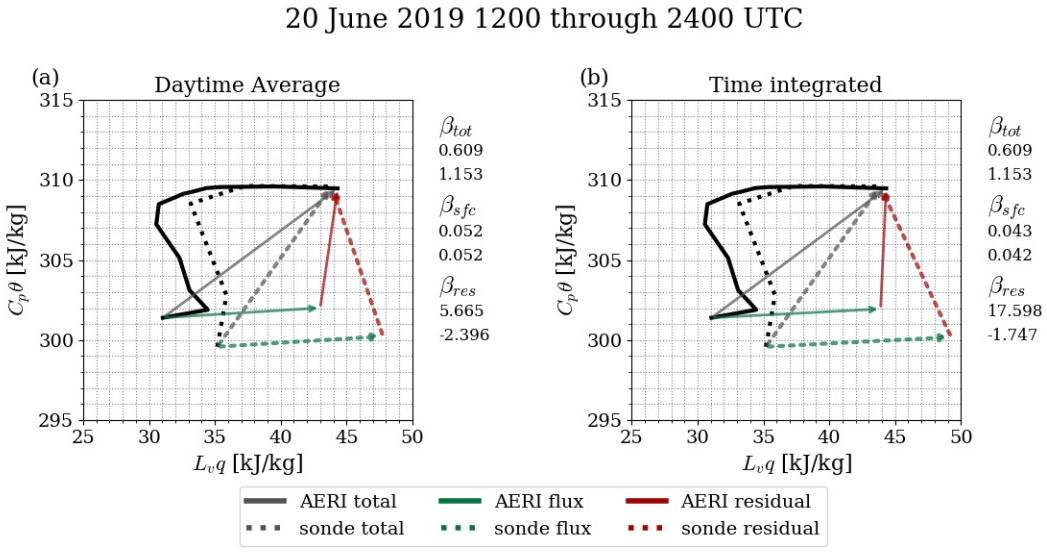

Figure 3.5: As in Figure 3.2, but for 20 June 2019.

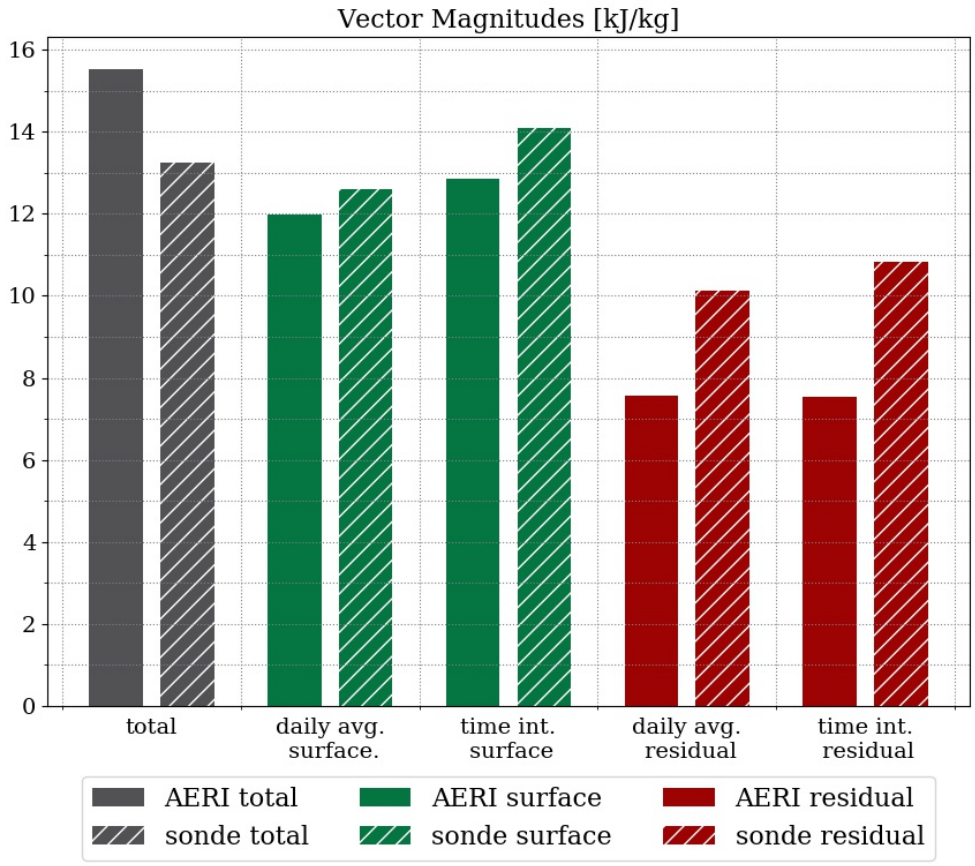

Figure 3.6: As in Figure 3.3 but for 20 June 2019.

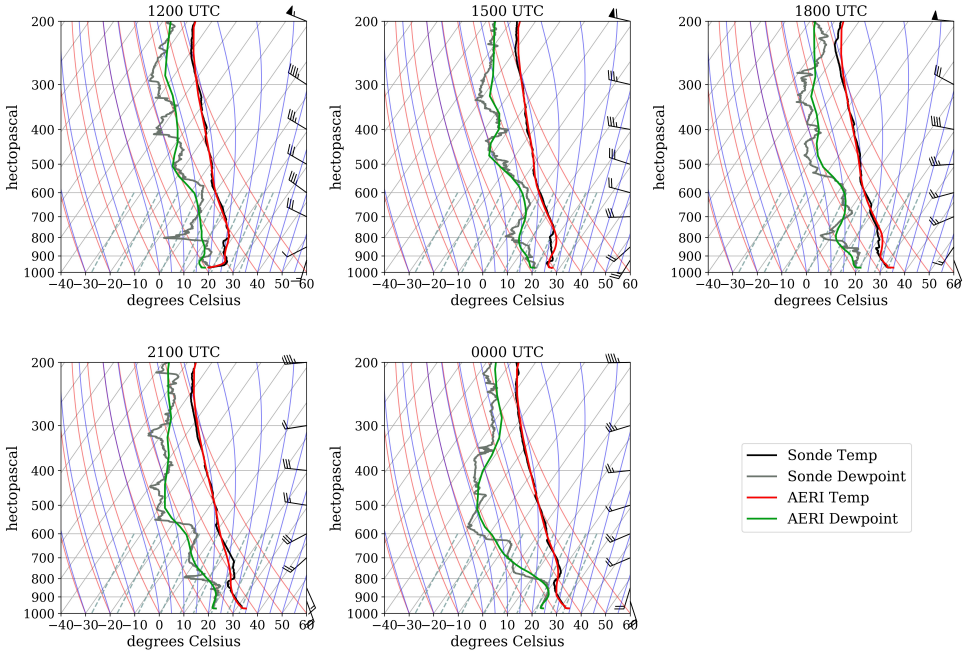

Figure 3.7: Vertical profiles of temperature and moisture at 3-hourly intervals on 20 June 2019. Black (red) represents radiosonde temperature observations and gray (green) represents radiosonde dewpoint observations. Wind speed and direction were also obtained from radiosonde observations.

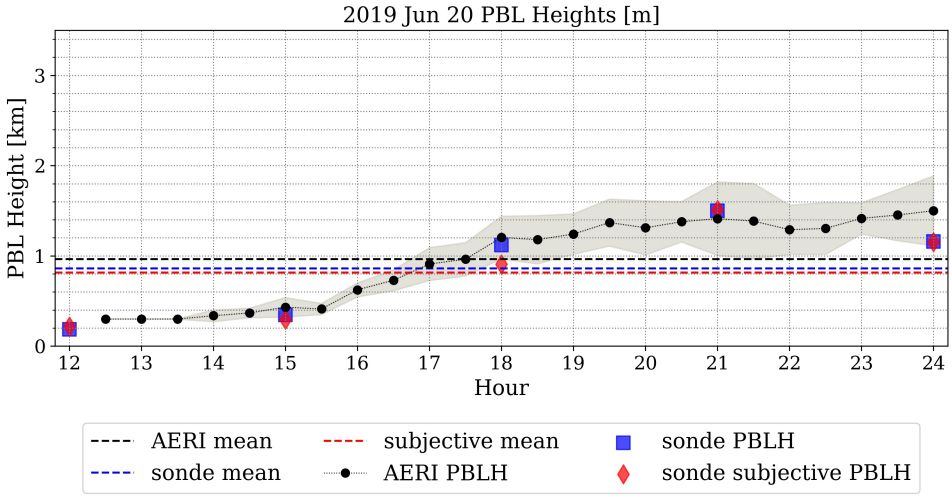

Figure 3.8: As in Figure 3.4, but for 20 June 2019.

Chapter 4

The Inland Maintenance and Reintensification of Tropical Storm Bill (2015) Part 1: Contributions of the Brown Ocean Effect

4.1 Introduction

Soil moisture can play a role in the development of weather and climate extremes, particularly within continental regions comprised of a transition zone from humid to drier climates such as the Southern Great Plains (Guo et al. 2006; Koster et al. 2004, 2006; Dirmeyer 2006). In these regions a greater sensitivity of the overlying atmosphere to surface fluxes is observed, reinforcing precipitation anomalies. Changes to land use and land cover can also impact precipitation extremes. This is evident even in arid regions where afforestation can provide localized rainfall enhancement (Yosef et al. 2018; Branch and Wulfmeyer 2019). Elsewhere, anthropogenic land use changes have been linked to reductions in precipitation a result of increased irrigation and agricultural use in the Indian Monsoon region (Niyogi et al. 2010). Thus, the land surface can even impact larger scale atmospheric circulations. Antecedent rainfall has been associated with further inland penetration of landfalling monsoon depressions (Kishtawal et al. 2013) and has also been shown to increase their intensity (Chang et al. 2009). Dastoor and Krishnamurti (1991) showed that more accurate parameterization of soil wetness produced more accurate simulations of rainfall associated with these circulations. Landfalling tropical cyclones may be similarly impacted by soil wetness and other land surface characteristics. Tropical cyclones (TC) are fueled by fluxes of heat and moisture from the surface, in particular, warm sea surface temperatures (e.g., Emanuel et al. 2004). Reduction in evaporation upon landfall contributes to tropical cyclone decay over land (Tuleya and Kurihara 1978; Tuleya 1994) though landfalling TCs may be sustained by fluxes of heat and moisture from the land surface even as they move away from

oceanic sources of energy. This phenomenon is referred to as the Brown Ocean Effect (Andersen et al. 2013).

Post-landfall intensification of TCs is typically a result of the storm interacting with a midlatitude baroclinic zone and transitioning to an extratropical cyclone (Hart and Evans 2001; Jones et al. 2003; Evans et al. 2011). Occasionally landfalling TCs maintain their warm-core structure and may re-intensify over land despite limited access to oceanic sources of moisture, and in particular, oceanic surface fluxes. In such cases, a moist land surface may provide sufficient fluxes of moisture and energy to re-intensify or sustain a TC. Numerical simulations of landfalling TCs are sensitive to parameterizations of the land surface (Bozeman et al. 2012; Kishtawal et al. 2012). Simulated landfalling TCs still weaken when moving over a water-covered land surface, but they do so more slowly than those over dry land. Moreover, these TCs display a much greater diurnal cycle in convection than TCs over the ocean due to lower heat capacity of shallower water surfaces (Shen et al. 2002).

Emanuel et al. (2008) suggested that daytime heating and moistening of sandy soils from outer rain bands ahead of the path of landfalling TCs in Australia provide sufficient latent heat flux to fuel maintenance or intensification of the TC as it moves further inland. This theory was proposed to explain the inland reintensification of TS Erin over Oklahoma on 19 August 2007 (Emanuel et al. 2008; Kellner et al. 2012). Antecedent rainfall in the region was well above normal; however, in the weeks preceding Erin's landfall, top level soil had dried and warmed markedly along the path such that outer rain bands ahead of Erin could remoisten soils and encourage enhanced latent heat fluxes (Arndt et al. 2009; Monteverdi and Edwards 2010; Evans et al. 2011; Andersen and Shepherd 2014).

This Brown Ocean Effect may play a role in the reintensification of TCs in North America, Asia, and Australia (Andersen et al. 2013). Through a global climatology of inland TC maintenance and/or intensification (TCMI), Andersen et al. (2013) found that latent heat fluxes were much greater in the vicinity of the location of a TCMI during the 3 weeks prior to, as well as during, the TCMI occurrence when compared to TCs that

weakened over land. In other words, antecedent and concurrent surface moisture both play a role in TCMI, via increased latent heat fluxes making it necessary to examine land surface conditions related to TCMI cases at multiple timescales. Furthermore, daytime maximum latent heat fluxes over land during the period preceding TCMI occurrences are often similar in magnitude to latent heat fluxes over the ocean (Andersen and Shepherd 2014). More recently, Nair et al. (2019) found that an unnamed depression responsible for intense flooding in Louisiana may have been enhanced by the Brown Ocean Effect.

Recently, in the United States, both TS Erin (2007) and TS Bill (2015) maintained warm-core characteristics for an extended period of time post-landfall. In both cases, above-normal antecedent precipitation had occurred along the paths of each storm. Previous studies have explored the potential drivers of Erin's reintensification over Oklahoma (Arndt et al. 2009; Monteverdi and Edwards 2010), but there is a dearth of literature regarding the post-landfall evolution of TS Bill. A series of Weather Prediction Center Tropical Advisory Discussions from 2100 UTC on 19 June 2015 to 1500 UTC on 20 June 2015 acknowledged the potential role that antecedent rainfall may have played in Bill's reintensification. However, Zhang et al. (2019) refute this claim, instead suggesting that increased soil moisture would contribute to the weakening of TS Bill post-landfall, through increased vertical mixing, and boundary-layer stabilization. Within the storm environment, beyond the main circulation, diabatic heating effects enhanced vertical vorticity and convective instability supporting a more symmetric structure over land, and thus, maintenance of intensity in a simulated TS Bill Zhang and Wang (2021). Thus, it is important to consider the role of latent heat fluxes within the environment adjacent to the storm itself.

This study uses a combination of existing and novel methods to evaluate the precursor environment along the path of TS Bill to determine whether the Brown Ocean effect aided the inland maintenance and/or intensification of TS Bill. It is hypothesized that anomalously moist soils supported the overland maintenance of TS Bill for more than four days following landfall through anomalous latent heat fluxes, both near the storm's center

and along the trajectories of inflow parcels. The current study implements a multi-step process for assessing whether TS Bill was maintained or reintensified over land as a result of anomalous moisture fluxes from the land surface. Sections 2 and 3 present an overview of TS Bill, the data analyzed and our TCMI classification criteria. Finally, the event was analyzed using three different approaches, and each analysis is grouped with its results in sections 4, 5 and 6. First, the evolution of surface moisture fluxes and atmospheric moisture during the 2-week period leading up to a potential TCMI event was examined, building on metrics from Andersen et al. (2013). Landfalling storms with a similar path that did not undergo TCMI were identified and these results were compared to TCMI cases. Then, the focus shifted toward a shorter timescale and the relative contributions of evapotranspiration to the atmospheric water vapor budget during the 72-hour period preceding TCMI and non-TCMI storms. The third and final part of the analysis evaluated evapotranspiration along the path of inflow parcels for each storm in the study. Discussion and conclusions of results follow.

4.2 Overview and Data

4.2.1 TS Bill (2015)

4.1 summarizes the track of TS Bill. The storm formed on 16 June at 0000 UTC over the Gulf of Mexico and tracked northwestward before making landfall on Matagorda Island, Texas at 1645 UTC. TS Bill's maximum intensity was observed shortly before and following landfall from 1200 to 1800 UTC on the 16th, with a central pressure of 997 hPa and maximum sustained winds at 50 kt (26 m^{-1}). As Bill progressed northward through Texas, it weakened and was re-classified by the National Hurricane Center as a tropical depression at 0600 UTC on 17 June. Despite moving further inland, Bill maintained a central pressure of 999 hPa from 0600 to 1800 UTC on 17 June, though maximum sustained winds decreased from 30 to 25 knots during the same period. Following this period of relatively constant intensity, Bill began to weaken and curved northeastward before being classified

as a remnant low by 1800 UTC on 18 June in eastern Oklahoma. Bill produced rainfall >30 cm in some places (Berg 2015; Stewart 2016) along with 19 tornadoes recorded in the Storm Prediction Center TC tornado data (TCTOR; Edwards 2010) as it tracked over land from 16–21 June. Between 1200 UTC 19 June and 1200 UTC 20 June, Bill's central pressure dropped from 1006 hPa to 1001 hPa as it moved from southern Missouri to northwestern Kentucky. Radar imagery of Bill during this time (not shown) indicated enhanced convective activity to the southeast and a defined cyclonic circulation. According to the Weather Prediction Center (WPC) public advisory archive (Rubin-Oster 2015), satellite imagery also displayed prominent upper-level outflow to the north.

Similar to 2007 when TS Erin reintensified over Oklahoma, 2015 was characterized by anomalously heavy rainfall preceding the arrival of TS Bill. Bill's period of reintensification on the 19th and 20th may have been supported by anomalously wet land surface conditions as upper-level forcing was minimal. Further, TS Bill also displayed a period of near-constant central pressure over northern Texas despite its inland location. As such, this study will also assess the relative contribution of the "Brown Ocean" effect to the maintenance and intensification of TS Bill over land. The objective of this study is not to reassess the existence of the Brown Ocean Effect, but rather to determine whether TS Bill exhibited similar characteristics to other landfalling tropical cyclones which maintained intensity or reintensified over land.

4.2.2 HURDAT2

National Hurricane Center Best Track data, for TS Bill and the other three storms analyzed, was obtained from the publicly available HURDAT2 database (Landsea and Franklin 2013). Latitude, longitude, central sea-level pressure and 1-minute maximum sustained surface wind speed (10 m AGL) are provided at 6-hourly intervals, as well as information about the cyclone's classification, landfall and maximum intensity.

Table 4.1: Summary of NHC Best Track Data for Tropical Storm Bill (2015). TCMI Events are highlighted in bold.

Date/Time [UTC]	Pressure [hPa]	Wind Speed [kts]	Category
16/0000	1005	45	TS
16/0600	1001	45	TS
16/1200	997	50	TS
16/1645	997	50	TS
16/1800	997	50	TS
17/0000	998	40	TS
17/0600	999	30	TD
17/1200	**999**	**30**	**TD**
17/1800	**999**	**25**	**TD**
18/0000	1000	25	TD
18/0600	1002	20	TD
18/1200	1003	15	TD
18/1800	1004	15	Low
19/0000	1005	15	Low
19/0600	1006	15	Low
19/1200	**1006**	**15**	**Low**
19/1800	**1005**	**20**	**Low**
20/0000	**1004**	**20**	**Low**
20/0600	**1002**	**15**	**Low**
20/1200	**1001**	**15**	**Low**
20/1800	1003	15	Low
21/0000	1006	15	Low

4.2.3 North American Regional Reanalysis

Meteorological surface and pressure level variables (4.1) were obtained from the 3-hourly North American Regional Reanalysis (NARR) dataset (Mesinger et al. 2006). The NARR assimilates observations into the National Centers for Environmental Prediction (NCEP)

Eta Model to produce a 3-hourly gridded dataset with 32 km resolution and 29 vertical pressure levels distributed non-uniformly from 1000 hPa to 10 hPa on a Northern Hemisphere Lambert Conformal Conic Grid. Further, the ability of the NARR to represent land-atmosphere coupling processes (Santanello Jr et al. 2015) and its past applications toward similar studies (Kellner et al. 2012) make it an appropriate choice to properly assess the impact of land surface fluxes on inland TCs. Latent heat flux, precipitable water (PWAT) and total-column water vapor convergence (WVC) 3-hourly data were obtained for the 2-week periods preceding each TC. Because best track data are provided at 6-hourly intervals, that data can be matched with appropriate corresponding NARR time. The only exception is for the time of landfall, which often occurs between the 3-hourly NARR intervals. This discrepancy does not impact the analysis, as the focus of this study is on inland TCs.

4.3 TCMI Classification

Classification of TCMI events was designed to be consistent with previous studies. Andersen et al. (2013) established that a minimum distance of 350 km from a tropical cyclone (TC) center to the nearest oceanic moisture source is necessary to properly assess the relative influence of the land surface. This minimum distance ensures that the majority of the TC circulation, which typically occurs within a 4°to 6°radius (Frank 1977), was over land at the time of analysis. Therefore, in this study, TCMI was evaluated along the TC path only when the TC was $>$350 km from the nearest ocean basin (Fig.4.1).

Next, the TC must still display tropical characteristics at the time of inland intensification. These characteristics include temperature maxima near the core of the cyclone, vertical stacking of lows at successive height levels, and wind speed that decreases with height, consistent with the thermal wind relation (Monteverdi and Edwards 2010). Equivalent potential temperature (θ_e) was examined at 700 and 500 hPa to determine whether the core of TS Bill was warmer than the environment within a 6° radius. The companion analysis to this paper uses polarimetric radar variables to show that TS Bill continued to

Table 4.2: Summary of variables obtained from the North American Regional Reanalysis

Variable	Description	Vertical Level
Accumulated Total Precipitation [kgm^{-2}]	3-hourly accumulation	Surface
Precipitable Water for entire atmosphere [kgm^{-2}]	3-hourly mean	Total atmospheric column
Latent Heat Flux [Wm^{-2}]	3-hourly mean	Surface
Specific Humidity [$kgkg^{-1}$]	3-hourly mean	Surface and Pressure Level
Air Temperature [K]	3-hourly mean	Pressure Level
Zonal Wind [ms^{-1}]	3-hourly mean	Pressure Level
Meridional Wind [ms^{-1}]	3-hourly mean	Pressure Level
Pressure Level [hPa]	constant levels	1000, 975, 950, 925, 900, 875, 850, 825, 800, 775, 750, 725, 700, 650, 600, 550, 500, 450, 400, 350, 300, 275, 250, 225, 200, 175, 150, 125, 100.

display warm rain signatures consistent with tropical cyclone precipitation characteristics (Brauer et al. 2021) during its track over land.

A period of relatively consistent intensity occurred over much of Central Texas, during which time TS Bill produced excessive rainfall across portions of Texas, Louisiana and Oklahoma (Stewart 2016). TS Bill maintained a central pressure of 999 hPa over land

from 17 June 0600 UTC through 17 June 1800 UTC, though only the period from 1200 to 1800 UTC met the >350-km oceanic-distance constraint of Andersen and Shepherd (2013). By 1200 UTC TS Bill was far enough from the Gulf of Mexico to be considered a TCMI event (Fig. 4.2); however, maximum sustained winds decreased from 30 to 25 kt (15 to 13 ms^{-1}), despite constant minimum central pressure. Pressure level temperature and specific humidity obtained from the NARR were used to compute equivalent potential temperature (θ_e) at 500 and 700 hPa. Area-averaged θ_e was computed for all points within 0.5°of the storm center at 500 and 700 hPa at 1800 UTC 17 June (TCMI1, Fig. 4.3) and 0600 UTC 20 June (TCMI2, Fig. 4.4). The difference between equivalent potential temperature all points outside of the 0.5-degree radius (environment) was then computed and the average within the 0.5-degree radius (center) was used to identify the presence of a warm core. Generally, θ_e was maximized near the center of TS Bill, consistent with the storm retaining tropical characteristics.

Further details regarding the tropical precipitation characteristics of TS Bill over land can be found in Brauer et al. (2021). The remainder of this study will focus on the contribution of land-atmosphere interactions to overland maintenance and reintensification of TS Bill.

4.4 Two-week antecedent environment

To better understand atmospheric pre-conditioning as a reflection of soil moisture memory, surface fluxes and precipitation during the antecedent 2-week period were analyzed prior to each storm. The 2-week time window was chosen to facilitate comparison between our observed fluxes and those of TCMI events considered in past studies. The main goal was to compare how TCMI events during Bill compared with TS Erin (2007) analyzed in Andersen and Shepherd (2014).

Analysis of the 2-week antecedent period was also motivated by soil moisture memory. In other words, changes in land surface moisture are slower than changes in atmospheric moisture. Consequently, excessive precipitation is "remembered" by the land surface and reflected in higher latent heat fluxes. A continuous supply of moisture via precipitation maintains a moist land surface that can then provide a continuous flux of moisture back into the atmosphere via evapotranspiration (ET). This constant supply ensures that the rate of evaporation is constrained only by the atmospheric demand. As soil moisture depletes at slower time scales, the 2-week antecedent period provided an important understanding of how excessive precipitation during 2015 could be linked to Bill's evolution by ensuring that the supply of moisture from the land surface was maximized.

Two additional tropical cyclones which weakened rapidly after landfall were also selected for analysis to identify the primary differences between TCMI and non-TCMI environments. The selected storms met the following criteria:

1. Must be within the temporal range of the NARR dataset (1979–2019)
2. Landfall occurred along the Texas coast and storm path was through northern Texas
3. Classified as a tropical storm or tropical depression at landfall
4. Weakened rapidly following landfall and did not undergo extratropical transition.
5. 5) Overall synoptic forcing was weak.

The two storms which met these criteria and were chosen for analysis were TS Frances (1998) and TS Edouard (2008). The paths of these storms are shown in Fig. 4. While the time of year for our comparison storms is later in the warm season, an already limited sample of storms made it unfeasible to obtain comparison cases which meet the above criteria and also occur as early in the season as TS Bill.

Domain averages of surface fluxes and precipitation were computed for the 2 weeks preceding the time of interest. These domains were defined by all points within a 3°radius

centered upon a select point along a tropical cyclone's path. Domains for Erin and Bill were centered upon the locations along the HURDAT best track locations in which TCMI occurred, while domains during Edouard and Frances were centered upon points that were within a similar inland geographic region to that of Bill during TCMI1. Pressure decreases were observed from 1200 UTC 19 June to 1200 UTC 20 June for TCMI2 during TS Bill with the greatest decrease observed from 1800 UTC 19 June to 0600 UTC 20 June. Even though the location of the storm changed during this time, results showed little difference if the domain was centered at the earlier or later location. As such, the latter location was chosen as this location corresponded to approximately the same time of day as the TCMI event during Erin.

4.4.1 TCMI antecedent environments

Maximum latent heat fluxes over land for both of Bill's TCMI domains were consistently greater than maximum latent heat fluxes over the oceanic domain for the 2-week antecedent period. During the 4 days prior to Bill's formation over the ocean, maximum latent heat fluxes became more similar in magnitude to those over land and were $200-300$ Wm^{-2}. A main difference between oceanic and overland domains is that a clear diurnal cycle exists in these fluxes over the land surface that is not observed over the ocean. Consequently, the daily average latent heat fluxes over the land surface during the antecedent 2-week period for each TCMI domain were approximately 150 Wm^{-2}, which was comparable to the daily average latent heat fluxes over the ocean (approximately 125 Wm^{-2}) for the same length of time.

Both TCMI domains during Bill also displayed multiple days with precipitation during the antecedent period, allowing for maintenance of land surface moisture which then supported ample latent heat fluxes. Sensible heat fluxes over both oceanic and TCMI domains were considerably smaller than latent heat fluxes.

Pre-TCMI environments during Bill were compared to that of TS Erin, given (1) numerous studies (Arndt et al. 2009; Kellner et al. 2012; Andersen et al. 2013; Andersen and Shepherd 2014) have already shown that TS Erin's reintensification over land was likely tied to anomalous latent heat fluxes, and (2) it was expected that pre-TCMI environments during TS Erin and TS Bill would share similar characteristics. In fact, daily maximum latent heat fluxes prior to TS Bill were greater than before Erin, while sensible heat fluxes were comparatively lower than before Erin. Andersen and Shepherd (2014) showed that sensible heat fluxes prior to Erin were greater than sensible heat flux magnitudes observed for three other TCMI events which did not occur in North America. Latent and sensible heat flux magnitudes prior to TS Bill were similar to the other three pre-TCMI environments they analyzed.

4.4.2 Non-TCMI antecedent environments

Analysis of non-TCMI antecedent environments preceding TS Edouard and TS Frances showed that pre-TCMI environments differed substantially from non-TCMI environments. The magnitudes of sensible heat fluxes over the land surface prior to Edouard were nearly identical to the magnitudes of latent heat fluxes during Bill. Daily averaged latent heat fluxes during the two weeks preceding TS Edouard and TS Frances were less than 40 Wm^{-2} while daily averaged sensible heat fluxes were 132 and 90 Wm^{-2} respectively.

Rainfall in the 48 hours preceding Frances was associated with a reduction in sensible heat fluxes such that they became similar in magnitude to latent heat fluxes. This precipitation was likely associated with cloud cover from the approaching TC which reduced net radiation, and therefore reduced the magnitude of sensible and latent heat fluxes. This will be discussed further in the next two sections.

4.5 Antecedent environment water vapor budgets

Soil moisture memory can reflect antecedent precipitation anomalies which occurred several weeks to several months prior, and this memory manifests itself in the partitioning of surface fluxes (Entin et al. 2000; Basara and Crawford 2002; Wu and Dickinson 2004). However, the impact of these fluxes on atmospheric moisture content is still constrained by the typical residence time of moisture in the atmosphere. The average residence time of moisture in the atmosphere over the Great Plains can vary seasonally but is usually on the order of $3-5$ days (Läderach and Sodemann 2016). Therefore, the atmospheric moisture budget over a 3-day antecedent time window was investigated for each domain.

The primary focus was on domain averages of the 3 components of the atmospheric moisture budget—precipitation, ET and WVC—and their impacts on the total column PWAT. Domain averages were computed over the same domains used in part 4. ET was defined as a 3-hour accumulation at each 3-hour timestep and can be obtained from:

$$ET = \frac{\overline{LHF} \times \Delta t}{L_v} \tag{4.1}$$

where Δt is given in seconds, $\overline{LHF}$ is the 3-hourly latent heat flux obtained from the NARR and L_v is the latent heat of vaporization. These three variables are by no means comprehensive, but they provide an approximation of the contributions of large-scale moisture transport, evaporation and precipitation to the overall PWAT tendency during the period immediately preceding TCMI. A comprehensive analysis of every component in the atmospheric moisture is beyond the scope of the current study and the three variables chosen are intended to highlight the greatest contributors to the moisture budget.

Precipitation contributes negatively to PWAT tendency, while WVC can have positive or negative contributions and ET generally has a positive contribution except at night over land. Therefore, ET can provide a compensating source of moisture when WVC is negative and may serve as an additional source when it is positive. Figures 4.7 and 4.8 show that precipitation and water vapor flux convergence increased prior to each TCMI

event during Bill, while ET displayed a diurnal cycle. To better understand the relative positive contribution of ET to the water vapor budget, the ratio of ET to the sum of ET and WVC only was computed when WVC was positive (Figs. 4.7b and 4.8b). During daytime hours, this ratio was often >0.2. In other words, ET had about 20% of all positive contributions to the atmospheric moisture budget.

Next, the PWAT tendency obtained from summing WVC and ET and subtracting precipitation was compared to the actual PWAT tendency which was obtained by subtracting PWAT between timesteps. Then the WVC+ET−precipitation PWAT estimate was compared to the hypothetical PWAT tendency that would be obtained from the sum of WVC and precipitation only. Neglecting ET resulted in an underestimation of PWAT tendency during daytime hours, whereas including ET contributions to PWAT tendency produced a better approximation of PWAT tendency (Figs. 7b and 8b). This contrast between including versus excluding ET contributions to PWAT tendencies was particularly evident during the daytime hours on 15 and 16 June prior to TCMI1, and on 19 June prior to TCMI2. Ignoring ET during these periods underestimated PWAT tendency. Note that the summed and actual tendencies display a slight time lag, because the summed tendency shows how current values of budget terms would alter PWAT at the next time step, whereas PWAT tendency shows the change in PWAT from the period preceding the current time step.

Finally, analyses were performed to better estimate whether much of the moisture budget terms considered were driven by the tropical cyclone circulation itself, rather than the precursor environment. A moving domain of the same size as the stationary domains was computed along the path of the tropical cyclone to determine when the TCMI domain began to overlap significantly with the stationary tropical cyclone domain. Figures 4.7c–4.11c show the temporal evolution of PWAT along the path of the tropical cyclone as well as the temporal evolution of PWAT within the stationary domain. Comparing these two values enabled determination of the magnitude of the difference between PWAT within the circulation and the environment that it was moving toward. A larger difference would

support weakening of the cyclone, while smaller differences would aid in maintenance. From 15–17 June, <30% of the domain overlapped with the tropical cyclone, while both WVC and ET provided positive contributions to the atmospheric water vapor budget, and PWAT slightly increased (Fig. 4.7). Furthermore, it was shown that WVC and precipitation alone were not sufficient to estimate the actual PWAT tendency during this time; however, without considering ET, the actual tendency of PWAT was underestimated suggesting that ET played a non-negligible role in the atmospheric moisture budget prior to TCMI1.

During the daytime hours of 18 June, prior to TCMI2, PWAT increased over the domain to about the same as the along-TC domain, though the two domains did not overlap (Fig. 4.8c). WVC contributed most to PWAT tendency during this time; however, without considering ET, the actual tendency of PWAT was underestimated (Fig. 4.8b).

Similar results were observed prior to TCMI during Erin (Fig. 4.9), where ET was often at least half of the magnitude of WVC, and ignoring ET once again underestimated PWAT tendency. Conversely, during Edouard and Frances, including ET provided little impact to the estimation of PWAT tendency, while WVC and precipitation played a dominant role in the tendency of PWAT within each domain.

While both Frances (Fig. 4.10) and Edouard (Fig. 4.11) had smaller magnitudes of ET than Erin and Bill, they also had smaller magnitudes of WVC as the tropical cyclone approached each domain, despite close proximity to the Gulf of Mexico. The TCMI1 domain during Bill was also within a similar location to Frances and Edouard but was characterized by greater WVC. Even TCMI2 during Bill and TCMI during Erin, with domains much further from oceanic moisture sources, still displayed larger WVC than that observed prior to Edouard and Frances. It is hypothesized that latent heat fluxes from a moist land surface along TC inflow may have influenced the maintenance of TS Bill over land, especially during TCMI2. Such upstream influences have, in fact, been shown to occur over the ocean, where inflow parcels can gain moisture from the underlying sea surface and support tropical cyclone development (Fujiwara et al. 2017). In other words, positive WVC during TCMI

events during TS Bill and TS Erin may not be independent of influences from upstream latent heat fluxes.

4.6 Trajectory analysis

Backward trajectories were to determine the relative path of inflow parcels for each domain considered, and the nature of latent heat fluxes along these paths. The origin of air parcels within the inflow and the lower troposphere surrounding the TC was identified using the Hybrid Single-Particle Lagrangian Integrated Trajectory (HYSPLIT) model (Stein et al. 2015). HYSPLIT-generated backward trajectories were computed using 3-D temperature, moisture and wind fields from NARR. Past applications of the HYSPLIT model are extensive and include the identification of moisture sources during extreme precipitation events (Gustafsson et al. 2010; Bracken et al. 2015; Jana et al. 2018), and identification of TC parcel moisture source regions (Fritz and Wang 2013; Wang et al. 2018), including for TS Erin (Monteverdi and Edwards 2010). Therefore, the application of the HYSPLIT model to current analyses is well-justified. The objective of this analysis is to understand the potential influence of boundary layers along the path of each parcel.

Parcel backward trajectories were released from 8 horizontal planes at heights of 0, 100, 250, 500, 750, 1000, 1500, and 2000 m AGL. Each horizontal plane contained 169 release points (Figure 12) distributed within a 3°$\times$ 3°grid at 0.5°intervals, and these planes were centered upon the domains analyzed in the previous sections. Parcels were released and traced backward in time for the preceding 24-hour period. For example, one trajectory release plane was centered upon the HURDAT latitude and longitude of TS Bill's center at 0600 UTC 20 June, and trajectories from this location were traced backward from this time to 0600 19 June. In most cases, low-level TC inflow is maximized below 1000 m (Zhang et al. 2013), thus the choice of vertical levels was primarily focused on representing the inflow layer.

Parcels within the planetary boundary layer (PBL) were binned to the nearest NARR grid box to determine the relative spatial distribution of all instances along every trajectory in which a parcel was within the PBL. One major assumption of this method is that parcels within a well-mixed PBL can be influenced by surface fluxes of moisture and can represent surface influence on parcel moisture uptake or loss (Erlingis et al. 2019a,b). This assumption may be especially limited in the vicinity of a TC. However, it does provide a first guess as to where land/oceanic surface fluxes may be influential along TC inflow. Backward trajectories also provide a slightly different definition of precursor environment, with information about the origin of parcels entering the TC inflow region. Finally, the accumulated evapotranspiration was computed at every grid-box during the 24-hour periods in which backward trajectories were analyzed.

4.6.1 ET along TCMI inflow trajectories

Accumulated ET in the 24-hour period preceding TCMI1, not surprisingly, was maximized over the Gulf of Mexico with values $>$10 mm day^{-1} (Fig. 4.13a). Some of the storm's circulation was still over the Gulf of Mexico at the start of the antecedent 24-hour period, such that wind speeds at tropical storm intensity would have encouraged elevated latent heat fluxes over water. Over land, accumulated evapotranspiration was considerably smaller than over the ocean, but still considerable, especially when compared to non-TCMI cases (Figure 4.14). During Bill's TCMI1, both accumulated ET (Fig. 4.13a) and parcel frequency (Fig. 4.13b) were locally maximized to the right of the TC track and in particular along the Texas and Louisiana border where ET was approximately 5 mm day^{-1}.

Similarly, maximum ET values of 5–7 mm day^{-1} were observed along the path of inflow parcels during the 24-hour period preceding TCMI2 (Figs. 4.13c,d). The greatest number of boundary layer inflow parcels were concentrated over Alabama, central Tennessee and Kentucky where ET was also maximized during this time. More importantly, boundary layer parcels during this 24-hour period had origins that were almost exclusively

over land. As such, not only had the TC itself resided over land for over 36 hours, but most parcels within its inflow were also subjected to influence of the land surface for at least 24 hours.

During TS Erin (Fig. 4.13e,f), ET values exceeding 5 mm day^{-1} were not as widespread over land as they were during TS Bill, however ET again was maximized locally where parcel frequencies were also maximized from eastern Oklahoma through eastern Texas. Accumulated ET over land along parcel paths for both TS Bill and TS Erin was maximized between 5–7 mm day^{-1}.

4.6.2 ET along non-TCMI inflow trajectories

Accumulated ET magnitudes over land during TS Edouard (Figs. 14a,b) and during TS Frances (Figs. 14c,d) were drastically smaller than those observed during TS Bill and TS Erin. Trajectory frequency plots indicate that some inflow parcels during Edouard and Frances still had oceanic origins, though the greatest concentration of parcels in both cases was still over land. The greatest concentration of PBL parcels during TS Frances occurred in northeastern Texas where accumulated ET was minimized.

The mechanisms limiting ET during Frances were different from those during Edouard, as Frances was stationary over the domain during the antecedent 24-hour period. ET in this region is sensitive to changes in soil moisture and/or atmospheric demand (Guo et al. 2006; Koster et al. 2011; Wei et al. 2016). Even if outer rainbands moistened the land surface in the region adjacent to the storm, persistent cloud cover over the same region limited surface fluxes of heat and moisture. In this case, latent heat fluxes along trajectories were limited by available energy or atmospheric demand. Latent heat fluxes over land are subjected to a diurnal cycle and thus sensitive to the amount of incoming solar radiation. Over open water latent heat fluxes are more consistent during the day and at night and are sensitive to other factors such as wind speed. Over land, cloud cover associated with the TC reduces downward net radiation during the day and subsequently reduces ET (Tuleya 1994). Thus, when

TS Frances became stationary over land, and most inflow parcels were also concentrated over land, the storm effectively cut itself off from land-surface sources of moisture both locally and upstream via reduced net radiation. Conversely, the continued movement of TS Bill and TS Erin may have also been beneficial to sustaining intensity over land by ensuring cloud cover was not as persistent along parcel paths. Even though Edouard, like Erin and Bill, was not stationary, latent heat fluxes in the pre-storm environment and along parcel inflow were driven more by a lack of surface-based moisture. Latent heat fluxes were limited over Edouard's domain during the antecedent 2-week period, suggesting limited soil moisture that was not recharged by the minimal precipitation accumulation observed during the same period.

Finally, it was determined whether the observed differences in accumulated ET prior to TCMI versus non-TCMI storms were statistically significant through comparison of composite ET distributions. The cumulative relative frequency of parcels within defined accumulated ET bins for non-TCMI storms and TCMI storms were computed separately to create relative cumulative distribution functions based upon accumulated ET. These distributions are shown in Fig. 15. More than half of TCMI inflow parcels were within the boundary layer over regions where accumulated ET exceeded 4 mm/day, while less than 10% of non-TCMI parcels encountered the same environment. The two distributions are significantly different from each other ($p < 0.05$) per a two-sample Kolomogorov-Smirnov test following Wilks (2011). A major limitation of this analysis is that the sample size was limited by geography and by TCMI occurrence; therefore, it was that these *particular* TCMI and non-TCMI events are different. Future work could benefit from including TCMI and non-TCMI cases that are not subject to the geographic limitations outlined in the current study's data and methods.

4.7 Summary and Conclusions

Notable differences in the antecedent environment were observed for non-TCMI and TCMI storms analyzed in this study. The 2-week antecedent periods for TCMI storms were characterized by larger latent heat flux magnitudes than sensible heat flux magnitudes with daily maxima in latent heat fluxes exceeding 200 Wm–2 which is consistent with previous analyses of TCMI storms. Antecedent environments 2 weeks prior to non-TCMI storms were characterized by much greater sensible than latent heat flux magnitudes.

Analysis of the water vapor budget 3 days prior to each storm indicated that approximations of PWAT tendency prior to TCMI storms were underestimated when only WVC and precipitation were considered. Positive contributions from ET during daytime hours were of sufficient magnitude that inclusion of ET in the approximated PWAT tendency provided an estimation that was more similar to reality. The opposite was true for the water vapor budget prior to non-TCMI storms. PWAT tendency approximations were not sensitive to inclusion of ET as ET magnitudes were much smaller than those observed preceding TCMI storms. In both TCMI and non-TCMI cases WVC appeared to have the greatest positive contributions to the water vapor budget.

While WVC played a primary role in the water vapor budget, Fujiwara et al. (2017) showed that latent heat fluxes from the ocean can moisten inflow parcels along a moist conveyor belt and contribute to further strengthening of a tropical cyclone. As such, it was hypothesized that large-scale moisture transport into each storm in the current analysis may have been impacted by latent heat fluxes along parcel paths. Using 24-hour backward trajectories, it was shown that daily accumulated ET along the path of inflow parcels was greater for TCMI storms than for non-TCMI storms. This was particularly true when only parcels over land were considered as the difference in distributions of accumulated ET along inflow parcels over land for non-TCMI and TCMI storms was statistically significant ($p < 0.05$).

This study demonstrates that TCMI and non-TCMI storms displayed distinct differences in latent heat flux (or ET) within the antecedent environment and along storm inflow. Interestingly, the mechanisms by which latent heat flux is reduced along parcel inflow and in the antecedent environment seem to be less important. For example, both Edouard and Frances displayed much smaller latent heat fluxes in the 2-week antecedent environment than were observed prior to Bill and Erin. Both non-TCMI environments were dominated by sensible heat fluxes 2 weeks prior to the storm. Small flux magnitudes during the 72-hour period preceding Frances were likely driven by limited net radiation as the storm was nearly stationary over the domain from the 12th through the 13th. Conversely, minimal latent heat fluxes preceding Edouard were accompanied by large sensible heat fluxes implying sufficient net radiation and a drier land surface that limited evapotranspiration rather than limited evapotranspiration driven by cloud cover from the storm itself. Nevertheless, both storms were characterized by limited ET from the land surface and decayed rapidly following landfall.

The results presented offer a new approach for characterizing the pre-storm environment in the analysis of overland tropical cyclones. While the study followed traditional approaches of characterizing fluxes over the domain the storm would eventually occupy, it also considered whether storm inflow could be impacted by the underlying land surface. The study sample size was limited, and the primary objective was to determine whether TS Bill exhibited characteristics of TCMI during its multi-day trek over land. To accomplish this task, observations during TS Bill's TCMI events were compared to a known TCMI event in the region, TS Erin as it made landfall in a similar location and shared some early path overlap with TS Bill. A applied novel trajectory-based approach was also applied to TS Erin to determine whether the two storms shared similarities in this definition of pre-storm environment and similar comparisons were to non-TCMI storms, TS Edouard (2008) and TS Frances (1998) which made landfall in similar locations and followed similar post-landfall paths to TS Bill.

This study shows that TS Bill exhibited multiple characteristics of a TCMI storm, including its maintenance of tropical characteristics over land (Brauer et al. 2021). Furthermore, the pre-storm environment was characterized by substantial contributions to the water vapor budget from evapotranspiration and was similar to other pre-TCMI environments in the literature (Andersen et al. 2013). TCMI and non-TCMI storms displayed statistically significant differences in accumulated evapotranspiration along parcel inflow suggesting that for inland tropical cyclones, evapotranspiration along inflow parcels may also play a role in their maintenance and/or reintensification. The objective of this study is not to question the existence of the Brown Ocean Effect, but rather to determine whether TS Bill exhibited similar characteristics to other landfalling tropical cyclones which maintained intensity or underwent reintensification over land. This study presents evidence that TS Bill's pre-storm environment supported its maintenance over land and provides a new approach for characterizing and defining the pre-storm environment via inflow parcel trajectories. Using this new approach, a statistically significant ($p < 0.05$) difference in ET along parcel inflow trajectories was demonstrated for TCMI versus non-TCMI storms. The geographic restrictions of the study limited sample size and future observational and reanalysis-based work should include analysis of potential TCMI and non-TCMI storms which made landfall at points beyond the Texas and Louisiana Gulf coasts. Zhang et al. (2018) showed that excessive precipitation during Hurricane Harvey may have been related not to latent heat fluxes, but rather, to enhanced surface roughness over the urban region. The methods employed in this study attempted to account for differences in land surface characteristics by selecting storms with similar paths, such that they would be subjected to similar surface roughness, and soil texture. Even so, these variables can still vary over small distances. Other land surface characteristics not analyzed in this study, like vegetation and albedo, can vary from year to year. As such, future work should include model simulations of TS Bill to determine the storm's sensitivity to not only latent heat fluxes, but

to surface roughness, albedo, soil texture, and other land surface characteristics, however that is beyond the scope of the current analysis.

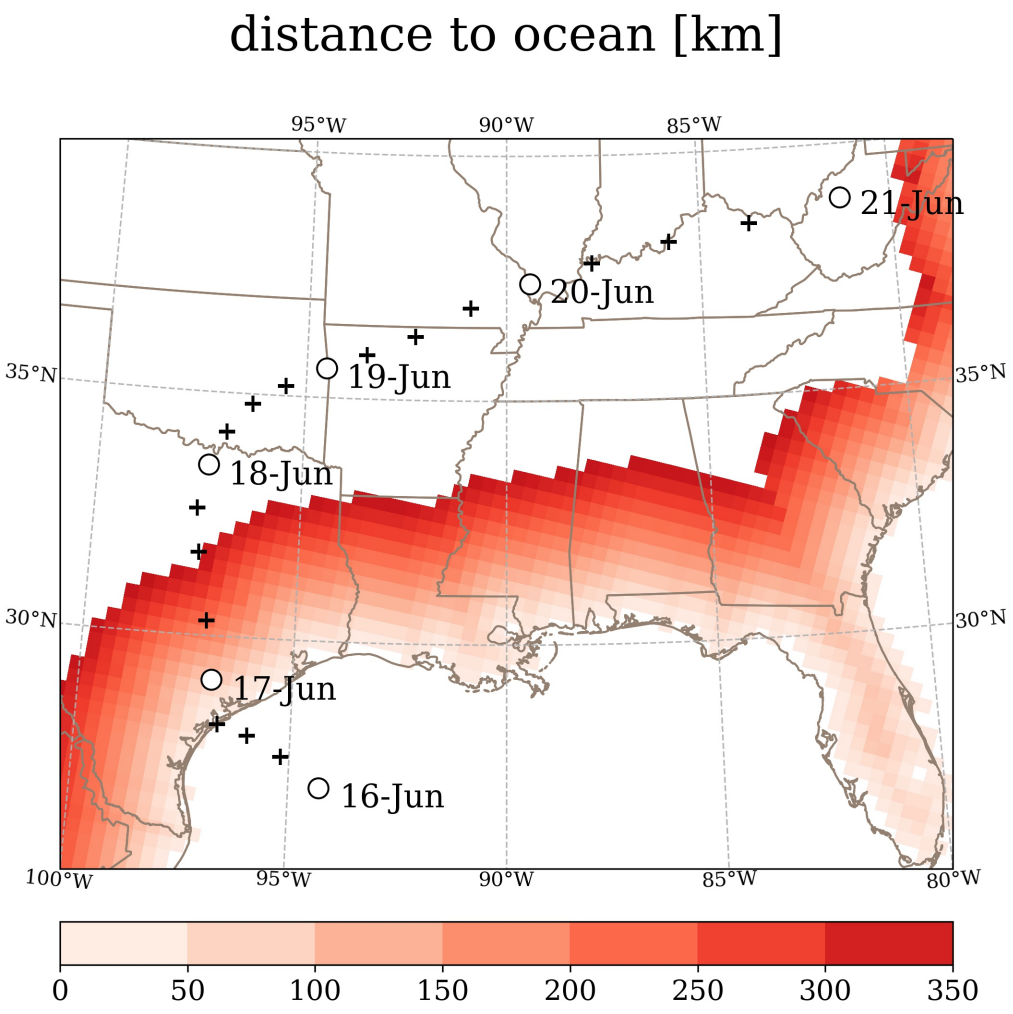

Figure 4.1: Distance from nearest ocean basin (shaded up to 350 km) and Tropical Storm Bill (2015) track. White filled circles represent 0000 UTC location while plus signs represent location at 0600, 1200 and 1800 UTC.

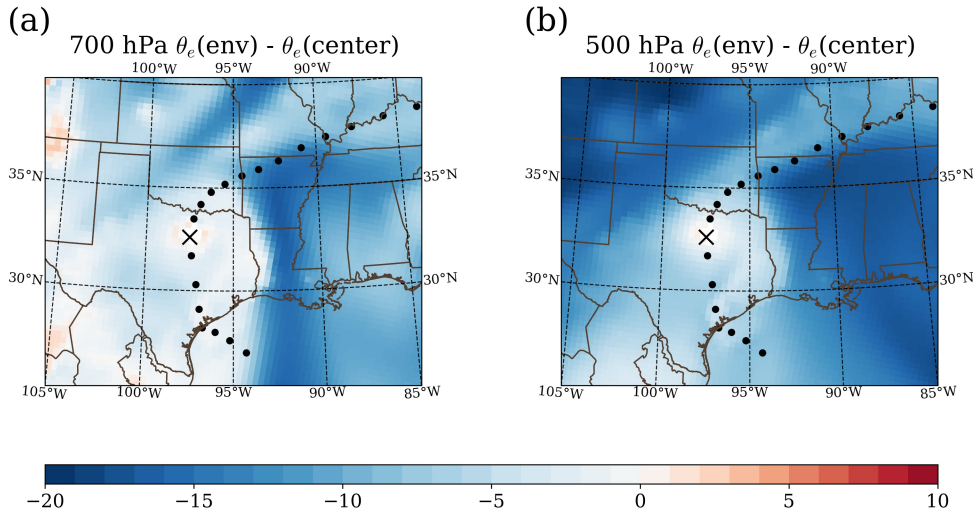

Figure 4.2: Difference from 0.5-degree area-averaged equivalent potential at 1800 UTC on 17 June 2015 at (a) 700 hPa and (b) 500 hPa. Area-averaged equivalent potential temperature was obtained by averaging equivalent potential temperature within a 0.5°radius of the storm center on 1800 UTC 17 June, while the environment is defined as all points outside of this region. Blue means that the environment is cooler than the 0.5-degree average.

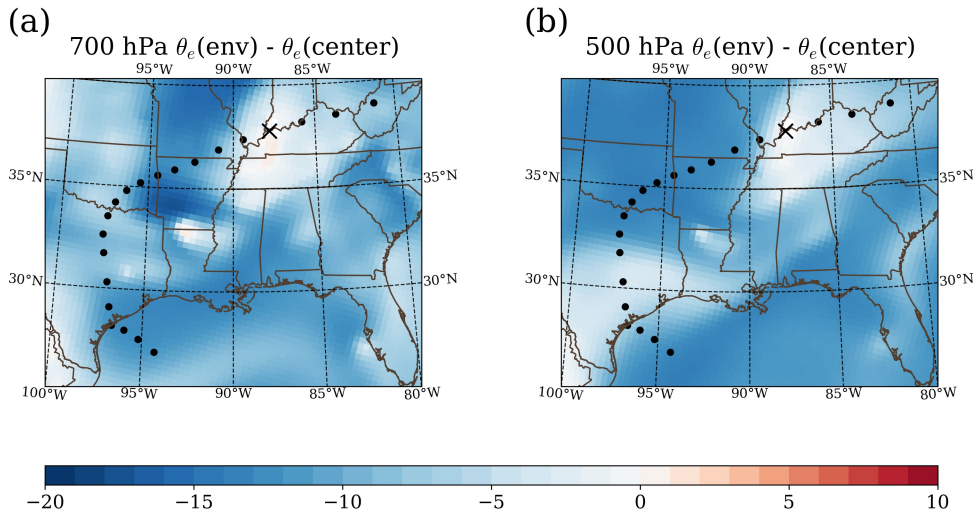

Figure 4.3: As in Fig. 4.2 but at 0600 UTC on 20 June 2015

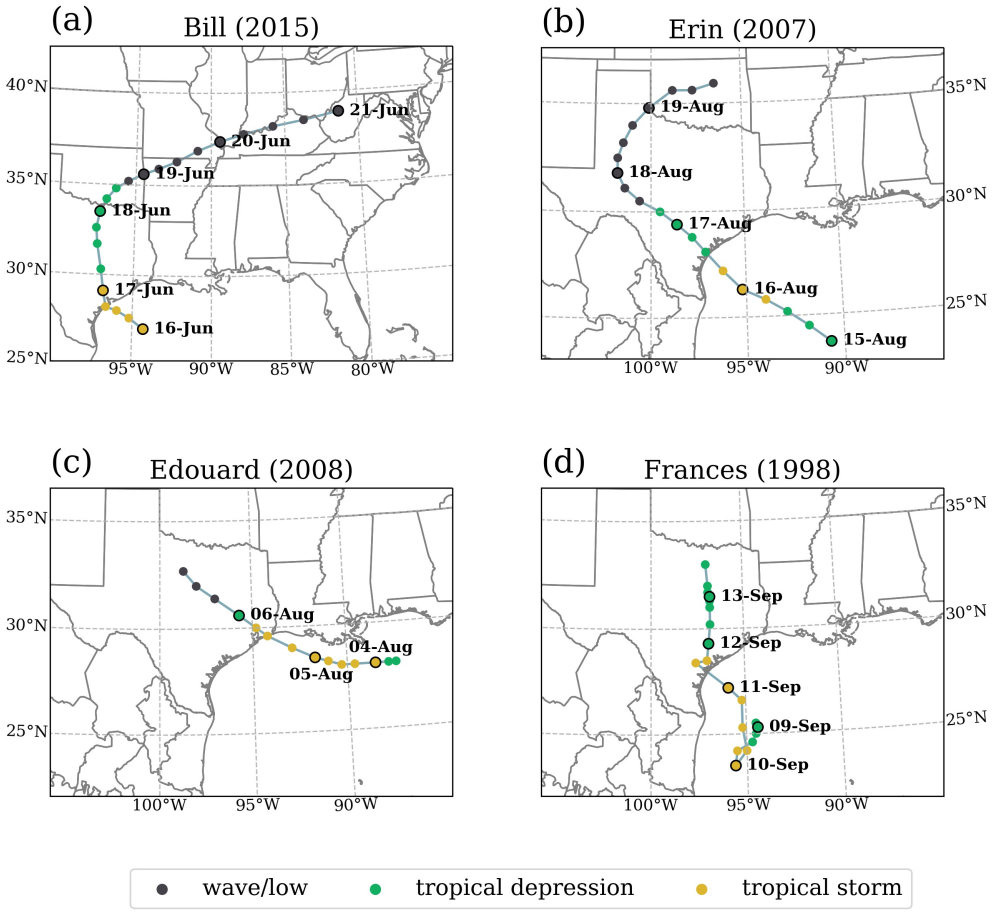

Figure 4.4: NHC Best Track estimates for (a) Tropical Storm Bil (2015), (b) Tropical Storm Erin (2007), (c) Tropical Storm Edouard (2008) and (d) Tropical Storm Frances (1998). 0000 UTC location is given for each date, while colors correspond to intensity.

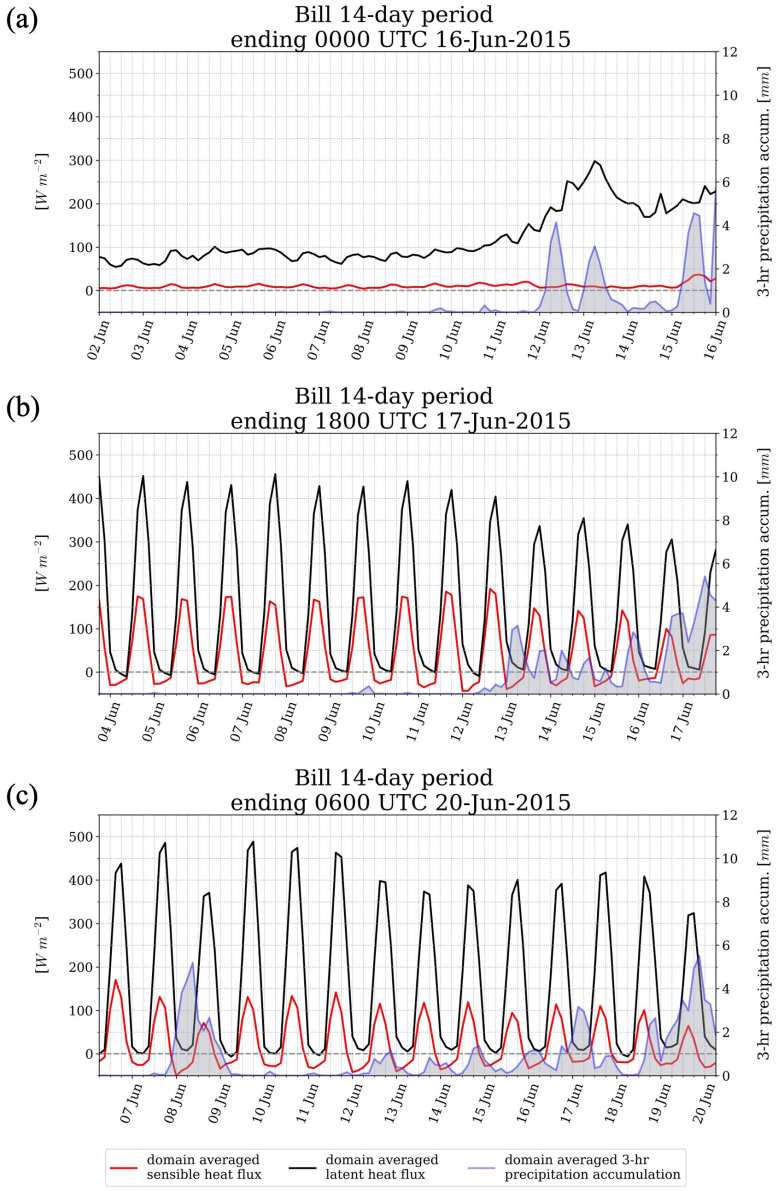

Figure 4.5: Domain averaged 3-hourly latent and sensible heat fluxes and 3-hourly accumulated precipitation for the two-week period preceding (a) formation of Tropical Storm Bill (b) TCMI1 during Tropical Storm Bill and (c) TCMI2 during Tropical Storm Bill.

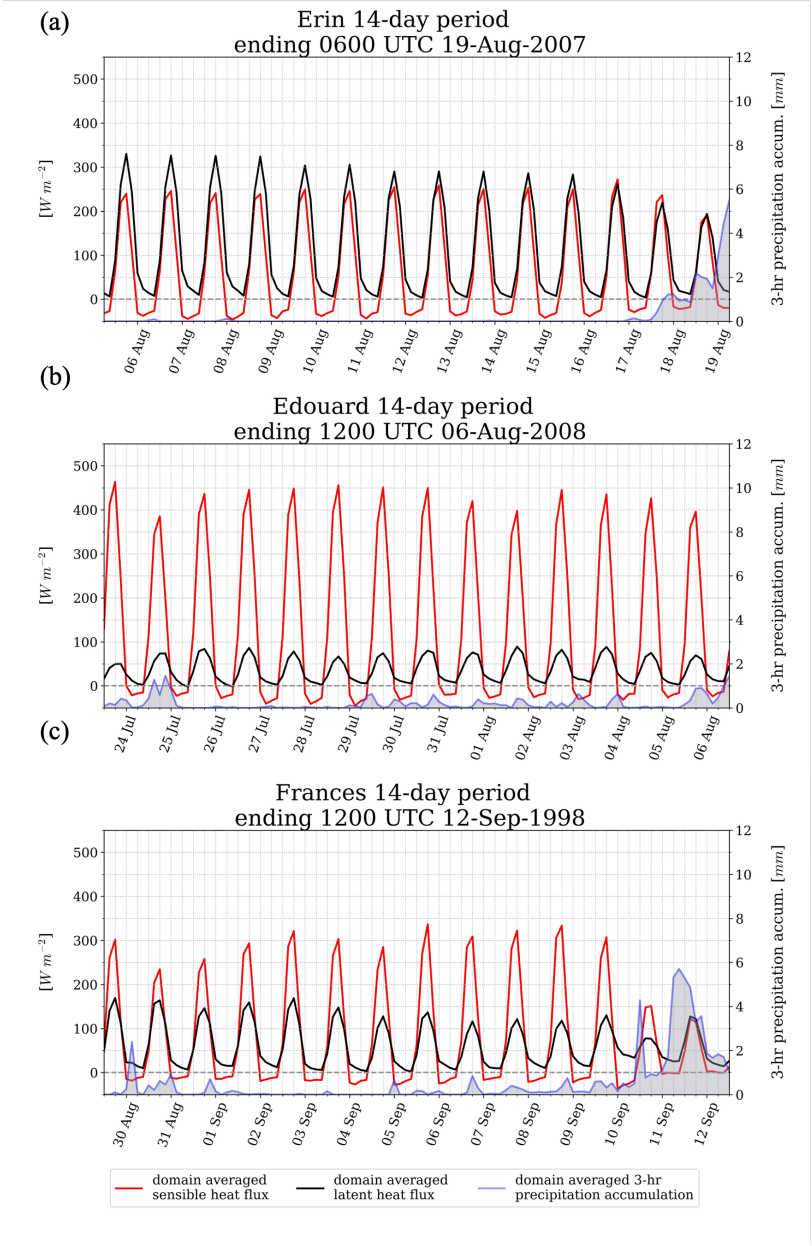

Figure 4.6: As in Figure 4.5 but for (a) TCMI during Tropical Storm Erin (b) non-TCMI during Edouard (c) non-TCMI during Frances.

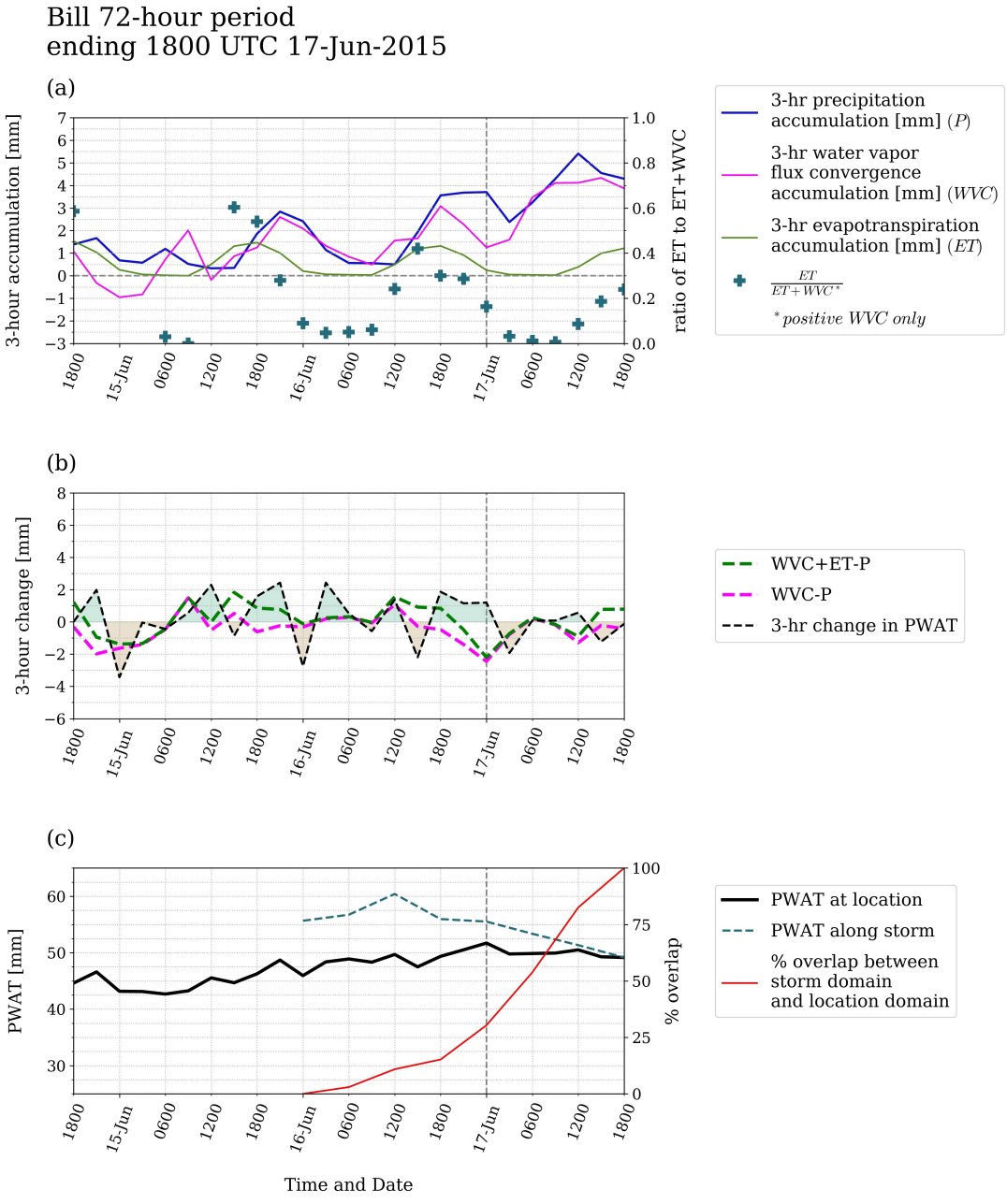
Bill 72-hour period
ending 1800 UTC 17-Jun-2015
(a)
3-hour accumulation [mm]
ratio of ET to ET+WVC
3-hr precipitation accumulation [mm] (P)
3-hr water vapor flux convergence accumulation [mm] (WVC)
3-hr evapotranspiration accumulation [mm] (ET)
ET / ET+WVC*
*positive WVC only
(b)
3-hour change [mm]
WVC+ET-P
WVC-P
3-hr change in PWAT
(c)
PWAT [mm]
% overlap
PWAT at location
PWAT along storm
% overlap between storm domain and location domain
1800
15-Jun
0600
1200
1800
16-Jun
0600
1200
1800
17-Jun
0600
1200
1800
Time and Date

Figure 4.7: Water vapor budget during the 72-hour period preceding TCMI1 with (a) Domain averaged, 3-hourly accumulated precipitation (mm; blue line), total column water vapor flux convergence (WVC; mm; magenta line), evapotranspiration (ET; mm; green line), and ratio of ET to sum of ET and WVC (dimensionless; crosses). Ratio was only computed when WVC is positive. (b) Estimated precipitable water (PWAT) tendency (mm per 3 hours) from summing WVC, ET and precipitation (dashed green line), estimated PWAT tendency from summing WVC and precipitation only (dashed magenta line), and actual PWAT tendency (black dashed line). Teal and brown shading denote positive and negative PWAT tendency. Respectively. (c) Temporal variation in PWAT (mm) within domain of interest (solid black line), temporal variation along path of TS Bill (dashed teal line), and percent overlap between domain centered along storm's path and the current domain (solid red line).

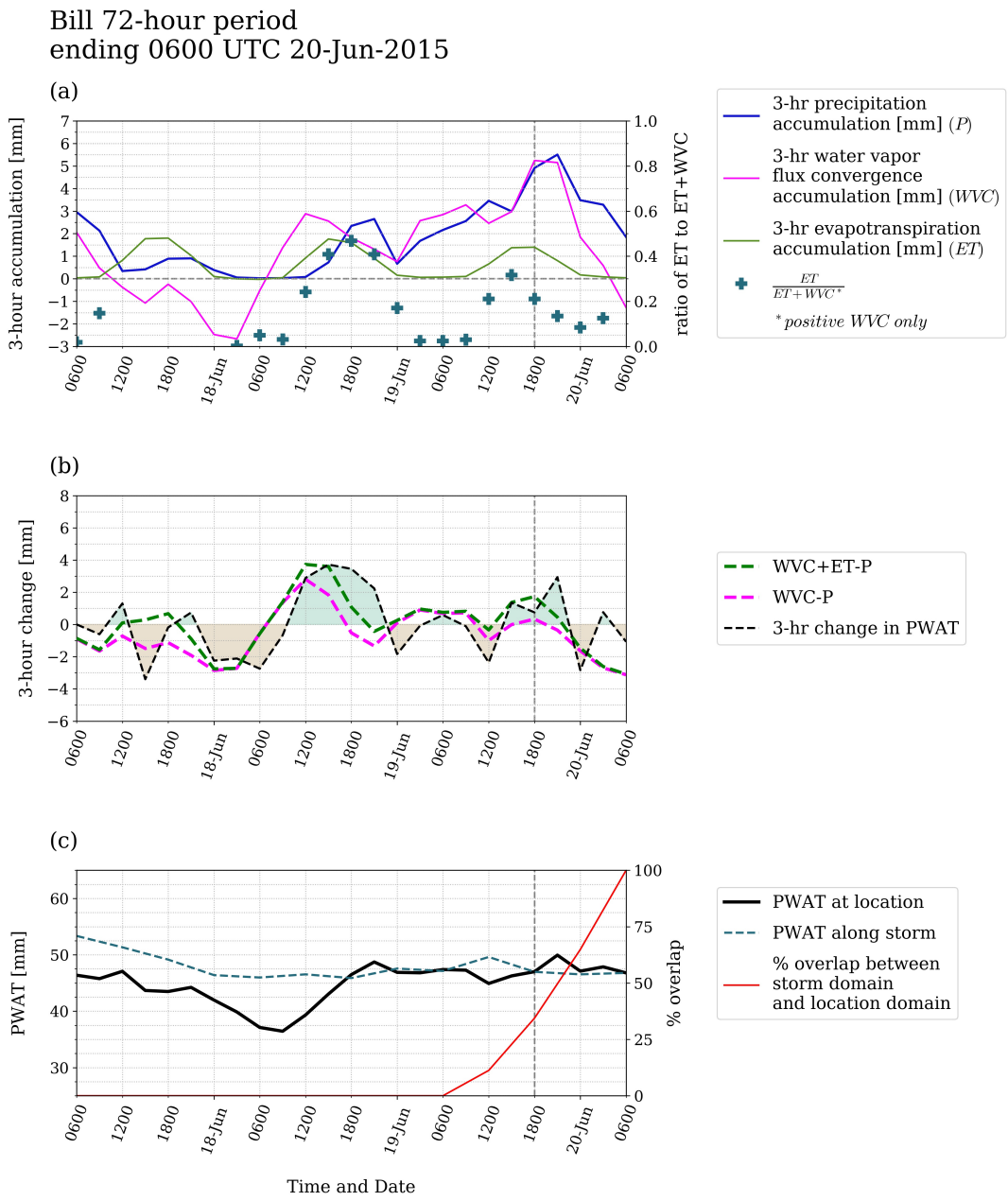

Figure 4.8: As in Figure 4.7 but for the 72-hour period preceding TCMI2.

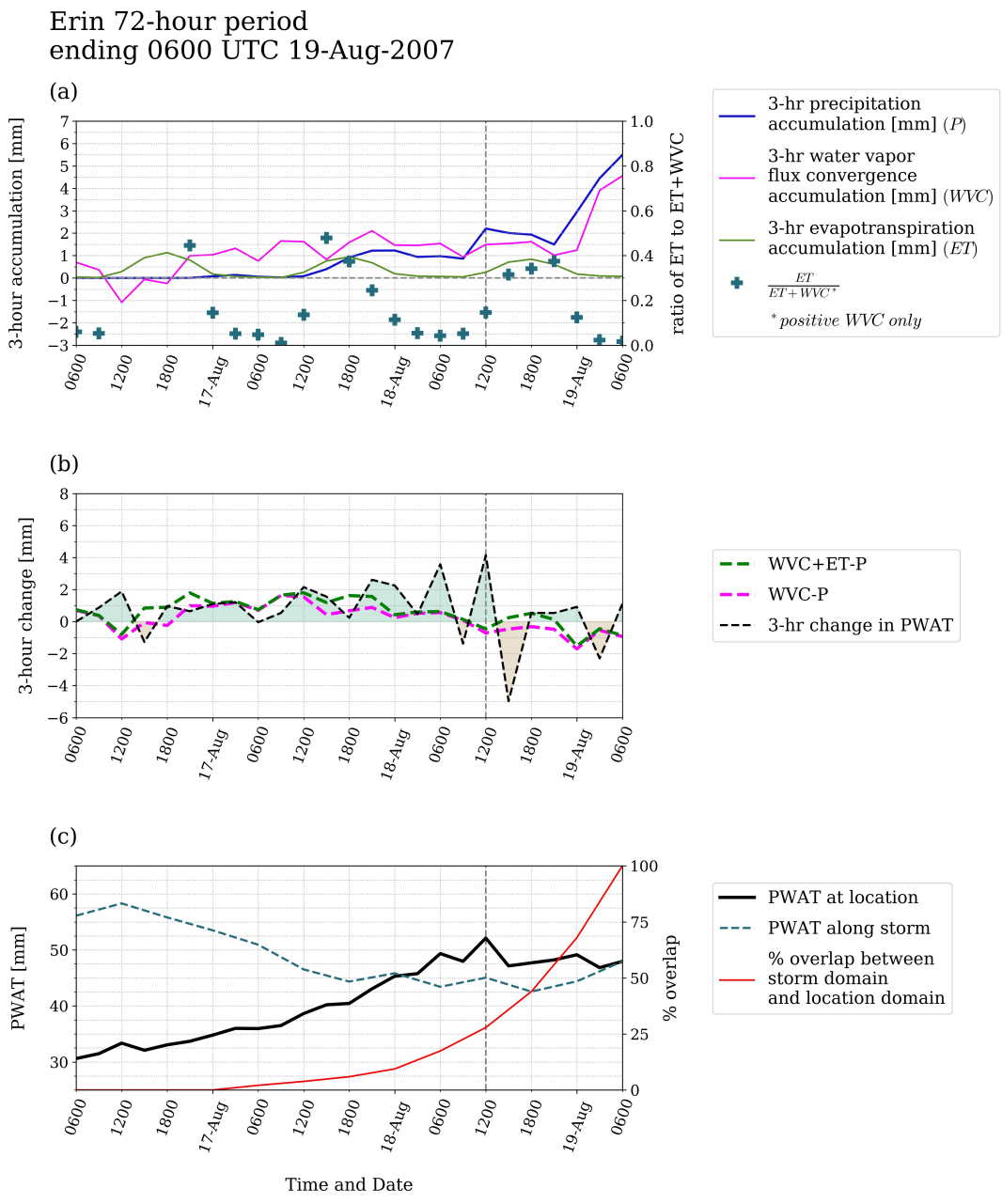

Figure 4.9: As in Figure 4.7 but for the 72-hour period preceding TCMI during Erin.

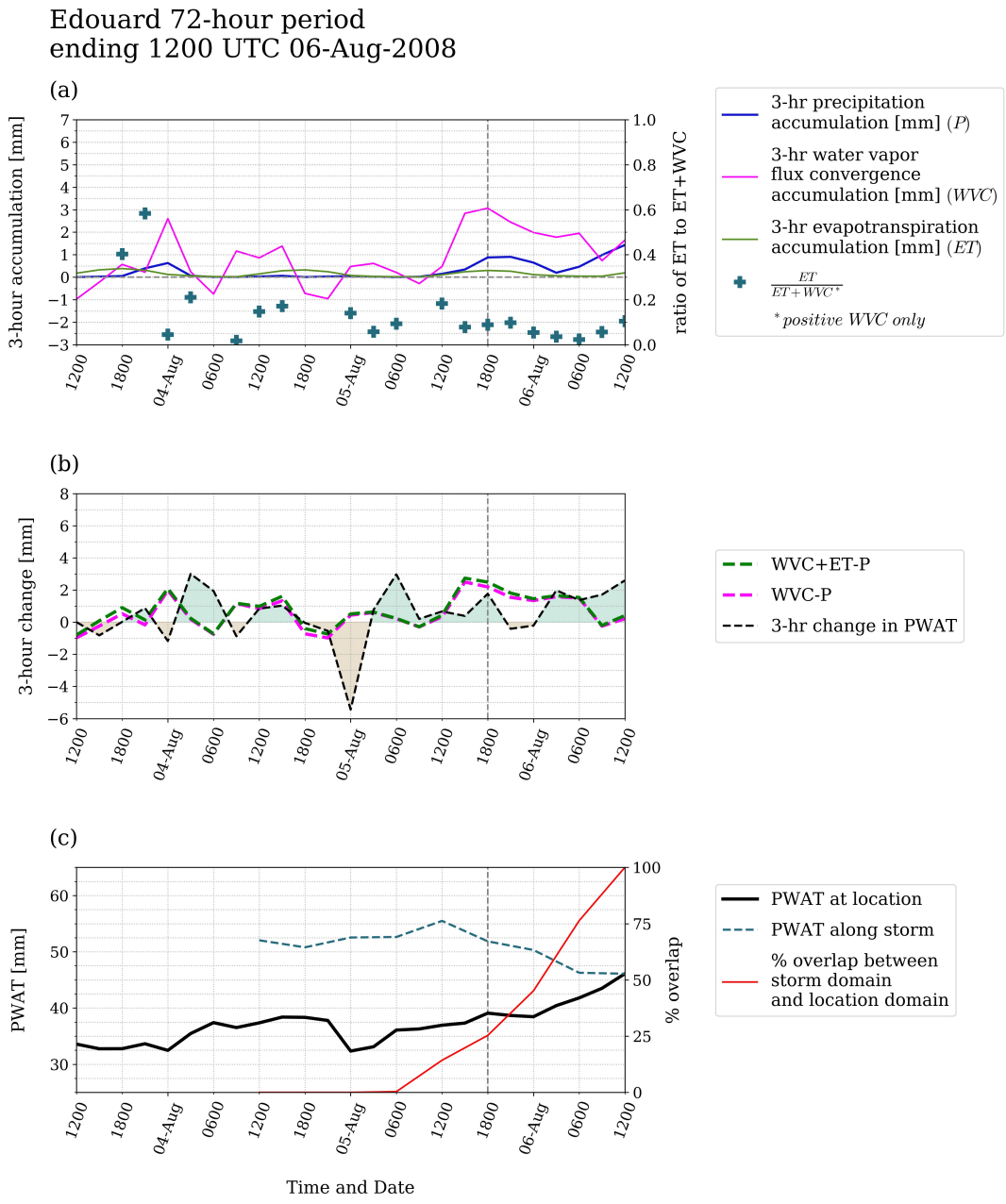

Figure 4.10: As in Figure 4.7 but for the 72-hour period preceding 1200 UTC on 06 August 2008 during Tropical Storm Edouard.

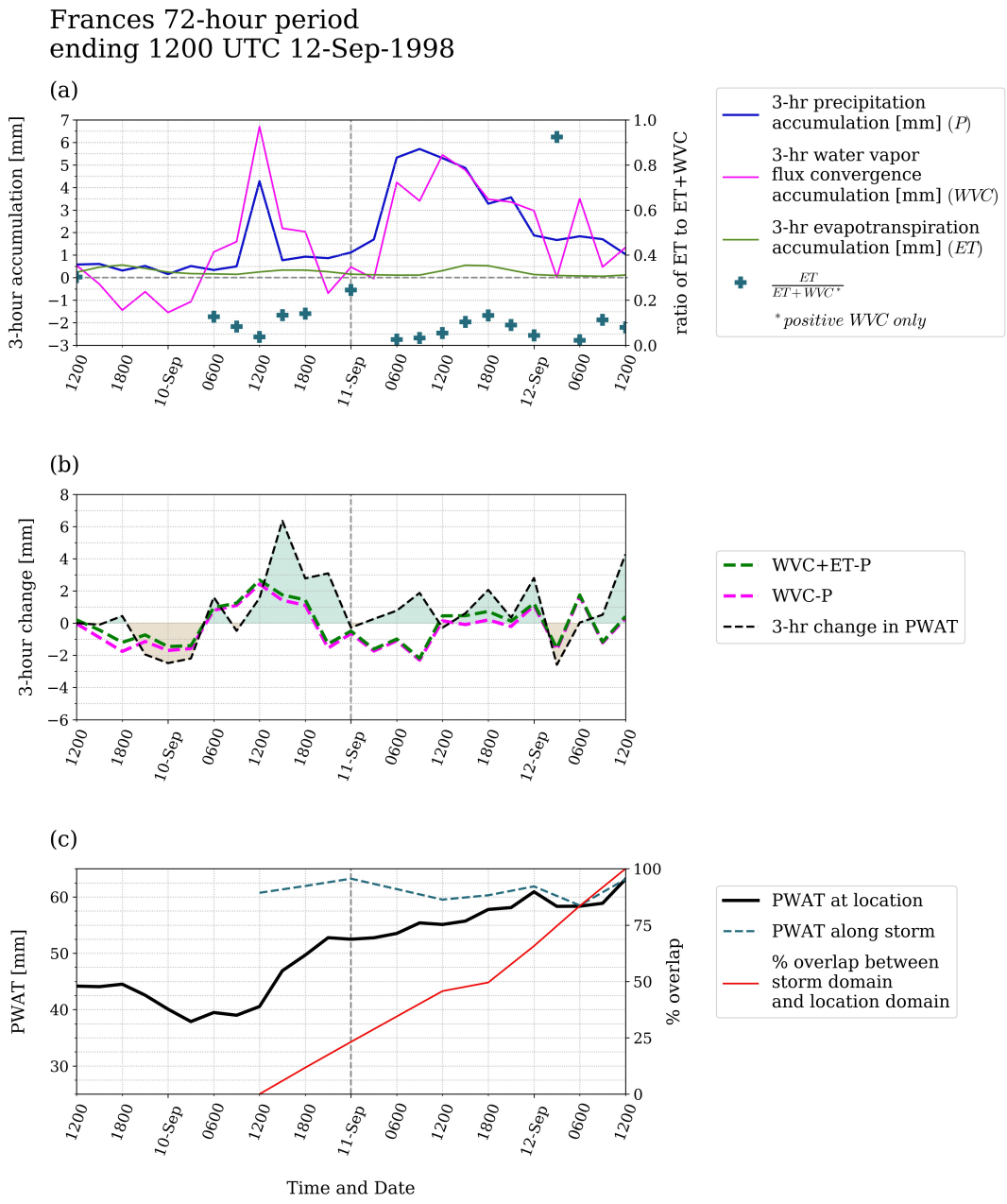

Figure 4.11: As in Figure 4.7 but for the 72-hour period preceding 1200 UTC on 13 September 1998 during Tropical Storm Frances.

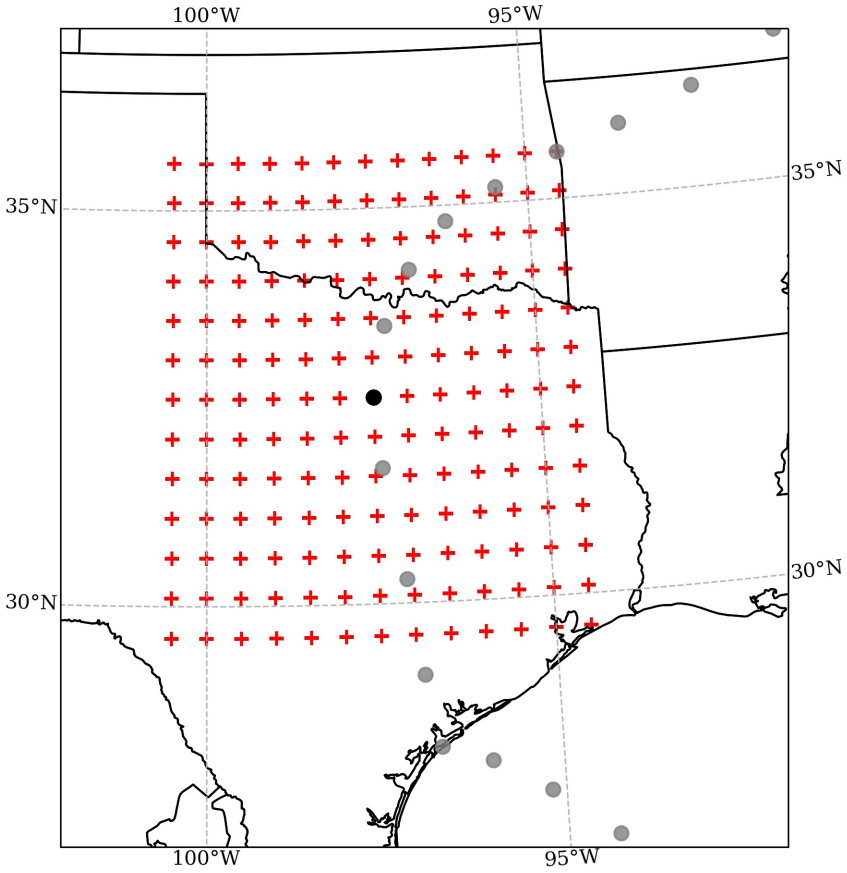

Figure 4.12: Example horizontal trajectory release grid for 1800 UTC 17 June 2015 for a single level. Red crosses represent trajectory release points and the black marker represents the location of TS Bill at the time of interest while gray markers represent the path of TS Bill.

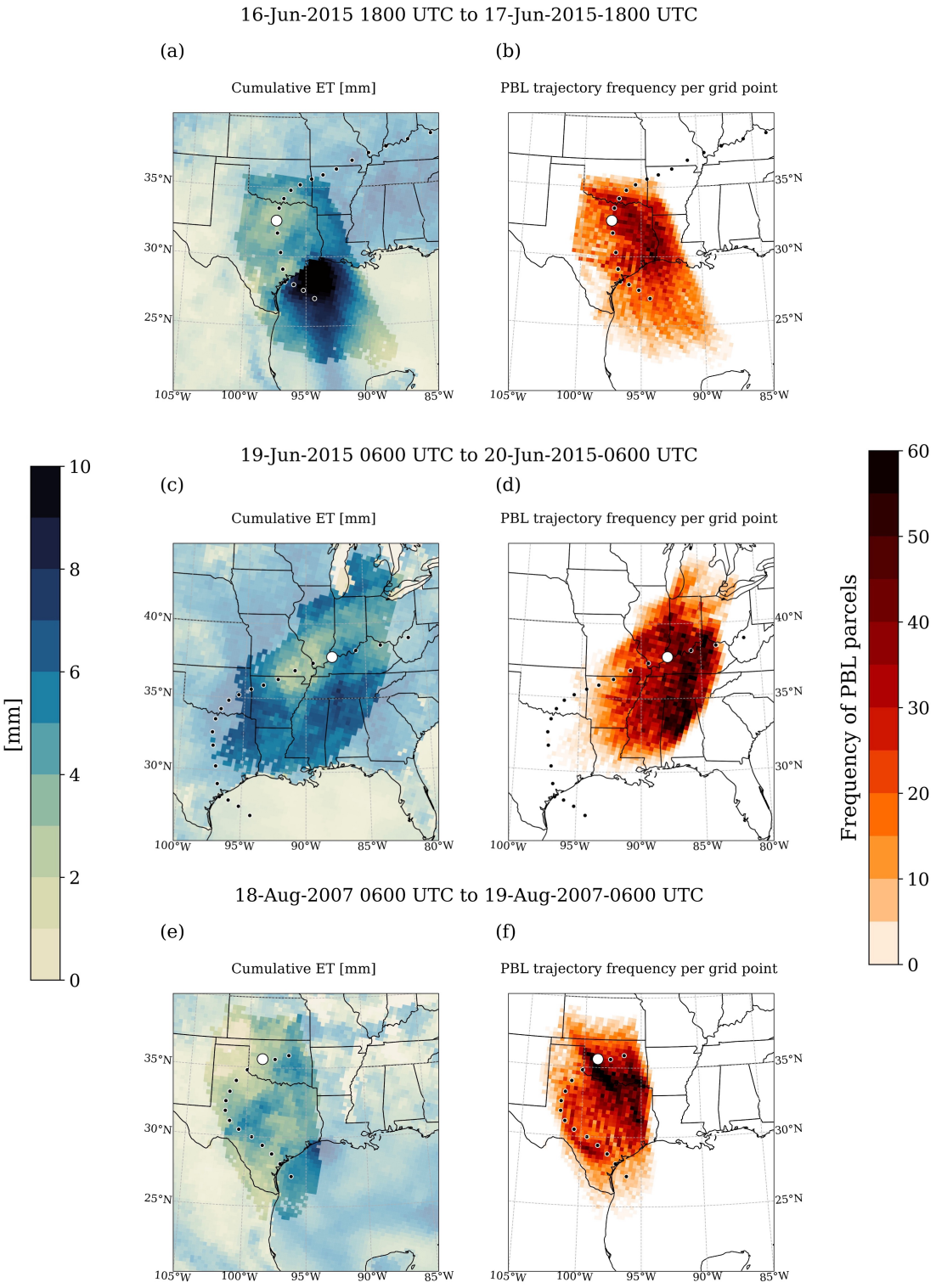
16-Jun-2015 1800 UTC to 17-Jun-2015-1800 UTC
(a)
Cumulative ET [mm]
(b)
PBL trajectory frequency per grid point
19-Jun-2015 0600 UTC to 20-Jun-2015-0600 UTC
(c)
Cumulative ET [mm]
(d)
PBL trajectory frequency per grid point
18-Aug-2007 0600 UTC to 19-Aug-2007-0600 UTC
(e)
Cumulative ET [mm]
(f)
PBL trajectory frequency per grid point
[mm]
0
2
4
6
8
10
Frequency of PBL parcels
0
10
20
30
40
50
60
105°W
100°W
95°W
90°W
85°W
80°W
25°N
30°N
35°N
40°N

Figure 4.13: 24-hour accumulated ET (a,c,e) and frequency of parcels along inflow trajectories that were within the boundary layer (b,d,f) for the 24-hour period preceding (a,b) TCMI1 during Tropical Storm Bill (c,d) TCMI2 during Tropical Storm Bill and (e,f) TCMI during Tropical Storm Erin.

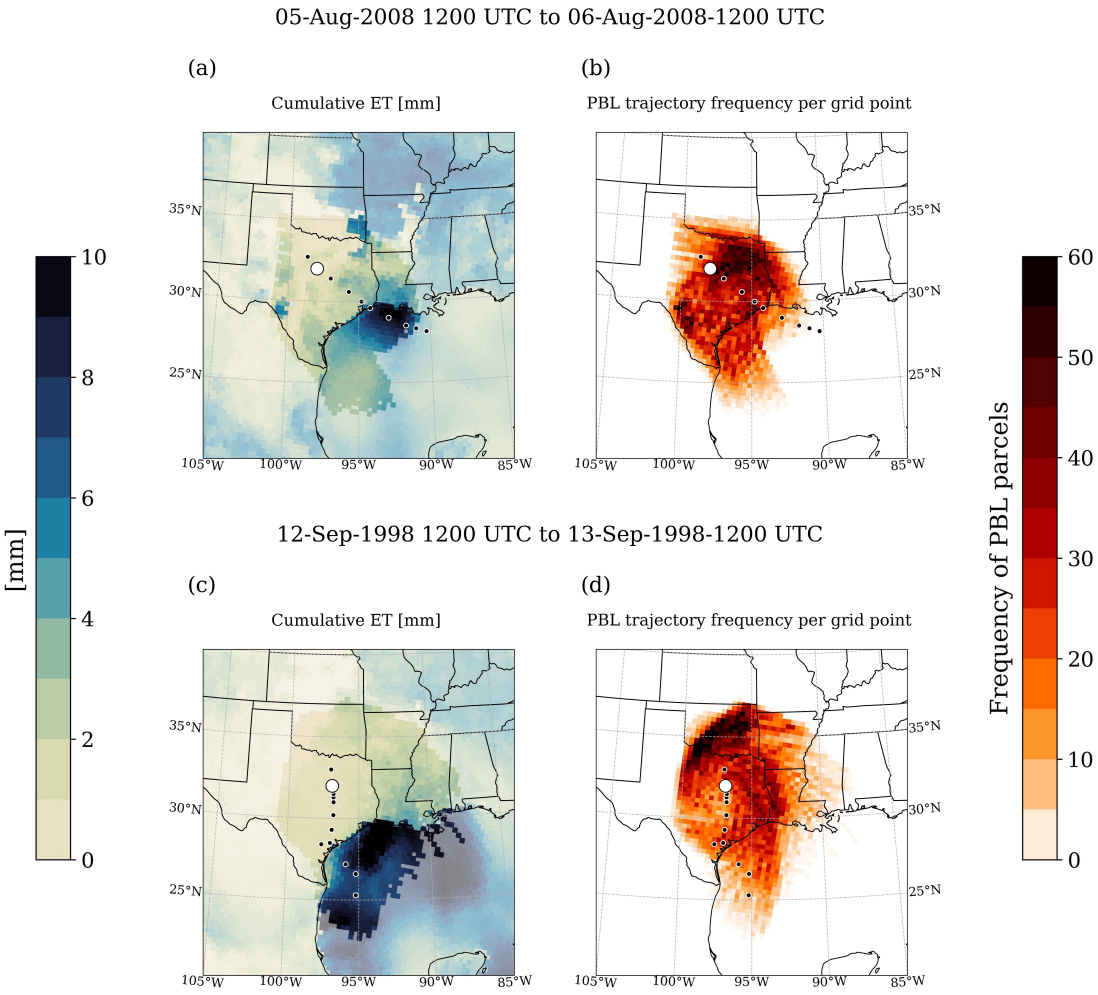

Figure 4.14: As in Figure 12 but for (a,b) 24-hour period preceding 1200 UTC 06 August 2008 during Edouard and (c,d) 24-hour period preceding 1200 UTC 13 September 1998 during Frances.

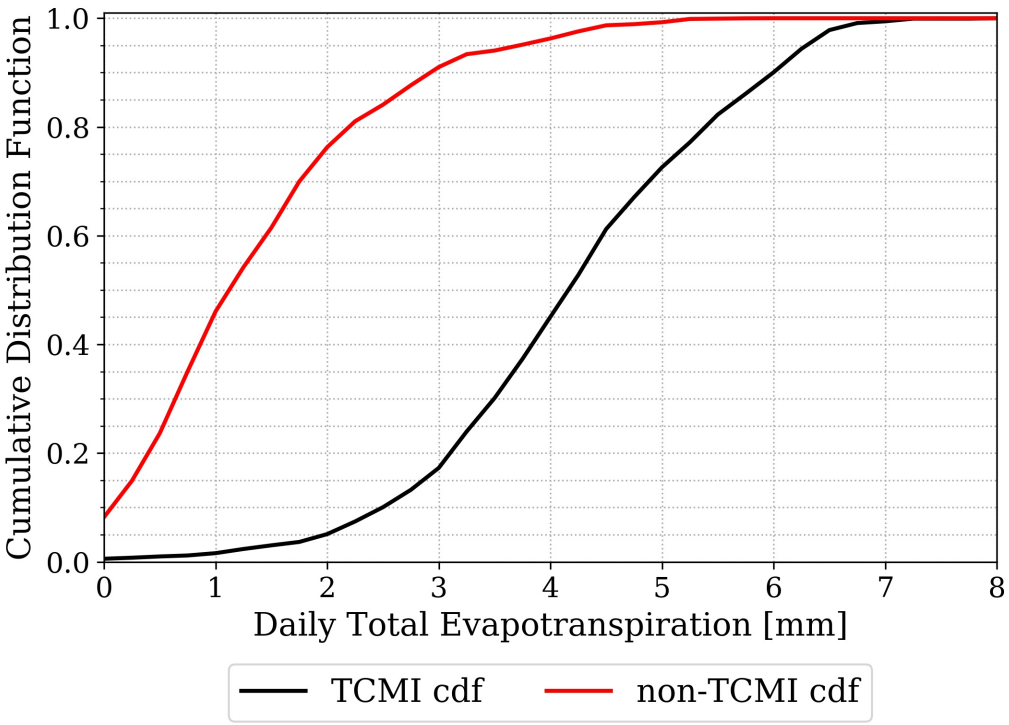

Figure 4.15: Cumulative distribution function for all boundary layer parcels binned by 24-hour accumulated ET [mm] for TCMI and non-TCMI storms.

Chapter 5

Sensitivity of daytime planetary boundary layer evolution to soil moisture conditions during the 2012 flash drought

5.1 Introduction

Seasonal forecasts failed to predict the 2012 drought in the central United States and though retrospective climate simulations indicated that internal climate variability may have played a role in its development (Hoerling et al. 2014), land-atmosphere feedbacks may have aided in the propagation and intensity of the event (Basara et al. 2019). For example, severity and extent of the 2012 drought was reduced in regional climate model simulations when late spring/early summer soil moisture was greater (Saini et al. 2016). More recently, DeAngelis et al. (2020) showed that improved initialization of soil moisture in global forecast models improved predictability of the 2012 drought once dry soils were established, demonstrating some sensitivity of drought evolution to the land surface state.

Drought in the Great Plains is often associated with a persistent mid to upper-level anticyclone, which suppresses precipitation and cloud development through large scale subsidence (Namias 1983; Trenberth et al. 1988; Schubert et al. 2004a; Dong et al. 2011; Basara et al. 2013). The origin of these atmospheric circulation patterns is frequently attributed to forcing from remote sea surface temperature (SST) anomalies (Trenberth and Guillemot 1996; Seager et al. 2005; Schubert et al. 2008, 2009; Seager and Hoerling 2014; Seager et al. 2019). Even so, once drought has been established, land-atmosphere feedbacks can reinforce drought conditions (Hong and Kalnay 2000).

Evolution of the daytime PBL is modulated by local turbulent fluxes (Basara and Crawford 2002) as well as the stability and moisture content of the layer immediately overlying the PBL (Ek and Mahrt 1994; Ek and Holtslag 2004). In addition to turbulent fluxes,

advection can play a similarly important role (Stull 1988). Similarly, when land surface heterogeneities are present, air masses may be modified along their trajectories by the underlying land surface (Stull 1988; Erlingis and Barros 2014; Erlingis et al. 2019a,b; Herrera-Estrada et al. 2019; Molina and Allen 2019, 2020). For example, Schumacher et al. (2019) showed that drought-enhanced sensible heat fluxes were advected into central Russia and contributed to heat wave development over Moscow in 2010. Miralles et al. (2019) showed a connection between heatwaves and upwind sensible heat fluxes, while Herrera-Estrada et al. (2019) similarly suggested that drought propagation into one region may be tied to decreases in upstream evapotranspiration over a region already in drought. While land-atmosphere interactions are constrained to the background atmospheric state, even during extreme events, (Su and Dickinson 2017), it is hypothesized that land-atmosphere feedbacks played an important role in the evolution of the 2012 flash drought (Basara et al. 2019). Saini et al. (2016) showed that severity and extent of the 2012 drought was reduced in regional climate model simulations when late spring/early summer soil moisture was greater.

This research seeks to build upon this hypothesis by investigating land-atmosphere feedbacks both locally and upstream during the 2012 flash drought. These Lagrangian land-atmosphere feedbacks are proposed as a critical mechanism for fueling flash drought development in the current research. Therefore, it is important to consider relative contributions of advection as well as surface fluxes and entrainment process to the daytime evolution of the PBL during flash drought and as flash drought evolves into long-term, persistent drought. Additionally, the origins of airmasses contributing to moisture and temperature advection within the PBL must also be considered. The primary question is how land-atmosphere feedbacks contribute to flash drought evolution and whether they amplify and perpetuate long-term drought following flash drought.

The primary hypotheses include:

1. 1) Local-land atmosphere feedbacks over a region that was already experiencing intense drought contributed to the development of a deeper, warmer and drier PBL over dry soils, increasing the overall evaporative demand or potential evapotranspiration (PET) within the PBL. This is considered the "drought influenced" PBL.

2. he drought influenced PBL was subsequently transported downstream over a region in which soils were not as dry and vegetation was still relatively healthy. The higher PET would enhance the rate of evapotranspiration (ET), increasing the rate of soil drying in the region where drought was not existent or less intense.

3. 3) Initially, the greater rate of ET would modulate the high PET air mass such that further downstream, drying was not as pronounced, until the second location also cascaded into drought.

4. 4) Similarly, if saturated soils are introduced throughout the domain, it is expected that PET would decrease locally and upstream due to soil moisture no longer limiting ET, allowing surface fluxes to moisten the PBL.

5.1.1 Event background

Drought was absent across much of the study domain at the beginning of the period with the exception of western Texas, western Kansas and the Oklahoma panhandle (Fig. 1a). Drought quickly intensified during the next 11 weeks resulting in most of the domain being classified by the United States Drought Monitor (USDM; Svoboda et al. 2002) as experiencing extreme drought (Fig 5.1b). Two phases of drying were observed across the domain (Fig. 5.2) during the 2012 flash drought. The first occurred during the beginning of the warm season from early to late May. A brief reprieve was observed from late May into the first week of June before rapid drying continued throughout June and July, eventually leading into long term drought (Fig. 5.2). The term flash drought describes the period of rapid drying when atmospheric demand largely exceeds evapotranspiration. This tends

to precede the impacts of the flash drought which become apparent when soils become desiccated and vegetation begins to wilt. Flash drought may end with a perpetuation of precipitation deficits and hostile atmospheric conditions that result in long term drought or it may end in ecosystem recovery due to atmospheric pattern changes that bring significant precipitation including features such as atmospheric rivers or tropical cyclones (Wu and Dirmeyer 2020). In 2012, flash drought during May-July led to prolonged drought over much of the central US including the southern Great Plains.

The first phase of the event was characterized by a steady decrease in soil moisture during May that resulted in nearly 90% of the domain being classified as abnormally dry or worse by the the USDM at the beginning of June. The end of this first phase was marked by temporary recharge of soil moisture in early June (Fig. 5.3) before rapid intensification of drought resumed. The rapid drying associated with flash drought ended in late June as long-term drought became established. Impacts of the flash drought were reflected in a 3-category increase during the first 3 weeks of July from moderate to extreme drought in northern Oklahoma.

5.2 Experimental design

5.2.1 Case selection

While flash drought was observed at many locations in the southern Great Plains region during 2012, the primary focus of this study is on the evolution of flash drought near the Atmospheric Radiation Measurement Program's Southern Great Plains (ARM SGP) site in Lamont, Oklahoma, where radiosonde observations are available at 6-hourly intervals for comparison to simulation output. Simulated case studies were selected to represent the various phases of the 2012 flash drought and subsequent long-term drought to better understand the role that land-atmosphere coupling may have played in the evolution of this event. Each case was selected when synoptically quiescent conditions were present for the duration of the simulation period. This was critical for attempting to disentangle the

relative contribution of the land surface toward boundary layer temperature and moisture evolution while avoiding atmospheric properties related to frontal boundaries and other synoptic features that could overpower any influence from the land surface. The selected cases are presented in Table 1.

5.2.2 NU-WRF and LIS

Case study simulations were utilized to test the sensitivity of the PBL to changes in soil moisture during the 2012 flash drought using the NASA Unified Weather Research and Forecasting (NU-WRF; Peters-Lidard et al. 2015) model coupled to NASA Land Information Systems (LIS; Kumar et al. 2006; Peters-Lidard et al. 2007). NU-WRF is NASA's version of the WRF-ARW model that provides additional model physics options unique to NASA, including ability to couple the land surface to the atmosphere through the implementation of LIS. LIS is a land surface modeling and data assimilation software framework that was developed to integrate both satellite and surface observations to obtain better approximations of land surface states, such as surface fluxes, soil moisture, etc. NU-WRF and LIS coupled simulations have been used in numerous applications to better understand the sensitivity of the atmosphere to land surface characteristics including soil moisture, irrigation, and vegetation (Santanello Jr et al. 2011). Thus, the coupled NU-WRF and LIS system (LIS-WRF) also provides an optimal choice for examining the sensitivity of PBL evolution to soil moisture during flash drought and drought.

All cases were simulated over the same 1100 km x 900 km domain (Fig. 5.4a) centered upon the ARM SGP site with a 1 km spatial resolution. The choice of one domain for all cases eliminated uncertainties associated with differences in initial and lateral boundary conditions that may arise from shifting the domain between simulations. Model physics combinations were based upon those used in Santanello Jr et al. (2019) and were chosen for their ability to best isolate the impacts of land-atmosphere coupling on simulation behavior.

Global Forecast System (GFS; Center 2003) 6-hourly analysis data were used as the atmospheric lateral boundary conditions (BC). Land surface initial conditions (ICs) were obtained through offline (uncoupled) simulations using LIS. Version 3.3 of the NOAH LSM (Ek et al. 2003) was used with meteorological forcing from the North American Land Data Assimilation System version 2 (NLDAS-2) dataset. The offline spinup was performed over a 5-year period from June 2007 to June 2012. From June 2007 to June 2010, the National Centers for Environmental Prediction (NCEP) monthly climatological greenness vegetation dataset was used for greenness vegetation fraction (GVF; Gutman and Ignatov 1998). Greenness vegetation fraction represents the density of green vegetation within a model grid cell and is related to vegetation type and phenology (Ek et al. 2003). As such, the distribution of vegetation in a grid cell influences how the LSM represents surface fluxes of moisture. NASA's short-term prediction research and transition (SPORT) center began producing a real-time GVF dataset based on NDVI observations from the Moderate Resolution Imaging Spectrometer (MODIS) during the summer of 2010, and SPoRT-MODIS real-time GVF was used instead for the remainder of the offline LIS spinup. The SPoRT-MODIS real-time GVF dataset allows for real-time observations of photosynthetically active vegetation and is, therefore, a more optimal choice for capturing vegetation health during flash drought, allowing evapotranspiration to be better represented by the LSM. Land surface ICs from the offline spinups were then used to initialize the coupled LIS and NU-WRF simulations of the selected days. Real-time GVF was used for coupled simulations, and NU-WRF provided atmospheric forcing to LIS.

Three simulations were performed for each date, a control (CTRL) simulation, a wet soil (WET) simulation and a dry soil simulation (DRY). CTRL simulations were initialized using land surface ICs from the offline LIS spinup. Both WET and DRY simulations used all land surface ICs from the LIS spinup except for soil moisture, which was prescribed instead. Soil moisture was prescribed at field capacity for all soil depths (0-10 cm, 10-40 cm, 40-100 cm, 100-200 cm) based upon the soil texture in each grid box

for WET simulations while soil moisture was prescribed at wilting point for DRY simulations. While vegetation health also serves as an important control for transpiration rate in the LSM, simply prescribing different soil moisture allowed for the simulation of how the observed state of vegetation may produce a different outcome if only soil moisture were changed. This approach produced sufficient variability between WET, DRY and CTRL simulations without introducing additional confounding factors that may arise from use of a more complex LSM.

Each simulation was initialized at 1800 UTC during the preceding day and run for 30 hours. For example, the 18 June simulation was initialized at 1800 UTC on 17 June and ended at 0000 UTC on 19 June. This allowed for the model to simulate PBL development and airmass response to surface fluxes upstream of the location of interest as well as locally. While simulations were occasionally performed for consecutive days, the simulations were not continuous. For example, the simulation for 18 June was performed separate from the simulation for 19 June. The thermodynamic characteristics of the residual layer exerts an important control on PBL growth (Findell and Eltahir 2003a), where a deep,dry-adiabatic, residual layer can encourage rapid PBL growth (Santanello Jr et al. 2005) such as those resulting from a PBL which developed over dry soils during the previous day (Santanello Jr et al. 2007). Milovac et al. (2016) showed that both local and non-local PBL parameterization schemes, including the scheme used in the current study (MYNN), produced a PBL that was too deep when compared to observations, thus resulting in a residual layer that was also too deep. This residual layer would likely bias PBL growth the following day, and without external influences, this bias would grow with time. Thus, to avoid such runaway effects, simulations were limited to 30 hours.

5.3 Observations versus Simulations

Atmospheric profiles were evaluated at multiple locations to gauge the CTRL simulation's ability to reproduce observed conditions. Composite mean profiles were computed from

CTRL, WET and DRY simulation output over a 30 km x 30 km domain centered upon each of 4 upper air stations (Fig. 5.4b). The size of domain surrounding each point was selected to ensure that vertical profiles were not influenced by grid scale variations in cloud cover that may impact temperature and humidity. Multiple sizes were tested with little difference observed between 10 km2 domains and 50 km2 domains. The 30 km2 domain also corresponds to roughly the same size as a single grid box in the North American Regional Reanalysis (NARR; Mesinger et al. 2006). The NARR was used to identify flash drought locations (Christian et al. 2019) and to perform a cursory analysis of land-atmosphere coupling during the 2012 flash drought in Basara et al. (2019), and thus, compositing over similarly sized grid spacing for this analysis enables greater intercomparison between studies. Finally, for the purposes of computing advection, this "composite" grid box size satisfies the Courant-Friedrichs-Lewy condition (Courant et al. 1928; Bakhvalov 2001), by balancing the size of the time step and the spatial resolution. This produced the best estimate of advection within the PBL using a finite differencing approach.

Flash drought evolution over north central Oklahoma was of primary interest in this study, however, because advection and upstream influences were also being considered, it was necessary to quantify how well the CTRL simulation reproduces observations throughout the domain. Spatially averaged potential temperature and mixing ratio profiles were computed over a 30 km $\times$ 30 km sub-domain centered upon the 4 upper air stations within the larger model domain, including the upper air station located at ARM SGP (LMN). Winds were primarily from the south or from the east for the selected cases, so stations analyzed were chosen to represent nearby and upwind regions. Additionally, DDC was selected to quantify biases when drought was ongoing, as it experienced intense drought during much of the study period and moisture gradients associated with the dryline were often positioned between DDC and LMN. Large differences near the surface were observed within the surface layer, however, the evaluation metrics employed in this study specifically exclude surface layer influences in an effort to quantify characteristics of the

mixed layer. Therefore, profiles are shown starting at approximately 20 mb above the mean surface pressure at each station.

Observed and simulated vertical profiles of moisture and temperature were nearly identical at 1200 UTC (Fig. 5.5). Differences between the 3 simulated profiles increased throughout the daytime hours (from 1200 to 2400 UTC) as PBL development varied between the simulations. Furthermore, CTRL simulations also showed greater deviation from observed profiles at the end of the daytime period (Fig. 5.6). Agreement between observed boundary layer temperature and moisture profiles and those simulated in CTRL were greatest when lower tropospheric winds were calm or when they had an easterly component. When lower tropospheric winds were southerly, profiles from the WET simulation displayed better agreement with observations.

A southerly wind direction was also consistent with higher wind speeds in general, and thus more advection. The model domain is slightly wider in the zonal direction, such that lateral boundary conditions from the south may have influenced the temperature and moisture profiles. The GFS has a tendency to underestimate relative humidity (Chaouch et al. 2017) such that propagation of this underestimation to observation location would have resulted in a dry and warm bias. In the case of the WET simulations, latent heat fluxes along the flow may have added sufficient moisture to counteract the warm and dry bias caused by the lateral boundary conditions while surface fluxes in the CTRL and DRY runs would not. In this case, the simulation would be correct for the wrong reasons because the WET simulation corrected pre-existing biases in the profile. Further exploration of these biases was performed via meridional and zonal cross sections that were aligned parallel to the mean wind through the LMN upper air site. Differences between CTRL and DRY simulations remained minor and therefore, results comparing only the CTRL and WET simulations are presented here.

Meridional cross sections of moisture and temperature centered upon the LMN upper air station show that mean mixing ratio differences between CTRL and WET simulations were minimized at 1200 and 1500 UTC on 18 June (Fig. 5.7a-d). The greatest differences between simulations were observed to the north, where drought intensity was greatest and furthest downstream from the southern boundary. Potential temperature and mixing ratio differences between the WET and CTRL simulations quickly increased as the PBL deepened, and they were maximized by 2100 and 2400 UTC(Fig. 5.7e-h). Once again, the maximum differences between simulations were observed in the northern portion of the cross-section. PBL heights also displayed the greatest differences further north.

At the southern boundary of the domain, differences in temperature and moisture profiles were smallest, as were differences in PBL depth. Such results suggest that the influence of the land surface on PBL evolution increased further from the lateral boundary that coincided with the prevailing wind direction, which, in this case was southerly. In other words, as the air mass entered the domain from the south and spent more time over the domain, it was modified by fluxes of heat and moisture from the land surface. Given the differences in soil moisture between WET and CTRL simulations, this resulted in a difference in surface fluxes, and thus differences in the level of air mass modification between simulations.

A similar result was observed on 22 July 2012 when winds were primarily from the east (Fig. 5.8). (Note: the 2100 and 2400 UTC cross- sections display a mixing ratio discontinuity at approximately -93°W. This was likely attributed to convection developing along the boundaries of the domain). Differences between simulations grew to their maximum values by late afternoon/early evening as the PBL deepened and was influenced by land surface fluxes. Once again differences between simulations were minimized at the eastern boundary and they were maximized further downstream, toward the western boundary. Yet, days with easterly flow did not produce large differences between observations and the CTRL simulations. One possible explanation is the proximity of the LMN upper

air station to the lateral boundaries. LMN is approximately 7°longitude from the eastern boundary of the domain, whereas it is only 5°from the southern boundary. Additionally, winds were generally stronger in the southerly flow cases resulting in less time for the land surface and atmosphere to interact within the coupled simulations.

With the above limitations in mind, the simulations all demonstrate a response of the PBL to the land surface and are thus, suitable for better understanding how soil moisture may impact drought development, especially for days with easterly flow. While there is greater confidence in simulations during days with easterly flow, all days were evaluated.

5.4 Evaluation metrics

A modified application of the mixing diagram approach (Santanello et al. 2009; 2011) was used to evaluate the evolution of daytime PBL heat and moisture budgets over the ARM SGP site within each of the simulations. A more detailed description of this framework was introduced in Chapter 3. Contributions from advection to PBL energy and moisture budgets may also be factored into the mixing diagram framework (Santanello et al. 2009; Santanello Jr et al. 2011), though these contributions are not often considered. When considering flash drought propagation via advective processes, advection must be considered in the analysis of PBL moisture and energy budgets. As such, a methodology for including advection will be introduced into this novel application of the mixing diagram framework.

Advection was computed using a centered finite differencing approach over aggregate domains that consisted of computing composite means of meteorological variables (zonal wind, meridional wind, specific humidity, potential temperature) over 30 km $\times$ 30 km sub-domains. The use of larger domains for the advection computations was motivated by the need to eliminate grid scale variability due to variations in cloud fraction, net radiation, temperature and moisture, and by the Courant-Friedrichs-Lewy Condition (Courant et al. 1928; Bakhvalov 2001) which states that the spatial interval (x) over which the finite differencing approach is being implemented must be less than the mean wind speed (U)

multiplied by the time step (Δt). This is represented by the Courant number (C), which ideally should be less than or equal to 1. A 30 km domain corresponds to an approximately $8 ms^{-1}$ average wind speed in the lower troposphere, which was realistic for the cases selected.

$$C = \frac{U\Delta t}{\Delta x} \tag{5.1}$$

Advection was computed between 0.1 z_i and 0.75 z_i, where z_i is the PBL height (PBLH) to remain consistent with the mixed layer mixing diagram approach. Advective fluxes were then transformed into energy per unit mass to be consistent with other variables in the mixing diagram moisture and energy budgets. This can be shown in (5.2):

$$L_v q_{adv} = L_v(\overline{\vec{V} \cdot \nabla q})\Delta t \tag{5.2}$$

where L_v is the latent heat of vaporization, $(\overline{\vec{V} \cdot \nabla q})$ is the average advection within the mixed layer and t is 3600 seconds. Potential temperature advective fluxes were computed similarly, replacing L_v with specific heat (C_p) and ∇q with $\nabla \theta$ where θ is potential temperature to obtain $C_p \theta_{adv}$

5.5 Mixing diagrams results

5.5.1 Initial dry-down cases, 15 May, 16 May, 23 May, 4 June

Soils were steadily drying during the middle and end of May as the initial phase of the flash drought was established. Nearby soil moisture observations from Oklahoma Mesonet sites indicated relatively moist soils at 25 and 60 cm depths (Figure 3) with the exception of the Marena (MARE) site, which was drier than the other five stations at 25 cm. Slightly more than 30% of the model domain was classified as abnormally dry or worse by the USDM during the week of 15 May, but nearly 75% of the domain was considered abnormally dry by 22 May, the following week. As such, the 15, 16, and 23 of May simulations capture

an important period of transition within the region as the impacts of the dry-down began to materialize in drought monitor observations.

Easterly winds characterized both daytime periods during 15 and 16 May, and observed profiles of moisture and temperature were well represented by CTRL simulations for each date. Mixing diagrams for each day and simulation are shown in Figure 5.9. PBL evolution on both 15 May and 16 May was characterized by an initial moistening and warming in all three simulations (CTRL, WET, and DRY) followed by a period of relatively rapid drying and warming in the early afternoon before becoming more consistent in the early afternoon when the PBL reached a steady depth (Fig. 5.10). Such results are characteristic of PBL evolution over intermediate soil moisture conditions (Santanello et al. 2009) as initial and final PBL moisture were similar. Indeed, soils were neither wet nor dry at nearby Mesonet sites during this time. Surface flux vectors displayed a similar Bowen ratio across all simulations, with the lowest occurring in the WET soil simulations. As soils were drying down, sufficient water was still available for evapotranspiration, and partitioning between latent and sensible heat fluxes was relatively equal. Interestingly, this is also true for the dry simulation despite being prescribed wilting point soil moisture. This is likely due to the land surface model evapotranspiration being a product of canopy transpiration as well as bare soil evaporation, and thus, sensitive to vegetation greenness in addition to soil moisture (Ek et al. 2003).

Advection was present during all four cases but contributed minimally toward PBL evolution in most cases and was considerably smaller in magnitude compared to entrainment and surface flux contributions toward the PBL moisture and energy budget. Slightly larger latent heat fluxes in the WET simulation, greater initial moisture and lower initial temperatures led to a cooler and more moist PBL at 2400 UTC than the other two simulations. The DRY simulation showed the greatest overall change in temperature, but little change in overall moisture content. Both DRY and CTRL produced similar temperature and moisture conditions at 2400 UTC.

Advection was slightly greater in magnitude for the 16 May DRY and CTRL simulations, with a moistening and cooling influence, but the overall magnitude of advective contributions remained relatively small compared to entrainment and surface fluxes. Despite advection contributing to cooling and moistening of the PBL in both simulations, CTRL and DRY once again produced the driest, warmest and deepest PBL at 2400 UTC. The overall contribution of advection within the WET simulation was negligible.

Mixing diagram curves on 23 May (Fig. 5.9c) were also relatively consistent with PBL evolution over intermediate soil moisture for the majority of the day, with the exception of the late afternoon/early evening hours. During this period a slight moistening of the PBL was shown by all 3 simulations. Such behavior is typically associated with PBL evolution over wet soils (Santanello et al. 2009). Unlike 15 and 16 May, surface Bowen ratios were noticeably greater for the CTRL and DRY simulations. While the DRY and CTRL simulations produced minimal cold and moist advection, the opposite was observed for the WET simulation, and the magnitude of advection in WET was also greater. All 3 simulations produced a similar level of drying due to entrainment. Though all 3 simulations began with the same initial moisture, and displayed similar levels of drying due to entrainment, the DRY and CTRL simulations still produced a much drier final PBL. In this case, the much greater magnitude of latent heat fluxes within the WET simulation appeared to offset drying due to both entrainment and advection to maintain a moister PBL. Surface fluxes are scaled to the depth of the PBL, which varied little between simulations (Fig. 5.10). *Therefore, it appears that differences in surface flux partitioning rather than flux magnitudes produced differences in daytime PBL evolution.* The overall vector magnitudes suggest that the combined PBL moisture and energy budget evolved similarly across all simulations. However, the major difference was how the evolution was partitioned into changes within moisture versus energy budgets. In the WET soil simulations this produced a slight moistening overall, while DRY and CTRL simulations dried slightly.

The beginning of June marked a temporary pause in the magnitude of drought intensification (Fig. 5.2), but was still characterized by steadily drying soils. Not surprisingly, PBL evolution was similar to the 3 dates analyzed in May, where intermediate soil moisture led to a PBL characterized primarily by warming and minimal change in moisture. As with 23 May, surface Bowen ratio was much greater for the WET simulation (Fig. 5.9d), and the overall magnitude of warming and drying was comparatively lower. All 3 simulations displayed slightly different magnitudes of advection, with the largest in the dry simulation, though these magnitudes were still relatively small compared to entrainment and surface fluxes. The CTRL and DRY simulations also began to display a slight tendency toward greater magnitudes of afternoon drying consistent with PBL evolution over dry soils (Santanello et al. 2009). DRY and CTRL simulations produced the greatest daytime drying even when all 3 simulations began with similar moisture content in the PBL. The larger contribution from surface fluxes to the PBL moisture/energy budget in the WET simulation (greater vector magnitude) was also partitioned toward latent heating, with a Bowen ratio less than 0.5. This enabled surface fluxes to moisten the PBL and counteract drying associated with entrainment. Finally, PBL depth also varied greatly between DRY, CTRL and WET simulations, such that surface fluxes were distributed over a much shallower depth in the WET simulations, and hence, the comparatively larger surface flux vector magnitude.

5.5.2 Mid to late June Dry-down: 18, 19, 28, 29 June

Mesoscale rainfall mid-June provided some recharge to dry soils (Fig. 5.3) near the ARM SGP site, but this localized relief was overshadowed by the continuously intensifying drought throughout the rest of the domain (Fig. 5.2). Soil moisture decreases in the latter half of June were much more rapid than those observed during the May dry-down minimizing any localized recharge.

Surface Bowen ratios continued to show greater differences between CTRL, DRY and WET simulations for 18, 19, 28 and 29 June. Advection contributions toward PBL

energy and moisture budgets were relatively greater than those observed in May and early June(Fig. 5.12). Similarly, late June was characterized by southerly flow that once again resulted in a warm, dry bias within CTRL PBL profiles. Even with a cooling and moistening contribution from advection, the CTRL and DRY PBL evolution was characterized by greater overall warming and drying compared to the WET simulation on 18 June. Drying of the PBL was also isolated to the late afternoon/evening hours for all 3 simulations, similar to PBL evolution observed during the 15 and 16 of May.

Mixing diagram curves on 19, 28 and 29 June were all consistent with PBL evolution over dry soils presented in Santanello et al. (2009). Early morning moistening and warming was countered by rapid drying in the afternoon. As the PBL deepened, a rapid transition from moistening to drying was accompanied by the most rapid deepening of the PBL (Fig. 5.13). Additionally, the slower growth rate of the WET simulation PBL resulted in this period of rapid deepening occurring later in time, typically an hour later, than in DRY and CTRL simulations. The slower PBL growth in WET simulations resulted in an overall shallower, moister PBL with higher ratio of ET to PET (Fig. 5.14).

5.5.3 Amplification/Perpetuation of Drought: 11 July, 22 July, 27 July

While the period of rapid drought intensification was largely over, the transition into long term drought began. It is hypothesized that land-atmosphere interactions played a role in amplifying the already hostile atmospheric conditions that were driven by larger scale atmospheric features. Such feedbacks arise when soil moisture is sufficiently depleted to a tipping point in which the atmosphere becomes hypersensitive to land-atmosphere interactions, and elevated sensible heat fluxes contribute to development or amplification of heat waves (Benson and Dirmeyer 2021). While the focus of this study is on drought, increased temperatures associated with land-atmosphere coupling fueled heatwaves can exacerbate existing drought.

Mixing diagrams during July indicated rapid drying of the daytime PBL (Fig. 5.15), even when initial atmospheric moisture was greater than some of the earlier cases. Drying was characteristic of all July cases, but most pronounced at the end of July. Mixing diagrams from 11 July(Fig. 5.15a) displayed some moist advection which counteracted drying due to entrainment and surface fluxes in CTRL and DRY simulations to provide some moderation to PBL drying. Even with significant amounts of drying during the day, WET simulations still produced an overall cooler and moister PBL in all cases. However, the combination of atmospheric and surface conditions produced some of the greatest PBL depths during July and the frequently observed period of rapid PBL growth also occurred earlier than during previous cases (Fig. 5.16). Even so, WET simulations continued to display shallower PBL depths and a later period of rapid deepening than CTRL and DRY simulations. PET and ET timeseries also show that daytime ET continued to decrease over time for DRY and CTRL simulations, even when PET was large, while WET simulations maintained a relatively constant rate of ET and PET throughout the 11 cases analyzed in this study (Figs. 5.11, 5.14, 5.17).

5.6 Discussion and Conclusions

The four days selected for analysis during the first phase of flash drought in May and early June, presented evidence of a slow shift toward a drying PBL regime when compared to the results of SSantanello et al. (2009). The first two days analyzed, 15 May and 16 May, displayed moistening in the early morning as sufficient fluxes of moisture from the land surface were distributed over a relatively shallow PBL in all three simulations. However, all three simulations displayed a period of rapid PBL growth between 1600 and 1800 UTC on 15 May, consistent with entrainment of a well-mixed residual layer (Lothon et al. 2014). Larger surface Bowen ratios in CTRL and DRY resulted in greater PBL warming and earlier rapid growth/entrainment of the residual layer. A similar result was also observed on 16 May, but less pronounced than during the preceding day. Early morning moistening on

23 May and 4 June was nearly non-existent and PBL evolution was primarily characterized by warming, suggesting a PBL growth regime over soils that were still moist enough to produce a relatively equal portioning between surface latent and sensible heat fluxes. The mid to late June cases signaled a steady progression toward PBL evolution more consistent with that expected over dry soils as mixing diagrams indicated greater warming and drying throughout the day (Santanello et al. 2009). A dry soil-type PBL evolution was characteristic of all cases by July. Even WET soil simulations produced a drying PBL during June and July, but the magnitude of drying and warming was suppressed in comparison to the CTRL and DRY simulations.

The tendency for the PBL to dry and warm even over wet soils during June and July cases suggests that surface fluxes played some role in PBL evolution, but were also behaving against a larger scale background state favorable for drought. This is further supported by the fact that vertical profiles of moisture at 1200 UTC were similar among WET, DRY and CTRL simulations and only began to deviate from one another as the PBL evolved. As such, this study presents an interesting interplay between a hostile background atmospheric state and the potential influence of the land surface on the atmosphere during an extreme event. Erfanian and Fu (2019) showed that advection of low relative humidity air above the PBL enhanced PBL drying due to entrainment during the 2012 (and 2011) drought. Entrainment of dry air into the PBL is sensitive to surface flux partitioning (Milovac et al. 2016) so based on the current results, wet soils could have, at least temporarily, produced a shallower, moister and cooler PBL given the same background atmospheric state that was driving drought during 2012, and offset some of the drying due to entrainment of dry air that had been advected above the PBL. While this conclusion is largely based on model simulation output, similar results have been observed in situ over wet soils in Oklahoma (Basara and Crawford 2002). Thus, it is possible that land-atmosphere feedbacks over wet soils could limit atmospheric demand by moistening the PBL.

The potential feedback between ET and PET was explored further in timeseries of daytime ET and PET evolution (Figs. 11, 14, 17). All cases show a consistent peak in PET and ET from 1800 to 2200 UTC, with WET simulations producing the smallest difference between PET and ET at all times. Even though atmospheric demand (PET) was smaller for the WET simulations, ET was greater while for the same magnitudes of PET, ET was smaller in CTRL and DRY simulations. These results indicate a moisture limited state rather than energy limited, in which soil moisture regulates the magnitude of ET (Budyko 1961). If this were an energy limited environment, it is expected that smaller magnitudes of PET in WET simulations would produce smaller magnitudes of ET. Interestingly, the initial profiles of moisture and temperature were similar across all simulations. PET and ET were also relatively similar between simulations during the first couple of hours of the day, with differences becoming maximized as the daytime PBL evolved differently between simulations. This suggests that greater ET in WET simulations also produced a slight moderating effect that reduced PET (i.e., evaporative demand) in the PBL.

Daytime (1200 to 2400 UTC) cumulative ET and PET were computed at all grid points within a 2°by 2°domain centered upon LMN. The ratio of cumulative ET to cumulative PET, otherwise known as the Evaporative Stress Ratio (ESR), was then computed to obtain distributions of ESR over the sub-domain for each case and simulation. The objective of this final analysis was to compare changes in ESR over the May through July 2012 study period, and to compare these changes to a well-tested index used to identify flash drought; the standardized evaporative stress ratio (SESR; Christian et al. 2019).The choice of domain size was intended to facilitate comparison with the results of Christian et al. (2019), in which flash droughts were identified on a grid with lower spatial resolution. Selecting the 2°by 2°size allowed for several grid boxes from the Christian et al. (2019) analysis to be included in the composite. SESR also standardizes ESR based upon climatology, and thus, this is not a perfect 1:1 comparison within this study for magnitudes. Even so, mean ESR and SESR are highly correlated ($p>0.05$) for the 3 simulations with

CTRL ($R^2 = 0.90$) and DRY ($R^2 = 0.86$) displaying the best agreement with SESR and WET displaying the least ($R^2 = 0.73$). This is not surprising as the WET simulations produce the greatest change to PET and ET. Further details of the computation of SESR can be found in Christian et al. (2019).

WET soil simulations consistently produced a higher ESR (Fig. 5.18), indicating that ET was better able to meet atmospheric demand, and/or that atmospheric demand was reduced. In fact, both cases were true. PET was reduced in WET simulations while ET was enhanced. Furthermore, though all simulations displayed an overall decrease in ESR, consistent with atmospheric demand overpowering ET, this decrease was not as obvious for WET simulations. The ESR patterns also closely followed patterns in SESR throughout the period of study. All the simulations produced relatively constant ESR values in late June and early July, consistent with steadier state SESR values during the same time. Given the same tendency toward a steady state ratio of ET to PET, the remaining question is whether ESR produced by WET simulations would be sufficiently large in comparison to climatology to produce less negative SESR values and less extreme drought.

Additionally, this study noted that the response of the PBL to initially-biased air masses over WET soil simulations. Fluxes of moisture from the surface moistened and cooled the PBL across the domain, while the lack of moisture fluxes in CTRL and DRY simulations allowed those biases to remain and propagate throughout the domain. This has implications for forecasting, as biases due to lateral boundary conditions may be more evident only over certain soil moisture conditions.

While the cases analyzed are only a small subset of the entire 2012 flash drought event and overall drought period, they provide insight into the relative influence soil moisture may have had in amplifying drought through local and upstream fluxes. In this analysis it was proposed that dry soils played a role in amplifying the 2012 flash drought and drought in the Southern Great Plains. The proposed mechanisms through which dry soils amplified this event are both local and upstream. Locally, dry soils drive greater PBL depths, along

with higher surface sensible heat fluxes, and entrainment of dry free tropospheric air all of which increase evaporative demand within the PBL.

Advection of warm, dry air above the influenced the evolution of the 2011 and 2012 droughts over the Great Plains (Erfanian and Fu 2019) as entrainment of the low relative humidity air likely increased evaporative demand within the PBL (Milovac et al. 2016). Dry soils were unable to balance this demand through increased moisture fluxes resulting in a net drying and warming. The results of the current study suggest that dry soils enhanced the effects of above PBL advection through deeper PBL development that (a) entrained more dry air and (b) diluting any surface moisture fluxes by distributing them over a deeper mixed layer. Despite similar initial profiles of moisture and temperature, WET simulations consistently produced shallower PBL depths, and the disparity between ET and PET was much smaller in WET simulations than in CTRL and DRY simulations. *Advection within the PBL played a much smaller role in the overall evolution of PBL moisture and temperature for the cases analyzed in this study, with surface fluxes and entrainment fluxes dominating the moisture and energy budgets.*

The results of this study suggest that local land-atmosphere feedbacks played an important role in regulating PBL moisture and energy budgets, with wet soils producing greater surface fluxes of moisture and lower evaporative demand. It is still somewhat unclear whether the response of the PBL over the sub-domain analyzed in this study was related to wet soils being prescribed across the entire model domain or whether it was a response of the PBL to local soil moisture conditions. One approach to answering this question could prescribe wet soils locally, however this would present unique challenges related to land-atmosphere coupling. Soil moisture gradients, such as those that would arise from only perturbing soil moisture in a sub-domain, can be associated with convective initiation (Frye and Mote 2010; Taylor et al. 2011).

The 2012 drought and flash drought was likely influenced by internal climate variability (Hoerling et al. 2014). Further, drought in the Great Plains region is often driven

by changes in the large-scale atmospheric circulation driven by remote sea surface temperature anomalies (Trenberth et al. 1988; Seager et al. 2005; Schubert et al. 2008, 2009; Seager and Hoerling 2014) producing widespread subsidence and precipitation suppression over the region, which favors drought (Basara et al. 2013). Indeed, this would explain the relatively consistent background atmospheric state across model simulations in the early morning despite large differences in soil moisture conditions. Even so, Basara et al. (2019) provided evidence that land-atmosphere interactions still played a role in the evolution of the 2012 flash drought and drought. The results presented in this analysis indicate sensitivity of the PBL itself to differences in soil moisture, such that wetter soils would increase ET and reduce PET locally. Thus, this study demonstrates that the 2012 drought and flash drought was influenced by a combination of favorable large-scale atmospheric conditions and land-atmosphere feedbacks that amplified already extreme conditions.

Future studies should apply these methods toward evaluation of additional flash drought events in the same region, as well as in other geographic regions. It is likely that the sensitivity of extreme events to land-atmosphere feedbacks will vary based upon geography as the Great Plains is considered especially favorable for land-atmosphere coupling (Koster et al. 2004; Guo et al. 2006; Koster et al. 2006). Additionally, null cases with rapid dry-down periods that did not end in drought should also be evaluated, to better understand the role of the land surface as well as the role of the large-scale atmospheric conditions that were favorable for rapid drying of the land surface but did not result in a true flash drought.

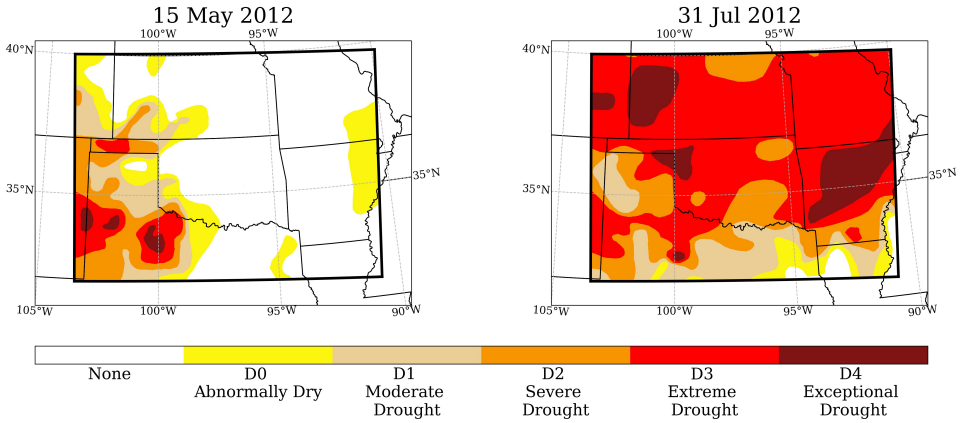

Figure 5.1: United States Drought Monitor for beginning (15 May 2012) and end (31 July 2012) of the analysis period.

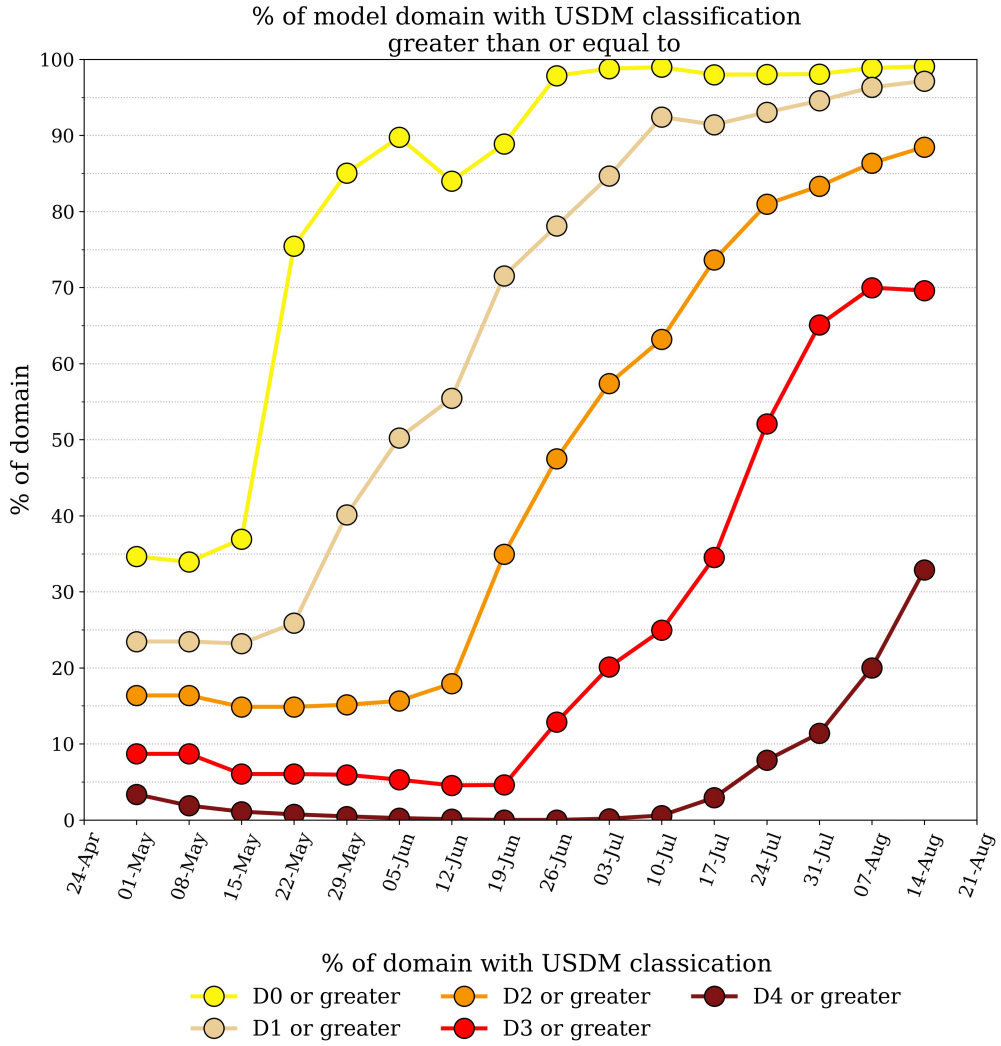

Figure 5.2: United States Drought Monitor classification timeseries during 2012 displaying the percentage of the model domain greater than or equal to a given intensity category.

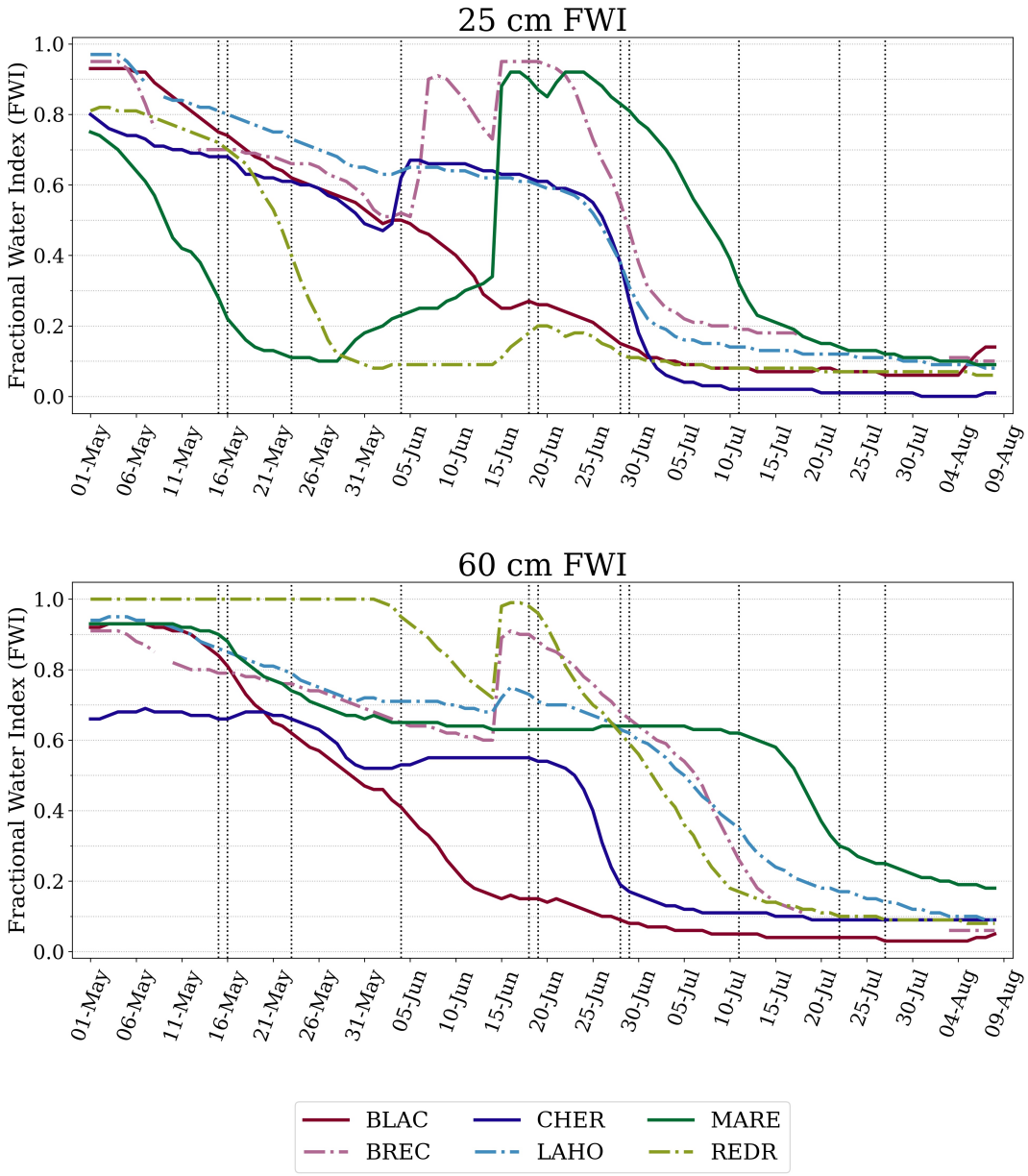

Figure 5.3: The (a) 25 cm and (b) 60 cm fractional water index (FWI; Schneider et al. 2003) for selected Mesonet stations during analysis period, where a value of 1 corresponds to saturated soils and a value of 0 corresponds to soils which are completely dry.

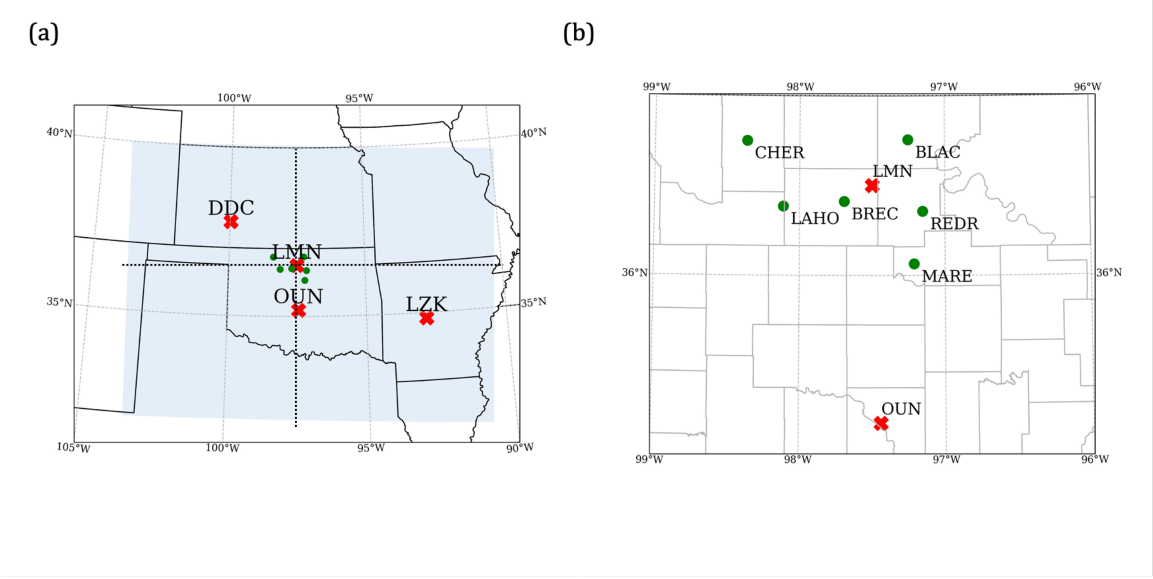

Figure 5.4: (a) Study domain shaded in light blue with a red "X" indicating each upper air station used for comparison to simulation output shown and (b) zoomed in to portion of domain near LMN upper air station with Mesonet stations from which soil moisture was data was obtained indicated by a green circle. Dotted lines from south to north, and from west to east represnt location of cross-sections taken in Figure 5.7 and Figure 5.8 respectively

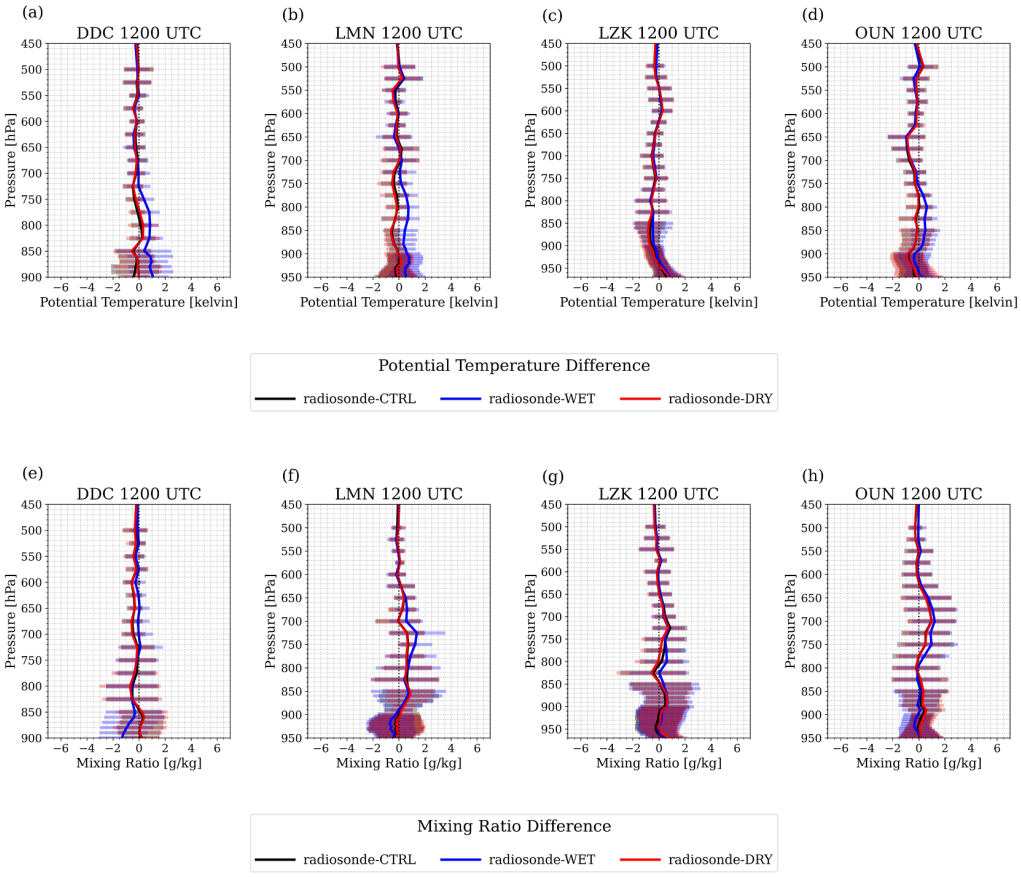

Figure 5.5: (a-d) Simulation composite mean potential temperature profiles at 1200 UTC subtracted from observed composite mean potential profiles at 1200 UTC for the 4 upper air sites. Composite means were computed over the 11 days simulated. (e-h) as in (a-d) but for mixing ratio. Horizontal bars represent ±1 standard deviation.

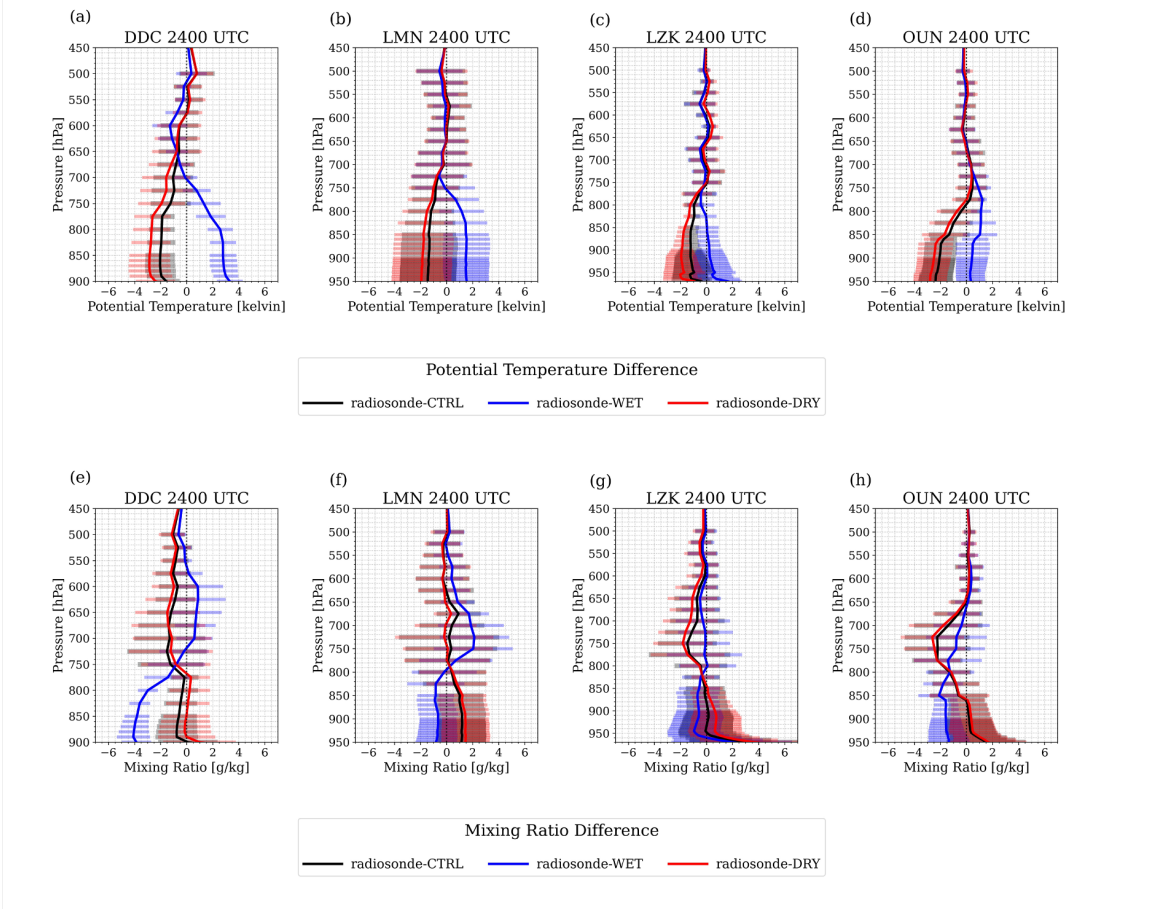

Figure 5.6: As in figure 5.5, but for profiles at 2400 UTC.

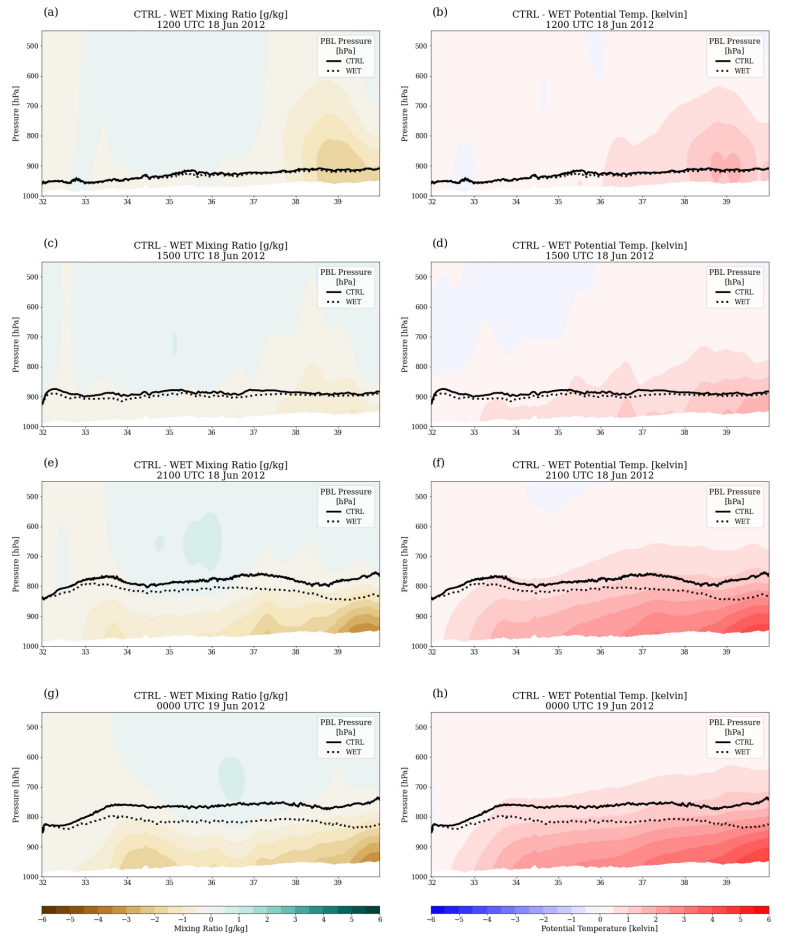

Figure 5.7: Meridional cross sections of mixing ratio and potential temperature differences between CTRL and WET simulation cross sections on 18 June 2012 at (a-b) 1200 UTC (c-d) 1500 UTC (e-f) 2100 UTC and (g-h) 0000 UTC on 19 June. Solid black lines indicate PBL depth in CTRL simulation and dashed lines indicate PBL depth in WET simulation. Cross sections were computed from mean values within a 10 km distance from the line connecting latitudes 32°N to 39°N

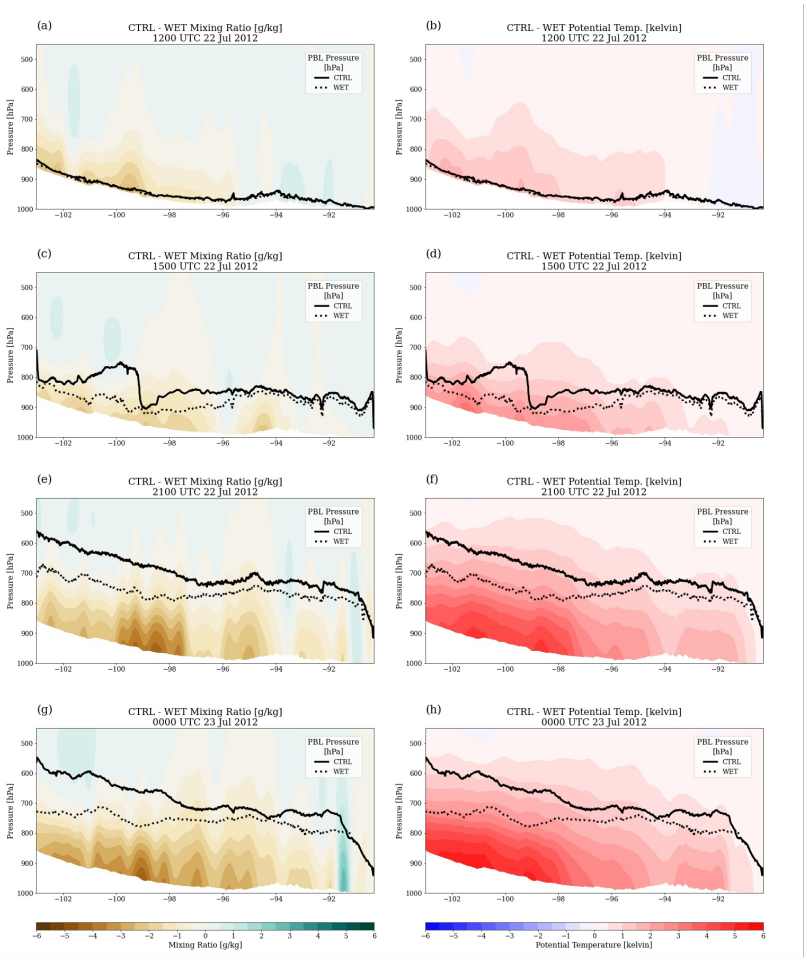

Figure 5.8: Zonal difference cross sections as in figure 7 but for 22 July 2012 at (a-b) 1200 UTC, (c-d) 1500 UTC (e-f) 2100 UTC and (g-h) 0000 UTC on 23 July 2012. Cross sections were computed from mean values within a 10 km distance from the line connecting longitudes -103°W to -90°W.

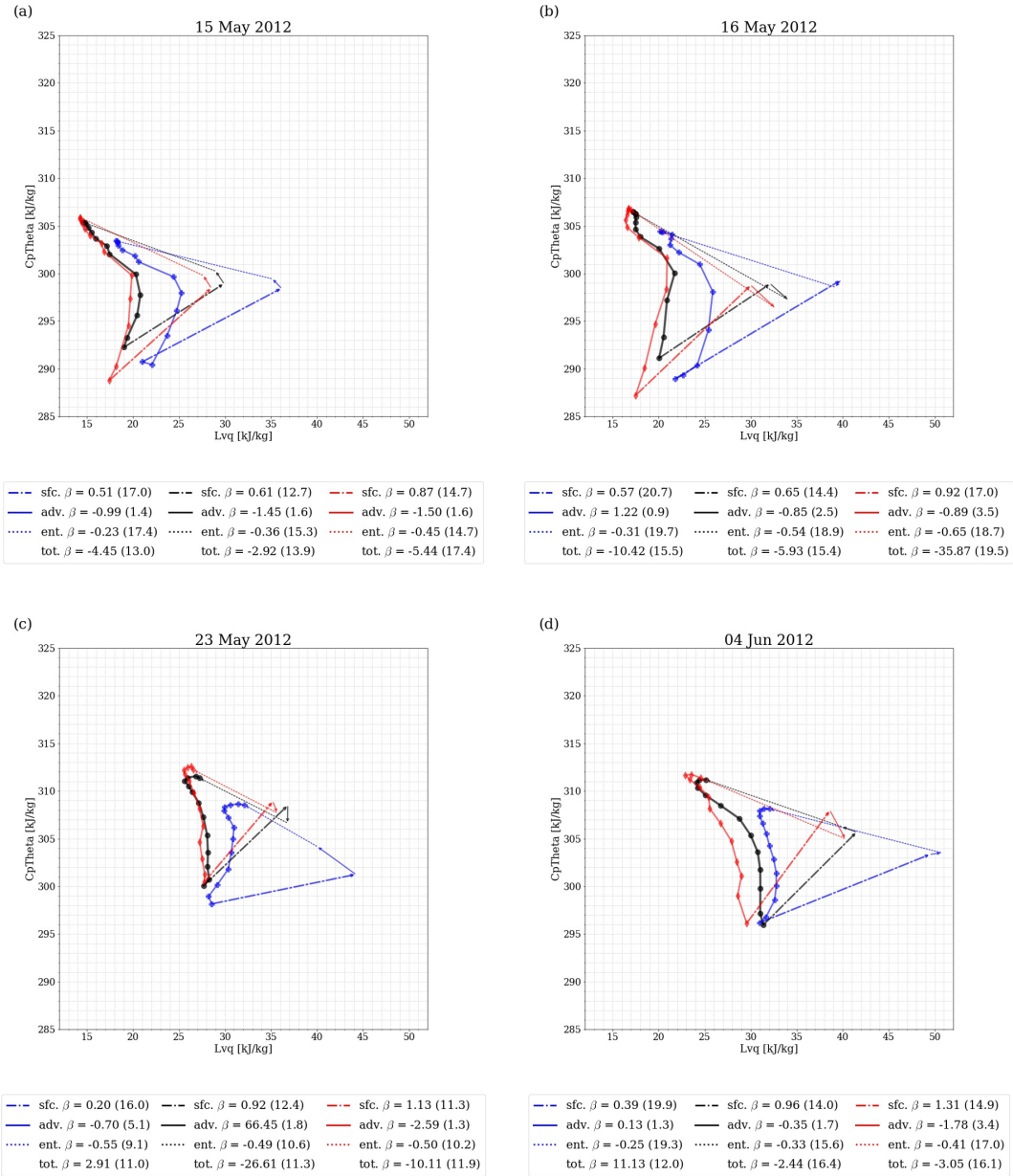
(a)
15 May 2012
(b)
16 May 2012
(c)
23 May 2012
(d)
04 Jun 2012
CpTheta [kJ/kg]
Lvq [kJ/kg]
sfc. β = 0.51 (17.0)
adv. β = -0.99 (1.4)
ent. β = -0.23 (17.4)
tot. β = -4.45 (13.0)
sfc. β = 0.61 (12.7)
adv. β = -1.45 (1.6)
ent. β = -0.36 (15.3)
tot. β = -2.92 (13.9)
sfc. β = 0.87 (14.7)
adv. β = -1.50 (1.6)
ent. β = -0.45 (14.7)
tot. β = -5.44 (17.4)
sfc. β = 0.57 (20.7)
adv. β = 1.22 (0.9)
ent. β = -0.31 (19.7)
tot. β = -10.42 (15.5)
sfc. β = 0.65 (14.4)
adv. β = -0.85 (2.5)
ent. β = -0.54 (18.9)
tot. β = -5.93 (15.4)
sfc. β = 0.92 (17.0)
adv. β = -0.89 (3.5)
ent. β = -0.65 (18.7)
tot. β = -35.87 (19.5)
sfc. β = 0.20 (16.0)
adv. β = -0.70 (5.1)
ent. β = -0.55 (9.1)
tot. β = 2.91 (11.0)
sfc. β = 0.92 (12.4)
adv. β = 66.45 (1.8)
ent. β = -0.49 (10.6)
tot. β = -26.61 (11.3)
sfc. β = 1.13 (11.3)
adv. β = -2.59 (1.3)
ent. β = -0.50 (10.2)
tot. β = -10.11 (11.9)
sfc. β = 0.39 (19.9)
adv. β = 0.13 (1.3)
ent. β = -0.25 (19.3)
tot. β = 11.13 (12.0)
sfc. β = 0.96 (14.0)
adv. β = -0.35 (1.7)
ent. β = -0.33 (15.6)
tot. β = -2.44 (16.4)
sfc. β = 1.31 (14.9)
adv. β = -1.78 (3.4)
ent. β = -0.41 (17.0)
tot. β = -3.05 (16.1)

Figure 5.9: Mixing diagrams for (a) 15 May 2012, (b) 16 May 2012, (c) 23 May 2012, (d) 4 June 2012. The moisture budget of the PBL is represented by values along the x-axis while the energy budget is represented by values along the y-axis. CTRL simulation curves are shown by black curve and markers, WET simulations by blue curve and markers and DRY simulations by red curve and markers. Markers represent each hour of the daytime PBL evolution from 1200 to 2400 UTC. Surface flux contributions are shown using the vectors with the dash-dot line for each curve, dashed vectors show contributions from entrainment and solid vectors show contributions from advection. Bowen ratios for each vector are shown in tables below each plot and the magnitude of each vector is indicated in parentheses next to the Bowen ratio. Vectors representing the total evolution of PBL moisture and energy budgets are not shown, however, Bowen ratio and magnitude data are included for comparison. Surface vectors point away from 1200 UTC values of each mixing diagram curve.

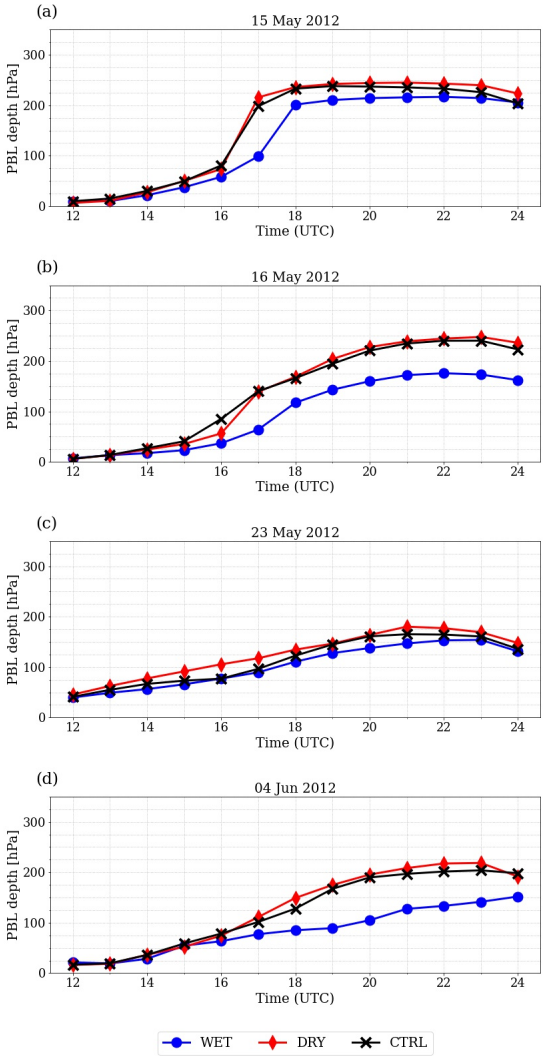

Figure 5.10: PBL depth for each date shown in Figure 5.9

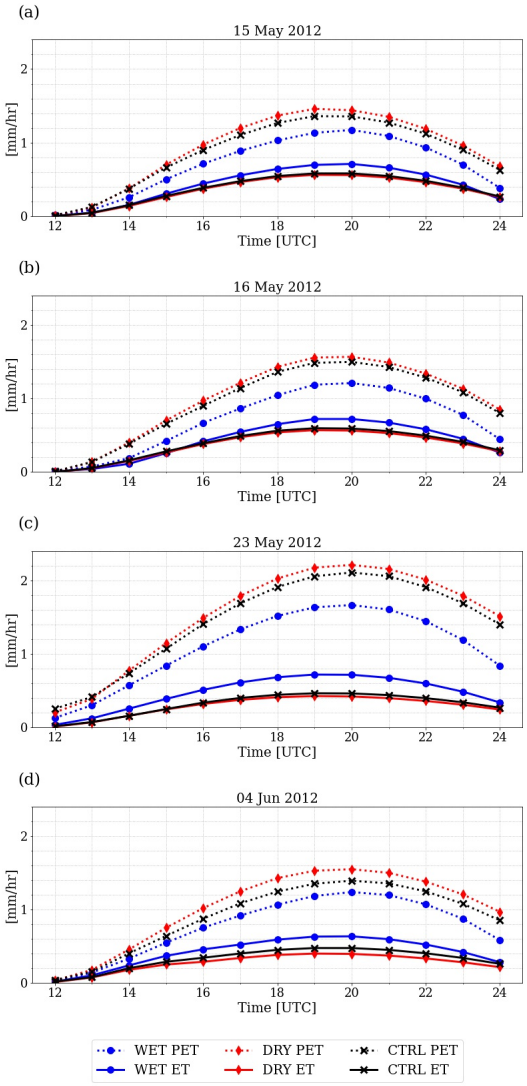

Figure 5.11: Potential evapotranspiration (PET, dashed line) and evapotranspiration (ET, solid line) curves in mm/hr for each date in Figure 5.9. CTRL simulations are shown in black with "x" marker, WET simulations are shown by blue lines with circular markers, and DRY simulations are shown by red lines with diamond markers.

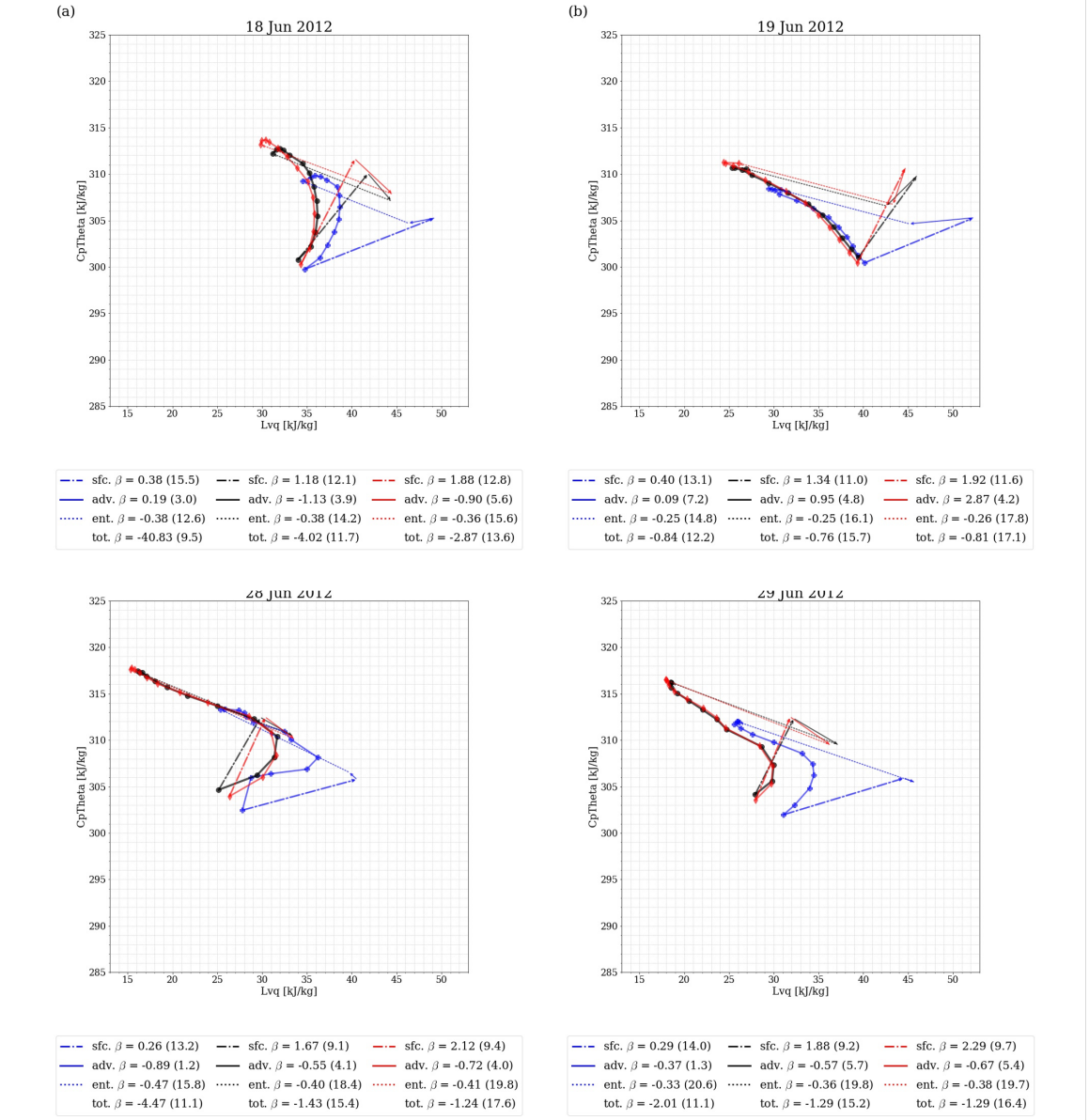

Figure 5.12: As in Figure 5.9 but for (a) 18 June 2012, (b) 19 June 2012, (c) 28 June 2012, (d) 29 June 2012.

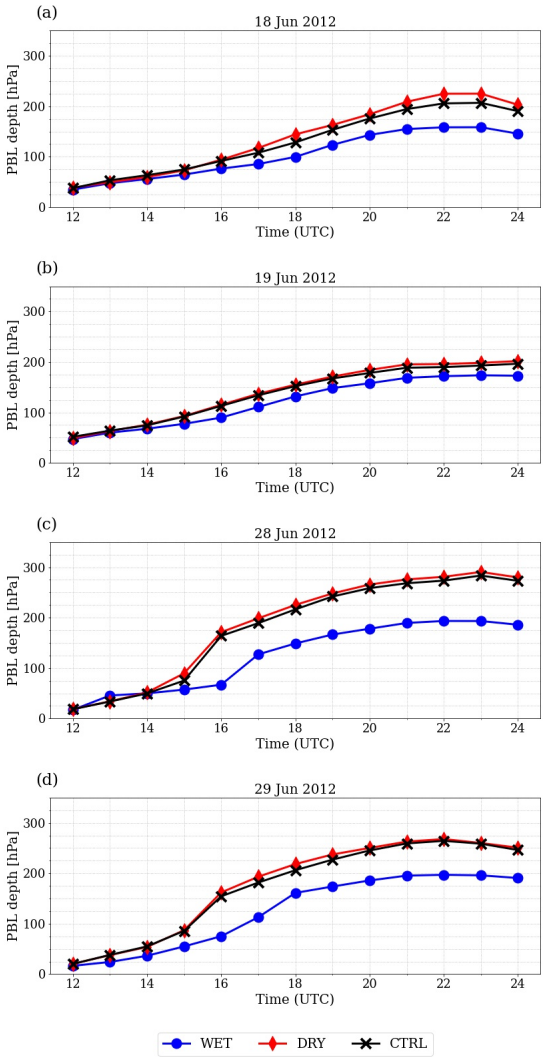

Figure 5.13: As in Figure 5.10 but for dates shown in Figure 5.12.

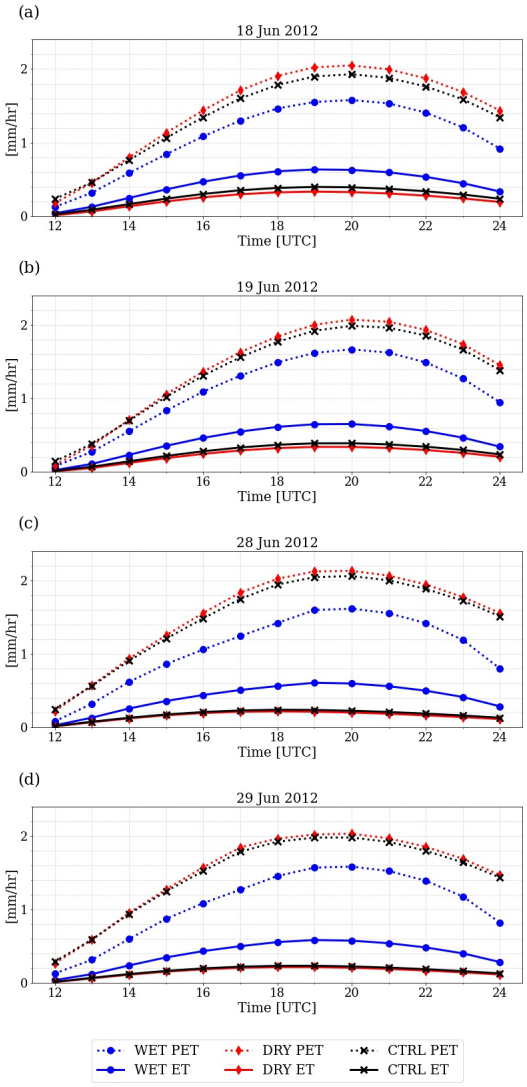

Figure 5.14: As in Figure 5.11 but for dates shown in Figure 5.12.

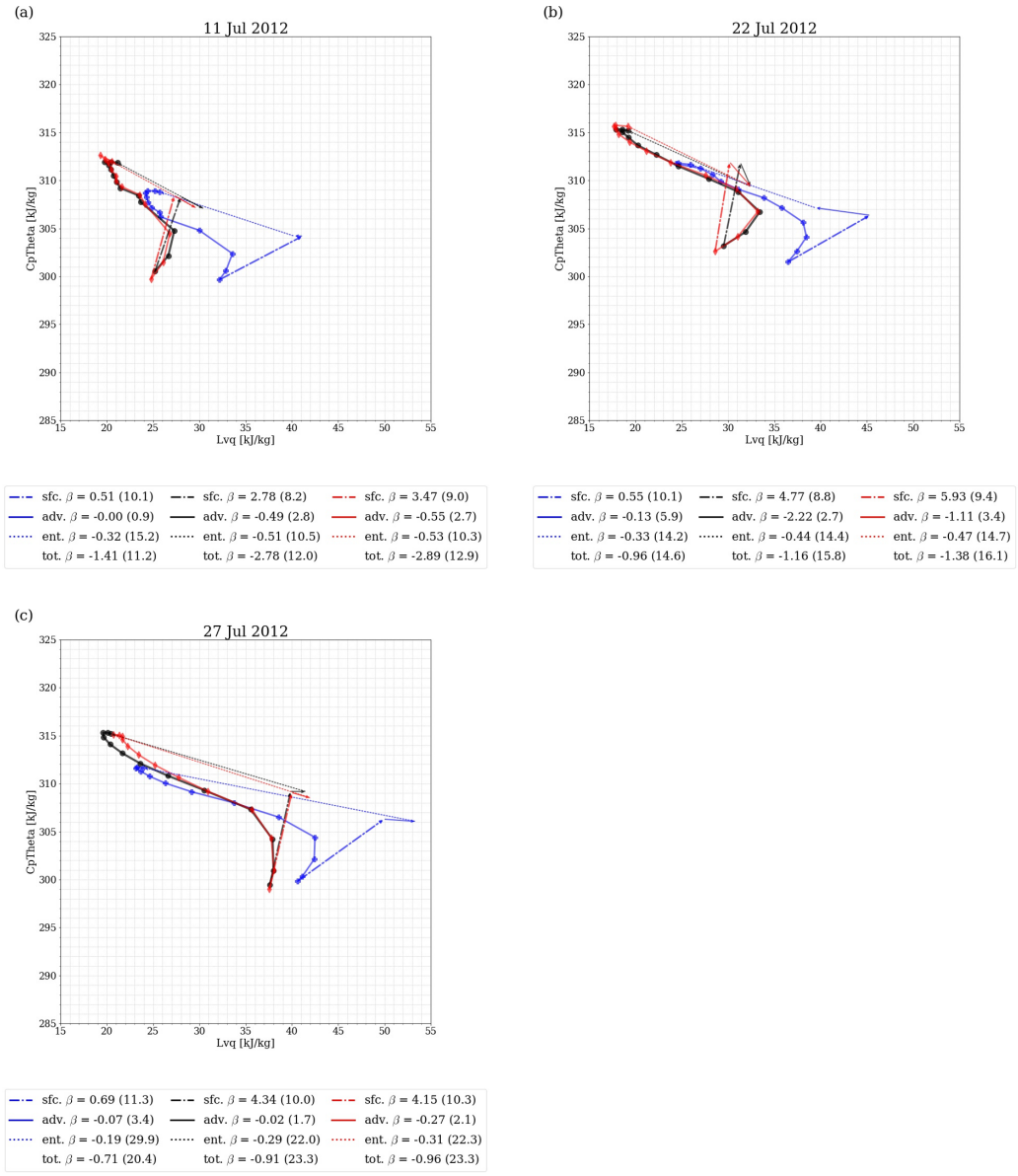

Figure 5.15: As in Figure 5.9 but for (a) 11 July 2012, (b) 22 July 2012, (c) 27 July 2012

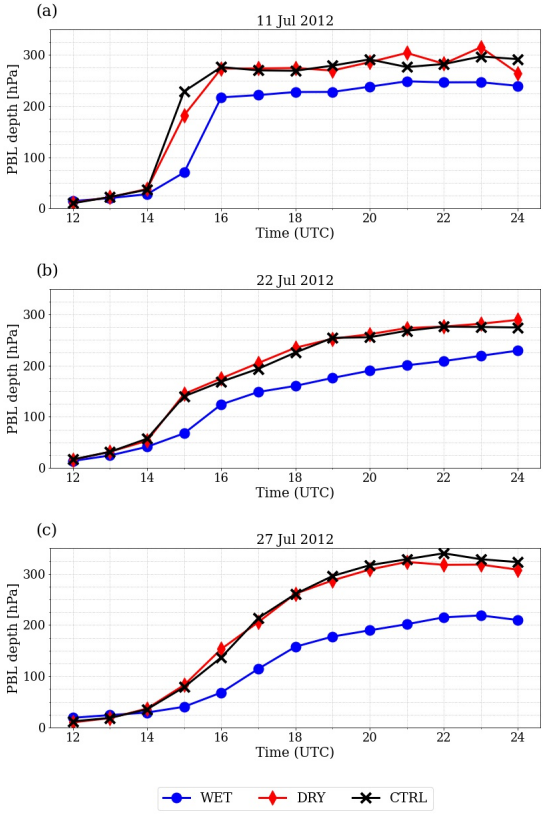

Figure 5.16: As in Figure 5.10 but for dates shown in Figure 5.15.

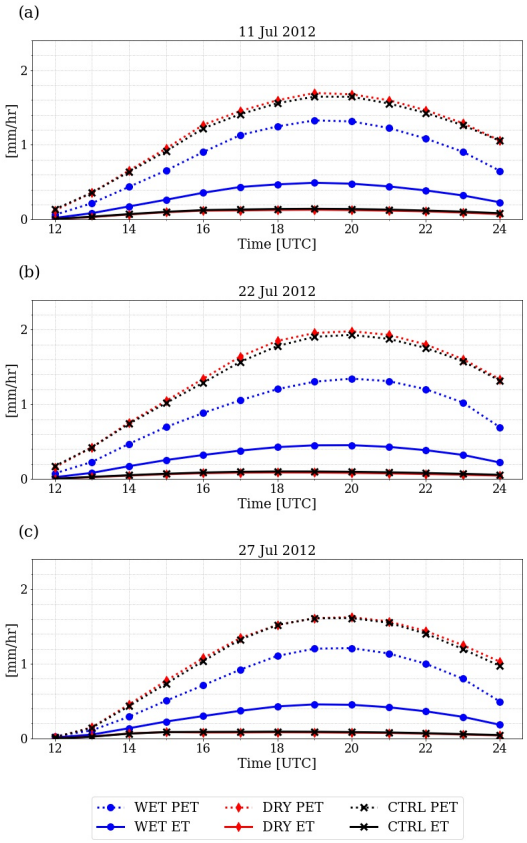

Figure 5.17: As in Figure 5.11 but for dates shown in Figure 5.15.

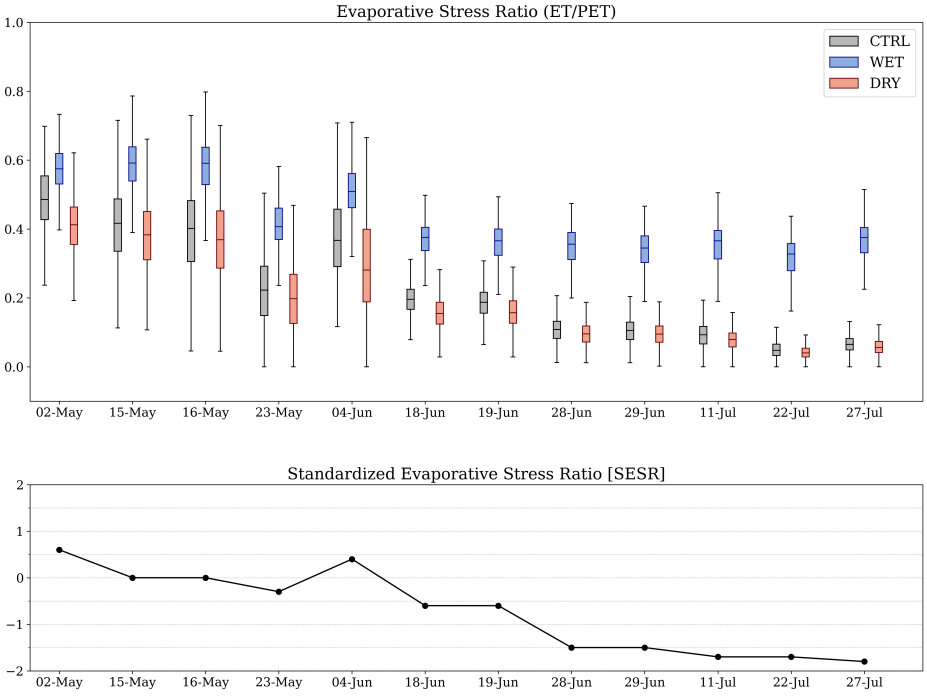

Figure 5.18: (a) Distributions of ET to PET ratio (ESR) for each date simulated. ESR values were obtained from cumulative daily ET and PET over a 2°by 2°domain centered upon LMN. (b) Composite mean standardized evaporative stress ratio (SESR) for simulation dates averaged over the same domain used in (a).

Chapter 6

Conclusions

The Great Plains is characterized by hydroclimate extremes. For example, landfalling tropical cyclones may maintain intensity far inland over the same region impacted by devastating drought in prior years. Such extreme events are often driven by anomalous large-scale atmospheric forcing; however, land-atmosphere feedbacks may also amplify these extreme events. As such, the broader, primary objective of this work was to more definitively quantify the relative role of land-atmosphere feedbacks against background atmospheric states that were already favorable for a dearth or an excess of precipitation. More specifically, this study hypothesized that anomalously wet soils provide sufficient fluxes to support the overland maintenance and reintensification of a landfalling Tropical Cyclone while on the opposite end of the precipitation distribution, excessive sensible heat fluxes from anomalously dry soils intensified and exacerbated drought.

Soil moisture extremes are communicated to the atmosphere through fluxes of heat and moisture which influence the development of the planetary boundary layer (Basara and Crawford 2002) and its moisture and energy budgets. Various land-atmosphere coupling metrics have been developed to quantify the potential atmospheric response to such soil moisture extremes, and several rely on vertical profiles of moisture and temperature in the lower troposphere to do so. Thus, a logical first step in this dissertation was to determine land-atmosphere coupling metrics that could be used to address the above hypotheses and extreme events. This was completed by leveraging observational platforms within the ARM Southern Great Plains site to test and improve two existing coupling metrics: the Convective Triggering Potential and Low-Level Humidity Index (CTP-HI_{low} Findell and Eltahir 2003a,b) and the mixing diagram framework (Santanello et al. 2009).

6.1 Identifying an Optimal Land-Atmosphere Coupling Framework

Analyses implementing the CTP-HI_{low} framework are frequently used to diagnose whether the atmosphere is pre-conditioned for convection initiation over wet or dry soils, and diagnosis is performed using 1200 UTC radiosonde observations only. This metric can be compared to climatology to determine whether atmospheric preconditioning over a region is more consistent with drier than normal conditions (Wakefield et al. 2019)). Application of this metric comes with several limitations however, the first being its dependence on vertical profiles of moisture and temperature which are limited to a sparse distribution of upper air stations. In Chapter 2 this study showcased the utility of ground-based remote sensing platforms, particularly the Atmospheric Emitted Radiance Interferometer (AERI) for providing profiles of moisture and temperature, and thus enabling computations of CTP and HI in locations where radiosondes are absent. Even so, this study highlighted limitations related to the time dependence of the framework. The framework diagnoses the early morning atmosphere (defined in this study between approximately 0500 and 0800 local time), which for most of the continental United States, corresponds to the 1200 UTC sounding. CTP and HI computed further in time from 1200 UTC at the ARM SGP site produced different diagnoses of atmospheric pre-conditioning than those computed at 1200 UTC. Thus, the requirement that the metric diagnoses the early morning atmosphere, precludes its application in regions where neither the 1200 UTC or 0000 UTC soundings correspond to early morning. Finally, while the framework provides information about layers of the atmosphere likely to be incorporated into the daytime boundary layer, it does not characterize the daytime PBL as it evolves.

Given the results of Chapter 2, a second metric, the mixing diagram framework was evaluated using the AERI. The mixing diagram framework traditionally uses the evolution of surface temperature and moisture to characterize the evolution of the daytime PBL moisture and energy budgets and assumes these values are representative of the well-mixed PBL as a whole. This is motivated by the greater availability of surface observations and lack of

PBL profiles of moisture and temperature. The high temporal resolution of the AERI enabled computation of mixed layer moisture and temperature to characterize the evolution of the daytime PBL and these results were compared to those using surface observations only. The mixed layer observations eliminated influences from the surface layer and entrainment zone, better characterized the daytime PBL, and was more likely to lead to closure of the moisture and energy budgets. This modification of the mixing diagram framework was later implemented to quantify the role of land-atmosphere feedbacks during the 2012 flash drought and drought (Chapter 5).

6.2 Surface flux contributions toward the fate of a landfalling tropical cyclone

The analysis of Tropical Storm (TS) Bill (2015) did not implement a specific land-atmosphere coupling framework, as these frameworks are often best suited for conditions in which synoptic drivers of precipitation are absent. Instead, the water vapor budget within the storm's antecedent environment and along its inflow was compared to that of storms which decayed rapidly following landfall and that of Tropical Storm Erin (2007) which also maintained/reintensified over land.

The results of this analysis showed that for tropical cyclones that maintained intensity or reintensified over land, accumulated evapotranspiration (ET) along the path of inflow parcels was greater (p¿0.05) than accumulated ET along the inflow of storms that decayed rapidly after landfall. Moreover, much of the accumulated ET along inflow parcels during TS Bill originated over land suggesting that fluxes of moisture from wet soils were sufficient to sustain a tropical cyclone over land. The large magnitudes of ET upstream of TS Bill over land were also likely enabled by the storm's direction of propagation. Over land, ET exhibits a diurnal cycle and is sensitive to downwelling shortwave radiation, atmospheric relative humidity, and wind speed as well as vegetation type and soil moisture. Storms which decayed rapidly over land either lacked sufficient downwelling shortwave

radiation or soil moisture upstream of the tropical cyclone. The propagation of TS Bill meant that cloud cover associated with its circulation did not remain too long over a given region upstream. Because soils in upstream regions were (a) already moistened by above normal rainfall prior to the landfall of TS Bill or (b) were moistened by the storm itself, ET was neither limited by soil moisture nor available energy from solar radiation.

The circulation associated with TS Bill and its path over land were both driven by large-scale atmospheric forcing. Maintenance of the storm over land was aided by above normal latent heat fluxes both near the storm's primary circulation and upstream. The upstream enhancement was driven by abundant soil moisture and solar radiation, both of which were maximized by the storm's movement. As such, the storm's movement, driven by the large-scale atmospheric circulation, produced a favorable environment upstream for large values of ET along the storm's inflow. In other words, the large-scale environment also produced favorable conditions for enhanced fluxes of moisture from the land surface into the storm's inflow. This combination of large-scale forcing and land-atmosphere interactions aided in the maintenance of TS Bill for several days over land. Further, the above analysis also demonstrated the importance of surface fluxes upstream during an extreme event and suggested that even advected quantities may be connected to soil moisture upstream.

6.3 Sensitivity of the PBL to surface fluxes during flash drought

The final analysis used knowledge gained from the preceding analyses to devise an experiment that would best determine the role of the land surface on the evolution of the 2012 flash drought and drought over the Southern Great Plains. A modified application of the CTP-HIlow framework previously demonstrated a pre-conditioning of the atmosphere for drought during 2012 (Basara et al. 2019), but a more detailed framework was necessary to capture the daytime evolution of the PBL during this period. Thus, the modified mixing diagram framework was used. Further, the impact of advected quantities via the

TS Bill analysis illustrated that advection was critical and implemented in the mixing diagram framework analysis for the 2012 case. Coupled simulations using the NASA Unified Weather Research and Forecasting (NU-WRF) model and Land Information Systems (LIS) were utilized for simulations spanning 11 days with minimal synoptic influence during May, June and July of 2012.

The prescription of wet soils across the study domain resulted in reduced PBL warming, drying, and reduced evaporative demand even during the height of drought development. Moreover, the control simulations, simulations over dry soils and simulations over wet soils all displayed similar moisture and temperature profiles above the PBL indicating the same large-scale atmospheric forcing for drought, but a sensitivity of evaporative demand to surface fluxes manifesting through differences in daytime PBL temperature and moisture evolution. Thus, if wet soils were present, the conditions would have likely modulated the magnitude and intensity of drought in the region. Further, if the event were driven by atmospheric aridity alone, increased ET would have been observed over wet soils but the concurrent reduction in PET would not.

6.4 Overlap between tropical cyclone and drought analyses

(Wu and Dirmeyer 2020) showed that drought demise is often associated with atmospheric rivers and in the southeastern United States and via precipitation from landfalling tropical cyclones. Had a tropical cyclone (TC) such as TS Bill made landfall three years earlier in 2012 and traveled sufficiently inland, it may have produced widespread moistening of soils in the Southern Great Plains. If the same background same background atmospheric conditions favorable for drought immediately returned after the hypothetical TC landfall, land-atmosphere feedbacks over moistened soils would have reduced evaporative demand within the PBL via moistening through increased ET. Eventually soils would once again dry out, due to sustained ET, but this would occur less rapidly than if evaporative demand were insensitive to soil moisture.

At the same time, the results from Chapter 4 demonstrate the if a tropical cyclone were to make landfall during 2012, dry soils would have contributed to its demise well before it could travel far enough inland to produce substantial rainfall over Oklahoma. Thus, even if a tropical cyclone identical to Tropical Storm Bill made landfall in 2012, the antecedent dry soils along its path would have interacted with larger scale forcing (the TC) to perpetuate drought by suppressing the TC's overland maintenance and/or reintensification.

6.5 Summary of Key Findings

Chapters 2 and 3 did not directly address the contribution of land-atmosphere feedbacks toward extreme precipitation event evolution, however they provided critical knowledge that optimized the methods for analyzing covariance and coupling during an extreme event. The ability to obtain vertical profiles of moisture and temperature at high temporal resolution allows for improved quantification of PBL moisture and energy budgets by considering the qualities of the mixed layer itself rather than simply using 2 m observations within the surface layer. This not only supports future studies that will improve the understanding of land-atmosphere coupling itself, but such observations can be used to improve operational and research-based models and model parameterizations of the land surface and the PBL. These improvements could also result in better simulations of the PBL during extreme events such as those analyzed in Chapters 4 and 5.

In summary, Chapters 4 and 5 directly addressed the stated hypothesis and provided these key results:

1. Chapter 4 showed that land surface fluxes upstream can impact advected quantities, and thus moisture and energy budgets within a location of interest that impact extreme events.

2. The background atmospheric state during TS Bill propagating along a path which allowed for greater fluxes of moisture along its inflow by neither limiting incoming

solar radiation or soil moisture along inflow parcel paths. These analyses presented a methodology for distinguishing between large-scale and land surface contributions toward an extreme event. The relative importance of each factor was demonstrated through comparison with other landfalling tropical cyclones which decayed rapidly.

3. Soil moisture influenced the relative humidity of the PBL over the Southern Great Plains during the 2012 flash drought and drought maintenance. Wet soil simulations show that moister soils would have contributed to lower PBL heights, an overall moister and cooler PBL, and lower evaporative demand that would have had a moderating effect on drought intensification.

4. Atmospheric profiles were similar across DRY, CTRL and WET simulations for the same day and displayed the greatest differences within the PBL during the daytime indicating that moisture and energy budgets of the PBL were largely sensitive to the partitioning of surface fluxes.

5. The more moist PBL generated by WET simulations was related to enhanced ET which also reduced PET. Had PET been insensitive to surface fluxes, PET would have been the same across DRY, CTRL and WET, simulations and only ET would have differed among them.

Future work should also consider idealized simulations during TS Bill to better quantify the sensitivity of the storm to surface fluxes. Further, sample size was a common limitation for each of the case studies. Even so, the novelty of this research lies in the methods of each analysis and the applicability of those methods toward future work which can include greater sample size. Further, these analyses build upon work by Schumacher et al. (2019) to consider a more Lagrangian approach to land-atmosphere interactions in which local and non-local land surface fluxes are considered as a potential influence on the nature of the PBL. This was completed by analyzing surface fluxes along inflow trajectories for TS Bill and by incorporating advective contributions into analysis of PBL moisture and

energy budgets in Chapter 5. The atmosphere does not operate within an isolated column, and as such future land-atmosphere coupling research will benefit from considering a more Lagrangian approach.

While this research primarily focused on land-atmosphere interactions and their contributions to extreme hydrometeorological events in the United States Great Plains, the novel methods introduced in these studies are applicable to studies in other regions of the world. This includes semi-arid regions, such as the African Sahel, and the Indian monsoon region, which display a greater sensitivity of evapotranspiration to changes in soil moisture (Guo et al. 2006; Koster et al. 2006; Wei et al. 2016; Basara and Christian 2018). In the case of the latter, changes in land use and land cover may influence the timing and quantity of rainfall associated with the monsoon circulation (Niyogi et al. 2010; Kishtawal et al. 2013; Niyogi et al. 2020).Moreover, the region's agriculture relies on monsoon rainfall, but an increase in number of dry and wet extremes has led to greater socioeconomic vulnerability (Singh et al. 2014; Swami et al. 2018). The modified mixing diagram framework introduced in Chapter 3 and applied in Chapter 5, could serve as a valuable tool for subseasonal to seasonal predictability of the timing of monsoon rainfall onset. Even though the framework was applied toward understanding drought/flash drought, it revealed the relative sensitivity of the PBL, PET and ET to terrestrial moisture even when the larger scale atmospheric state was constant. As land-sea temperature differences play a role in the monsoon circulation, this framework could be used to better quantify the relative role of the land surface on PBL development in relation to a given background atmospheric state prior to and during monsoon onset. The framework's flexibility to observational and gridded datasets enable retrospective analyses and real time monitoring that could further enhance subseasonal to seasonal predictability. Methods used to analyze Tropical Storm Bill's overland reintensification may also have predictive utility once monsoon rainfall has commenced. Much like landfalling tropical cyclones, the intensity of rainfall associated with landfalling monsoon

depressions is sensitive to antecedent land surface conditions. Therefore, monsoon rainfall intensity predictions at the subseasonal to seasonal scale could be aided by methods introduced in the analysis of Tropical Storm Bill's overland reintensification. Moisture advection feedbacks are thought to play a role in the monsoon circulation (Levermann et al. 2009; Pathak and Ghosh 2019), thus along trajectory analysis of surface fluxes may provide further insight into the role of upstream terrestrial and/or oceanic moisture fluxes in maintaining these moisture advection feedbacks. This is just one example of how the methods introduced in this work can have global impacts by increasing subseasonal to seasonal predictability of precipitation extremes in regions where precipitation variability is synonymous with socioeconomic variability. As such, the novel contributions of this research to the science extend well beyond the results presented, and have enabled numerous opportunities for ongoing and future research utilizing the tools and methods presented in this dissertation.

Bibliography

Andersen, T. K., D. E. Radcliffe, and J. M. Shepherd, 2013: Quantifying surface energy fluxes in the vicinity of inland-tracking tropical cyclones. *J. Appl. Meteor. Climatol.*, **52 (12)**, 2797–2808.

Andersen, T. K., and J. M. Shepherd, 2014: A global spatiotemporal analysis of inland tropical cyclone maintenance or intensification. *Int. J. Climatol.*, **34 (2)**, 391–402.

Arndt, D. S., J. B. Basara, R. A. McPherson, B. G. Illston, G. D. McManus, and D. B. Demko, 2009: Observations of the overland reintensification of tropical storm erin (2007). *Bull. Amer. Meteor. Soc.*, **90 (8)**, 1079–1094.

Atlas, R., N. Wolfson, and J. Terry, 1993: The effect of sst and soil moisture anomalies on gla model simulations of the 1988 us summer drought. *J. Climate*, **6 (11)**, 2034–2048.

Bakhshaii, A., and R. Stull, 01 Jan. 2013: Saturated pseudoadiabats—a noniterative approximation. *J. Appl. Meteor. Climatol.*, **52 (1)**, 5 – 15, doi:10.1175/JAMC-D-12-062.1, URL https://journals.ametsoc.org/view/journals/apme/52/1/jamc-d-12-062.1.xml.

Bakhvalov, N., 2001: Courant–friedrichs–lewy condition, encyclopedia of mathematics. EMS Press, urlhttps://encyclopediaofmath.org/wiki/Courant-Friedrichs-Lewy$_condition$.

Basara, J. B., and J. I. Christian, 2018: Seasonal and interannual variability of land–atmosphere coupling across the southern great plains of north america using the north american regional reanalysis. *Int. J. Climatol.*, **38 (2)**, 964–978.

Basara, J. B., J. I. Christian, R. A. Wakefield, J. A. Otkin, E. H. Hunt, and D. P. Brown, 2019: The evolution, propagation, and spread of flash drought in the central united states during 2012. *Environmental Research Letters*, **14 (8)**, 084 025.

Basara, J. B., and K. C. Crawford, 2002: Linear relationships between root-zone soil moisture and atmospheric processes in the planetary boundary layer. *J. Geophys. Res.*, **107 (D15)**, ACL–10.

Basara, J. B., J. N. Maybourn, C. M. Peirano, J. E. Tate, P. J. Brown, J. D. Hoey, and B. R. Smith, 2013: Drought and associated impacts in the great plains of the united states—a review.

Benson, D. O., and P. A. Dirmeyer, 2021: Characterizing the relationship between temperature and soil moisture extremes and their role in the exacerbation of heat waves over the contiguous united states. *Journal of Climate*, **34 (6)**, 2175–2187.

Berg, R., 2015: Tropical cyclone report, tropical storm bill, 16-18 june 2015. *Miami, FL: National Hurricane Center*.

Betts, A., 1992: Possible relation between land surface feedback and the post-landfall structure of monsoon depressions. *J. Geophys. Res.*, **97 (D17)**, 18 523–18 531.

Blumberg, W., D. Turner, U. Löhnert, and S. Castleberry, 2015: Ground-based temperature and humidity profiling using spectral infrared and microwave observations. part ii: Actual retrieval performance in clear-sky and cloudy conditions. *J. Appl. Meteor. Climatol.*, **54 (11)**, 2305–2319.

Blumberg, W., T. Wagner, D. Turner, and J. Correia Jr, 2017: Quantifying the accuracy and uncertainty of diurnal thermodynamic profiles and convection indices derived from the atmospheric emitted radiance interferometer. *J. Appl. Meteor. Climatol.*, **56 (10)**, 2747–2766.

Board, S. S., E. National Academies of Sciences, Medicine, and Coauthors, 2017: *Thriving on our changing planet: A decadal strategy for Earth observation from space*. National Academies Press.

Bozeman, M. L., D. Niyogi, S. Gopalakrishnan, F. D. Marks, X. Zhang, and V. Tallapragada, 2012: An hwrf-based ensemble assessment of the land surface feedback on the post-landfall intensification of tropical storm fay (2008). *Nat. Hazards Rev.*, **63 (3)**, 1543–1571.

Bracken, C., B. Rajagopalan, M. Alexander, and S. Gangopadhyay, 2015: Spatial variability of seasonal extreme precipitation in the western united states. *J. Geophys. Res.*, **120 (10)**, 4522–4533.

Branch, O., and V. Wulfmeyer, 2019: Deliberate enhancement of rainfall using desert plantations. *Proc. Natl. Acad. Sci. (USA)*, **116 (38)**, 18 841–18 847, doi:10.1073/pnas.1904754116.

Brauer, N., J. B. Basara, P.-E. Kirstetter, R. A. Wakefield, C. R. Homeyer, J. Yoo, J. M. Shepherd, and J. A. Santanello, 2021: The inland maintenance and re-intensification of tropical storm bill (2015) part 2: Precipitation microphysics. *J. Hydrometeor.*, **In press**.

Center, E. M., 2003: The gfs atmospheric model. *National Centers for Environmental Prediction Office Note*, **442**, 14.

Chang, H., D. Niyogi, A. Kumar, C. Kishtawal, J. Dudhia, F. Chen, U. Mohanty, and M. Shepherd, 2009: Possible relation between land surface feedback and the post-landfall structure of monsoon depressions. *Geophys. Res. Lett.*, **36 (15)**.

Chaouch, N., M. Temimi, M. Weston, and H. Ghedira, 2017: Sensitivity of the meteorological model wrf-arw to planetary boundary layer schemes during fog conditions in a coastal arid region. *Atmospheric Research*, **187**, 106–127.

Christian, J. I., J. B. Basara, J. A. Otkin, E. D. Hunt, R. A. Wakefield, P. X. Flanagan, and X. Xiao, 2019: A methodology for flash drought identification: Application of flash drought frequency across the united states. *Journal of Hydrometeorology*, **20 (5)**, 833–846.

Cook, D. R., and R. C. Sullivan, 2020: Eddy correlation flux measurement system (ecor) instrument handbook. Tech. rep., DOE Office of Science Atmospheric Radiation Measurement (ARM) Program ....

Courant, R., K. Friedrichs, and H. Lewy, 1928: Über die partiellen differenzengleichungen der mathematischen physik. *Mathematische annalen*, **100 (1)**, 32–74.

Dastoor, A., and T. Krishnamurti, 1991: The landfall and structure of a tropical cyclone: The sensitivity of model predictions to soil moisture parameterizations. *Bound.-Layer Meteorol.*, **55 (4)**, 345–380.

DeAngelis, A. M., H. Wang, R. D. Koster, S. D. Schubert, Y. Chang, and J. Marshak, 2020: Prediction skill of the 2012 us great plains flash drought in subseasonal experiment (subx) models. *J. Climate*, **33 (14)**, 6229–6253.

Dirmeyer, P. A., 2001: An evaluation of the strength of land–atmosphere coupling. *J. Hydrometeor.*, **2 (4)**, 329–344.

Dirmeyer, P. A., 2006: The hydrologic feedback pathway for land–climate coupling. *J. Hydrometeor.*, **7 (5)**, 857–867.

Dirmeyer, P. A., and S. Halder, 2016: Sensitivity of numerical weather forecasts to initial soil moisture variations in cfsv2. *Wea. Forecasting*, **31 (6)**, 1973–1983.

Dong, X., and Coauthors, 2011: Investigation of the 2006 drought and 2007 flood extremes at the southern great plains through an integrative analysis of observations. *J. Geophys. Res.*, **116 (D3)**.

Edwards, R., 2010: Tropical cyclone tornado records for the modernized national weather service era. *Preprints, 25th Conf. on Severe Local Storms, Denver, CO, Amer. Meteor. Soc. P*, Vol. 2.

Ek, M., and A. Holtslag, 2004: Influence of soil moisture on boundary layer cloud development. *J. Hydrometeor.*, **5 (1)**, 86–99.

Ek, M., and L. Mahrt, 1994: Daytime evolution of relative humidity at the boundary layer top. *Mon. Wea. Rev.*, **122 (12)**, 2709–2721.

Ek, M., K. Mitchell, Y. Lin, E. Rogers, P. Grunmann, V. Koren, G. Gayno, and J. Tarpley, 2003: Implementation of noah land surface model advances in the national centers for environmental prediction operational mesoscale eta model. *J. Geophys. Res.*, **108 (D22)**.

Emanuel, K., J. Callaghan, and P. Otto, 2008: A hypothesis for the redevelopment of warm-core cyclones over northern australia. *Mon. Wea. Rev.*, **136 (10)**, 3863–3872.

Emanuel, K., C. DesAutels, C. Holloway, and R. Korty, 2004: Environmental control of tropical cyclone intensity. *J. Atmos. Sci.*, **61 (7)**, 843 – 858, doi:10.1175/1520-0469(2004)061⟨0843:ECOTCI⟩2.0.CO;2.

Entin, J. K., A. Robock, K. Y. Vinnikov, S. E. Hollinger, S. Liu, and A. Namkhai, 2000: Temporal and spatial scales of observed soil moisture variations in the extratropics. *J. Geophys. Res.*, **105 (D9)**, 11 865–11 877.

Erfanian, A., and R. Fu, 2019: The role of spring dry zonal advection in summer drought onset over the us great plains. *Atmos. Chem. Phys.*, **19 (24)**, 15 199–15 216.

Erlingis, J. M., and A. P. Barros, 2014: A study of the role of daytime land–atmosphere interactions on nocturnal convective activity in the southern great plains during clasic. *J. Hydrometeor.*, **15 (5)**, 1932–1953.

Erlingis, J. M., J. J. Gourley, and J. B. Basara, 2019a: Diagnosing moisture sources for flash floods in the united states. part i: Kinematic trajectories. *J. Hydrometeor.*, **20 (8)**, 1495–1509.

Erlingis, J. M., J. J. Gourley, and J. B. Basara, 2019b: Diagnosing moisture sources for flash floods in the united states. part ii: Terrestrial and oceanic sources of moisture. *J. Hydrometeor.*, **20 (8)**, 1511–1531.

Evans, C., R. S. Schumacher, and T. J. Galarneau Jr, 2011: Sensitivity in the overland reintensification of tropical cyclone erin (2007) to near-surface soil moisture characteristics. *Mon. Wea. Rev.*, **139 (12)**, 3848–3870.

Feltz, W., W. Smith, H. B. Howell, R. Knuteson, H. Woolf, and H. Revercomb, 2003: Near-continuous profiling of temperature, moisture, and atmospheric stability using the atmospheric emitted radiance interferometer (aeri). *J. Appl. Meteor.*, **42 (5)**, 584–597.

Feltz, W. F., W. L. Smith, R. O. Knuteson, H. E. Revercomb, H. M. Woolf, and H. B. Howell, 1998: Meteorological applications of temperature and water vapor retrievals from the ground-based atmospheric emitted radiance interferometer (aeri). *J. Appl. Meteor.*, **37 (9)**, 857–875.

Ferguson, C. R., and E. F. Wood, 2011: Observed land–atmosphere coupling from satellite remote sensing and reanalysis. *J. Hydrometeor.*, **12 (6)**, 1221–1254.

Fernando, D. N., and Coauthors, 2016: What caused the spring intensification and winter demise of the 2011 drought over texas? *Climate Dyn.*, **47 (9)**, 3077–3090.

Findell, K. L., and E. A. Eltahir, 2003a: Atmospheric controls on soil moisture–boundary layer interactions. part i: Framework development. *J. Hydrometeor.*, **4 (3)**, 552–569.

Findell, K. L., and E. A. Eltahir, 2003b: Atmospheric controls on soil moisture–boundary layer interactions. part ii: Feedbacks within the continental united states. *J. Hydrometeor.*, **4 (3)**, 570–583.

Flanagan, P. X., J. B. Basara, B. G. Illston, and J. A. Otkin, 2017: The effect of the dry line and convective initiation on drought evolution over oklahoma during the 2011 drought. *Adv. Meteorol.*, **2017**.

Frank, W. M., 1977: The structure and energetics of the tropical cyclone i. storm structure. *Mon. Wea. Rev.*, **105 (9)**, 1119–1135.

Fritz, C., and Z. Wang, 2013: A numerical study of the impacts of dry air on tropical cyclone formation: A development case and a nondevelopment case. *J. Atmos. Sci.*, **70 (1)**, 91–111.

Frye, J. D., and T. L. Mote, 2010: Convection initiation along soil moisture boundaries in the southern great plains. *Mon. Wea. Rev.*, **138 (4)**, 1140–1151.

Fujiwara, K., R. Kawamura, H. Hirata, T. Kawano, M. Kato, and T. Shinoda, 2017: A positive feedback process between tropical cyclone intensity and the moisture conveyor belt assessed with lagrangian diagnostics. *J. Geophys. Res.*, **122 (23)**, 12–502.

Guo, Z., and Coauthors, 2006: Glace: the global land–atmosphere coupling experiment. part ii: analysis. *Journal of Hydrometeorology*, **7 (4)**, 611–625.

Gustafsson, M., D. Rayner, and D. Chen, 2010: Extreme rainfall events in southern sweden: Where does the moisture come from? *Tellus A.*, **62 (5)**, 605–616.

Hart, R. E., and J. L. Evans, 2001: A climatology of the extratropical transition of atlantic tropical cyclones. *J. Climate*, **14 (4)**, 546–564.

Herrera-Estrada, J. E., J. A. Martinez, F. Dominguez, K. L. Findell, E. F. Wood, and J. Sheffield, 2019: Reduced moisture transport linked to drought propagation across north america. *Geophys. Res. Lett.*, **46 (10)**, 5243–5253.

Hoerling, M., J. Eischeid, A. Kumar, R. Leung, A. Mariotti, K. Mo, S. Schubert, and R. Seager, 2014: Causes and predictability of the 2012 great plains drought. *Bull. Amer. Meteor. Soc.*, **95 (2)**, 269–282.

Hong, S.-Y., and E. Kalnay, 2000: Role of sea surface temperature and soil-moisture feedback in the 1998 oklahoma–texas drought. *Nature*, **408 (6814)**, 842–844.

Irion, F. W., and Coauthors, 2018: Single-footprint retrievals of temperature, water vapor and cloud properties from airs. *Atmos. Meas. Tech.*, **11 (2)**, 971–995.

Jach, L., K. Warrach-Sagi, J. Ingwersen, E. Kaas, and V. Wulfmeyer, 2020: Land cover impacts on land-atmosphere coupling strength in climate simulations with wrf over europe. *J. Geophys. Res.*, **125 (18)**, e2019JD031 989.

Jana, S., B. Rajagopalan, M. A. Alexander, and A. J. Ray, 2018: Understanding the dominant sources and tracks of moisture for summer rainfall in the southwest united states. *J. Geophys. Res.*, **123 (10)**, 4850–4870.

Jones, S. C., and Coauthors, 2003: The extratropical transition of tropical cyclones: Forecast challenges, current understanding, and future directions. *Wea. Forecasting*, **18 (6)**, 1052–1092.

Kellner, O., D. Niyogi, M. Lei, and A. Kumar, 2012: The role of anomalous soil moisture on the inland reintensification of tropical storm erin (2007). *Nat. Hazards Rev.*, **63 (3)**, 1573–1600.

Kishtawal, C., D. Niyogi, B. Rajagopalan, M. Rajeevan, N. Jaiswal, and U. Mohanty, 2013: Enhancement of inland penetration of monsoon depressions in the bay of bengal due to prestorm ground wetness. *Water Resour. Res*, **49 (6)**, 3589–3600.

Kishtawal, C. M., D. Niyogi, A. Kumar, M. L. Bozeman, and O. Kellner, 2012: Sensitivity of inland decay of north atlantic tropical cyclones to soil parameters. *Nat. Hazards Rev.*, **63 (3)**, 1527–1542.

Knuteson, R., and Coauthors, 2004a: Atmospheric emitted radiance interferometer. part i: Instrument design. *J. Atmos. Oceanic Technol.*, **21 (12)**, 1763–1776.

Knuteson, R., and Coauthors, 2004b: Atmospheric emitted radiance interferometer. part ii: Instrument performance. *J. Atmos. Oceanic Technol.*, **21 (12)**, 1777–1789.

Koster, R., and Coauthors, 2011: The second phase of the global land–atmosphere coupling experiment: Soil moisture contributions to subseasonal forecast skill. *J. Hydrometeor.*, **12 (5)**, 805–822.

Koster, R. D., Y. Chang, and S. D. Schubert, 2014: A mechanism for land–atmosphere feedback involving planetary wave structures. *J. Climate*, **27 (24)**, 9290–9301.

Koster, R. D., Y. Chang, H. Wang, and S. D. Schubert, 2016: Impacts of local soil moisture anomalies on the atmospheric circulation and on remote surface meteorological fields during boreal summer: A comprehensive analysis over north america. *J. Climate*, **29 (20)**, 7345–7364.

Koster, R. D., and M. J. Suarez, 2001: Soil moisture memory in climate models. *J. Hydrometeor.*, **2 (6)**, 558–570.

Koster, R. D., and Coauthors, 2004: Regions of strong coupling between soil moisture and precipitation. *Science*, **305 (5687)**, 1138–1140.

Koster, R. D., and Coauthors, 2006: Glace: the global land–atmosphere coupling experiment. part i: overview. *Journal of Hydrometeorology*, **7 (4)**, 590–610.

Kumar, S. V., and Coauthors, 2006: Land information system: An interoperable framework for high resolution land surface modeling. *Environ. Model. Softw.*, **21 (10)**, 1402–1415.

Läderach, A., and H. Sodemann, 2016: A revised picture of the atmospheric moisture residence time. *Geophys. Res. Lett.*, **43 (2)**, 924–933.

Landsea, C. W., and J. L. Franklin, 2013: Atlantic hurricane database uncertainty and presentation of a new database format. *Mon. Wea. Rev.*, **141 (10)**, 3576–3592.

Levermann, A., J. Schewe, V. Petoukhov, and H. Held, 2009: Basic mechanism for abrupt monsoon transitions. *Proc. Natl. Acad. Sci. (USA)*, **106 (49)**, 20 572–20 577.

Lothon, M., and Coauthors, 2014: The bllast field experiment: boundary-layer late afternoon and sunset turbulence. *Atmospheric chemistry and physics*, **14 (20)**, 10 931–10 960.

May, R. M., S. C. Arms, P. Marsh, E. Bruning, J. R. Leeman, K. Goebbert, J. E. Thielen, and Z. S. Bruick, 2020: Metpy: A Python package for meteorological data. Unidata, urlhttps://github.com/Unidata/MetPy, doi:10.5065/D6WW7G29.

McPherson, R. A., D. J. Stensrud, and K. C. Crawford, 2004: The impact of oklahoma's winter wheat belt on the mesoscale environment. *Mon. Wea. Rev.*, **132 (2)**, 405–421.

Mesinger, F., and Coauthors, 2006: North american regional reanalysis. *Bull. Amer. Meteor. Soc.*, **87 (3)**, 343–360.

Milovac, J., K. Warrach-Sagi, A. Behrendt, F. Späth, J. Ingwersen, and V. Wulfmeyer, 2016: Investigation of pbl schemes combining the wrf model simulations with scanning water vapor differential absorption lidar measurements. *J. Geophys. Res.*, **121 (2)**, 624–649.

Miralles, D. G., P. Gentine, S. I. Seneviratne, and A. J. Teuling, 2019: Land–atmospheric feedbacks during droughts and heatwaves: state of the science and current challenges. *Annals of the New York Academy of Sciences*, **1436 (1)**, 19.

Miralles, D. G., A. J. Teuling, C. C. Van Heerwaarden, and J. V.-G. De Arellano, 2014: Mega-heatwave temperatures due to combined soil desiccation and atmospheric heat accumulation. *Nat. Geosci.*, **7 (5)**, 345–349.

Molina, M. J., and J. T. Allen, 2019: On the moisture origins of tornadic thunderstorms. *J. Climate*, **32 (14)**, 4321–4346.

Molina, M. J., and J. T. Allen, 2020: Regionally-stratified tornadoes: Moisture source physical reasoning and climate trends. *Weather Clim. Extremes*, **28**, 100 244.

Monteverdi, J. P., and R. Edwards, 2010: The redevelopment of a warm-core structure in erin: A case of inland tropical storm formation. *Electron. J. Severe. Storms Meteor.*, **5 (6)**.

Nair, U. S., and Coauthors, 2019: Influence of land cover and soil moisture based brown ocean effect on an extreme rainfall event from a louisiana gulf coast tropical system. *Sci. Rep*, **9 (1)**, 1–10.

Namias, J., 1983: Some causes of united states drought. *J. Appl. Meteor. Climatol.*, **22 (1)**, 30–39.

Namias, J., 1988: The 1988 summer drought over the great plains: A classic example of air-sea-land interaction. *Trans. Amer. Geophys. Union*, **69**, 1067.

Newsom, R., D. Turner, R. Lehtinen, C. Münkel, J. Kallio, and R. Roininen, 2020: Evaluation of a compact broadband differential absorption lidar for routine water vapor profiling in the atmospheric boundary layer. *J. Atmos. Oceanic Technol.*, **37 (1)**, 47–65.

Niyogi, D., C. Kishtawal, S. Tripathi, and R. S. Govindaraju, 2010: Observational evidence that agricultural intensification and land use change may be reducing the indian summer monsoon rainfall. *Water Resour. Res*, **46 (3)**.

Niyogi, D., K. K. Osuri, N. Busireddy, and R. Nadimpalli, 2020: Timing of rainfall occurrence altered by urban sprawl. *Urban Clim.*, **33**, 100 643.

Pal, J. S., and E. A. Eltahir, 2003: A feedback mechanism between soil-moisture distribution and storm tracks. *Quart. J. Roy. Meteor. Soc.*, **129 (592)**, 2279–2297.

Pathak, A., and S. Ghosh, 2019: Land–atmosphere interactions in indian monsoon at subseasonal to seasonal scale. *Hydrology in a Changing World*, Springer, 139–152.

Peters-Lidard, C. D., and Coauthors, 2007: High-performance earth system modeling with nasa/gsfc's land information system. *Innov. Syst. Softw. Eng.*, **3 (3)**, 157–165.

Peters-Lidard, C. D., and Coauthors, 2015: Integrated modeling of aerosol, cloud, precipitation and land processes at satellite-resolved scales. *Environ. Model. Softw.*, **67**, 149–159.

Phillips, T. J., and S. A. Klein, 2014: Land-atmosphere coupling manifested in warm-season observations on the us southern great plains. *J. Geophys. Res.*, **119 (2)**, 509–528.

Ritsche, M., 2011: Arm surface meteorology systems instrument handbook. Tech. rep., Tech. rep., Office of Scientific and Technical Information (OSTI), https ....

Rodgers, C. D., 2000: *Inverse methods for atmospheric sounding: theory and practice*, Vol. 2. World scientific.

Roundy, J. K., C. R. Ferguson, and E. F. Wood, 2013: Temporal variability of land–atmosphere coupling and its implications for drought over the southeast united states. *J. Hydrometeor.*, **14 (2)**, 622–635.

Roundy, J. K., and J. A. Santanello, 2017: Utility of satellite remote sensing for land–atmosphere coupling and drought metrics. *J. Hydrometeor.*, **18 (3)**, 863–877.

Saini, R., G. Wang, and J. S. Pal, 2016: Role of soil moisture feedback in the development of extreme summer drought and flood in the united states. *J. Hydrometeor.*, **17 (8)**, 2191–2207.

Santanello, J., C. Ferguson, M. Ek, P. Dirmeyer, O. Tuinenburg, C. Jacobs, C. van Heerwaarden, and B. Findell, 2011: Local land-atmosphere coupling (loco) research: Status and results. *GEWEX news*, **21 (4)**, 7–9.

Santanello, J. A., C. D. Peters-Lidard, S. V. Kumar, C. Alonge, and W.-K. Tao, 2009: A modeling and observational framework for diagnosing local land–atmosphere coupling on diurnal time scales. *JHM*, **10 (3)**, 577–599.

Santanello Jr, J. A., M. A. Friedl, and M. B. Ek, 2007: Convective planetary boundary layer interactions with the land surface at diurnal time scales: Diagnostics and feedbacks. *J. Hydrometeor.*, **8 (5)**, 1082–1097.

Santanello Jr, J. A., M. A. Friedl, and W. P. Kustas, 2005: An empirical investigation of convective planetary boundary layer evolution and its relationship with the land surface. *J. Appl. Meteor.*, **44 (6)**, 917–932.

Santanello Jr, J. A., P. Lawston, S. Kumar, and E. Dennis, 2019: Understanding the impacts of soil moisture initial conditions on nwp in the context of land–atmosphere coupling. *J. Hydrometeor.*, **20 (5)**, 793–819.

Santanello Jr, J. A., C. D. Peters-Lidard, and S. V. Kumar, 2011: Diagnosing the sensitivity of local land–atmosphere coupling via the soil moisture–boundary layer interaction. *J. Hydrometeor.*, **12 (5)**, 766–786.

Santanello Jr, J. A., J. Roundy, and P. A. Dirmeyer, 2015: Quantifying the land–atmosphere coupling behavior in modern reanalysis products over the us southern great plains. *J. Climate*, **28 (14)**, 5813–5829.

Santanello Jr, J. A., and Coauthors, 2018: Land–atmosphere interactions: The loco perspective. *Bull. Amer. Meteor. Soc.*, **99 (6)**, 1253–1272.

Schubert, S., and Coauthors, 2009: A us clivar project to assess and compare the responses of global climate models to drought-related sst forcing patterns: Overview and results. *J. Climate*, **22 (19)**, 5251–5272.

Schubert, S. D., M. J. Suarez, P. J. Pegion, R. D. Koster, and J. T. Bacmeister, 2004a: Causes of long-term drought in the us great plains. *J. Climate*, **17 (3)**, 485–503.

Schubert, S. D., M. J. Suarez, P. J. Pegion, R. D. Koster, and J. T. Bacmeister, 2008: Potential predictability of long-term drought and pluvial conditions in the us great plains. *J. Climate*, **21 (4)**, 802–816.

Schumacher, D. L., J. Keune, C. C. Van Heerwaarden, J. V.-G. de Arellano, A. J. Teuling, and D. G. Miralles, 2019: Amplification of mega-heatwaves through heat torrents fuelled by upwind drought. *Nature Geoscience*, **12 (9)**, 712–717.

Seager, R., and M. Hoerling, 2014: Atmosphere and ocean origins of north american droughts. *J. Climate*, **27 (12)**, 4581–4606.

Seager, R., Y. Kushnir, C. Herweijer, N. Naik, and J. Velez, 2005: Modeling of tropical forcing of persistent droughts and pluvials over western north america: 1856–2000. *J. Climate*, **18 (19)**, 4065–4088.

Seager, R., N. Lis, J. Feldman, M. Ting, A. P. Williams, J. Nakamura, H. Liu, and N. Henderson, 2018: Whither the 100th meridian? the once and future physical and human geography of america's arid–humid divide. part i: The story so far. *Earth Interact.*, **22 (5)**, 1–22.

Seager, R., J. Nakamura, and M. Ting, 2019: Mechanisms of seasonal soil moisture drought onset and termination in the southern great plains. *J. Hydrometeor.*, **20 (4)**, 751–771.

Seneviratne, S. I., D. Lüthi, M. Litschi, and C. Schär, 2006: Land–atmosphere coupling and climate change in europe. *Nature*, **443 (7108)**, 205–209.

Shen, W., I. Ginis, and R. E. Tuleya, 2002: A numerical investigation of land surface water on landfalling hurricanes. *J. Atmos. Sci.*, **59 (4)**, 789–802.

Singh, D., M. Tsiang, B. Rajaratnam, and N. S. Diffenbaugh, 2014: Observed changes in extreme wet and dry spells during the south asian summer monsoon season. *Nat. Clim. Change*, **4 (6)**, 456–461.

Sisterson, D., R. Peppler, T. Cress, P. Lamb, and D. Turner, 2016: The arm southern great plains (sgp) site. *Meteor. Monogr.*, **57**, 6–1.

Smith, W. L., W. F. Feltz, R. O. Knuteson, H. E. Revercomb, H. M. Woolf, and H. B. Howell, 1999: The retrieval of planetary boundary layer structure using ground-based infrared spectral radiance measurements. *J. Atmos. Oceanic Technol.*, **16 (3)**, 323–333.

Song, H.-J., C. R. Ferguson, and J. K. Roundy, 2016: Land–atmosphere coupling at the southern great plains atmospheric radiation measurement (arm) field site and its role in anomalous afternoon peak precipitation. *J. Hydrometeor.*, **17 (2)**, 541–556.

Stein, A., R. R. Draxler, G. D. Rolph, B. J. Stunder, M. Cohen, and F. Ngan, 2015: Noaa's hysplit atmospheric transport and dispersion modeling system. *Bull. Amer. Meteor. Soc.*, **96 (12)**, 2059–2077.

Stewart, S., 2016: National hurricane center annual summary. *2015 Atlantic Hurricane Season*.

Stull, R. B., 1988: *An introduction to boundary layer meteorology*, Vol. 13. Springer Science & Business Media.

Su, H., and R. E. Dickinson, 2017: On the spatial gradient of soil moisture–precipitation feedback strength in the april 2011 drought in the southern great plains. *J. Climate*, **30 (3)**, 829–848.

Svoboda, M., and Coauthors, 2002: The drought monitor. *Bull. Amer. Meteor. Soc.*, **83 (8)**, 1181–1190.

Swami, D., P. Dave, and D. Parthasarathy, 2018: Agricultural susceptibility to monsoon variability: A district level analysis of maharashtra, india. *Sci. Total Environ.*, **619**, 559–577.

Tang, Q., S. Xie, Y. Zhang, T. J. Phillips, J. A. Santanello, D. R. Cook, L. D. Riihimaki, and K. L. Gaustad, 2018: Heterogeneity in warm-season land-atmosphere coupling over the us southern great plains. *J. Geophys. Res.*, **123 (15)**, 7867–7882.

Taylor, C. M., A. Gounou, F. Guichard, P. P. Harris, R. J. Ellis, F. Couvreux, and M. De Kauwe, 2011: Frequency of sahelian storm initiation enhanced over mesoscale soil-moisture patterns. *Nature Geoscience*, **4 (7)**, 430–433.

Taylor, C. M., D. J. Parker, and P. P. Harris, 2007: An observational case study of mesoscale atmospheric circulations induced by soil moisture. *Geophys. Res. Lett.*, **34 (15)**.

Trenberth, K. E., G. W. Branstator, and P. A. Arkin, 1988: Origins of the 1988 north american drought. *Science*, **242 (4886)**, 1640–1645.

Trenberth, K. E., and C. J. Guillemot, 1996: Physical processes involved in the 1988 drought and 1993 floods in north america. *J. Climate*, **9 (6)**, 1288–1298.

Tuleya, R. E., 1994: Tropical storm development and decay: Sensitivity to surface boundary conditions. *Mon. Wea. Rev.*, **122 (2)**, 291–304.

Tuleya, R. E., and Y. Kurihara, 1978: A numerical simulation of the landfall of tropical cyclones. *J. Atmos. Sci.*, **35 (2)**, 242–257.

Turner, D., and U. Löhnert, 2014: Information content and uncertainties in thermodynamic profiles and liquid cloud properties retrieved from the ground-based atmospheric emitted radiance interferometer (aeri). *J. Appl. Meteor. Climatol.*, **53 (3)**, 752–771.

Turner, D. D., and W. G. Blumberg, 2018: Improvements to the aerioe thermodynamic profile retrieval algorithm. *IEEE Selected Topics Appl. Earth Obs. Remote Sens.*, **12 (5)**, 1339–1354.

Wagner, T. J., W. F. Feltz, and S. A. Ackerman, 2008: The temporal evolution of convective indices in storm-producing environments. *Wea. Forecasting*, **23 (5)**, 786–794.

Wakefield, R. A., J. B. Basara, J. C. Furtado, B. G. Illston, C. R. Ferguson, and P. M. Klein, 2019: A modified framework for quantifying land–atmosphere covariability during hydrometeorological and soil wetness extremes in oklahoma. *J. Appl. Meteor. Climatol.*, **58 (7)**, 1465–1483.

Wang, Y., Y. Huang, and X. Cui, 2018: Impact of mid-and upper-level dry air on tropical cyclone genesis and intensification: A modeling study of durian (2001). *Adv. Atmos. Sci.*, **35 (12)**, 1505–1521.

Wei, J., H. Su, and Z.-L. Yang, 2016: Impact of moisture flux convergence and soil moisture on precipitation: a case study for the southern united states with implications for the globe. *Climate Dyn.*, **46 (1-2)**, 467–481.

Welty, J., and X. Zeng, 2018: Does soil moisture affect warm season precipitation over the southern great plains? *Geophys. Res. Lett.*, **45 (15)**, 7866–7873.

Wilks, D. S., 2011: *Statistical methods in the atmospheric sciences*, Vol. 100. Academic press.

Wu, J., and P. A. Dirmeyer, 2020: Drought demise attribution over conus. *J. Geophys. Res.*, **125 (4)**, e2019JD031 255.

Wu, W., and R. E. Dickinson, 2004: Time scales of layered soil moisture memory in the context ofland–atmosphere interaction. *J. Climate*, **17 (14)**, 2752–2764.

Wulfmeyer, V., and Coauthors, 2018: A new research approach for observing and characterizing land–atmosphere feedback. *Bull. Amer. Meteor. Soc.*, **99 (8)**, 1639–1667.

Yosef, G., R. Walko, R. Avisar, F. Tatarinov, E. Rotenberg, and D. Yakir, 2018: Large-scale semi-arid afforestation can enhance precipitation and carbon sequestration potential. *Sci. Rep.*, **8 (1)**, 1–10.

Zhang, F., Z. Pu, and C. Wang, 2019: Impacts of soil moisture on the numerical simulation of a post-landfall storm. *J. Meteor. Res.*, **33**, 206–218.

Zhang, F., and C. Wang, 2021: Impacts of soil moisture on the numerical simulation of a post-landfall storm. *J. Geophys. Res.*, **126 (1)**, 2020JD033 842.

Zhang, J. A., R. F. Rogers, P. D. Reasor, E. W. Uhlhorn, and F. D. Marks Jr, 2013: Asymmetric hurricane boundary layer structure from dropsonde composites in relation to the environmental vertical wind shear. *Mon. Wea. Rev.*, **141 (11)**, 3968–3984.

Zhang, W., G. Villarini, G. A. Vecchi, and J. A. Smith, 2018: Urbanization exacerbated the rainfall and flooding caused by hurricane harvey in houston. *Nature*, **563 (7731)**, 384–388.